Investigation and control of strong-field photoemission from metal nanotips

Michael Förster

München 2016

Investigation and control of strong-field photoemission from metal nanotips

Michael Förster

Dissertation
an der Fakultät für Physik
der Ludwig–Maximilians–Universität
München

vorgelegt von
Michael Förster
aus Schweinfurt

München, den 18.12.2015

Erstgutachter: Prof. Dr. Peter Hommelhoff
Zweitgutachter: Prof. Dr. Matthias Kling
Tag der mündlichen Prüfung: 04. April 2016

La machine n'isole pas l'homme des grands problèmes de la nature
mais le plonge plus profondément en eux.
Antoine de Saint-Exupéry
Terre des hommes (1939)

Zusammenfassung

Diese Arbeit befasst sich mit der Untersuchung und Kontrolle der Photoemission von metallischen Nanospitzen mit Femtosekunden-Lichtpulsen. Durch in-situ Oberflächenkontrolle auf atomarer Skala sowie Anregung intensiver Nahfelder sind Nanospitzen ein wertvolles Modellsystem für starke Licht-Materie-Wechselwirkung am Festkörper. Von Nanospitzen emittierte Elektronenpulse sind darüber hinaus wegen der hohen Strahlqualität für Mikroskopie und Beugungsexperimente hochinteressant. In unseren Experimenten verwenden wir Femtosekunden-Lichtpulse, um die Stärke des angeregten Nahfeldes zu vermessen, und formen Lichtfelder mit dem Ziel der Untersuchung und effizienten Kontrolle der Photoemission auf optischem Wege.

Wir beobachten Rückstreuung eines Teils der emittierten Elektronen mit der Nanospitze gelenkt durch das laserinduzierte Nahfeld, ein grundlegender Effekt der Attosekundenphysik. Durch Vergleich der höchsten so erreichten Elektronenenergie im charakteristischen Plateau des Elektronenspektrums mit Modellen der Starkfeldphysik bestimmen wir die Stärke des Nahfeldes am Apex der Spitze auf einer Skala von 1 nm und stellen gute Übereinstimmung mit numerischen Lösungen der Maxwellgleichungen fest. Wir geben außerdem einen Ausblick auf eine vollständige Charakterisierung der zeitlichen Struktur von Nahfeldern durch Attosekunden-Streaking.

Aus einem starken fundamentalen und einem perturbativen zweiten harmonischen Laserpuls formen wir ein asymmetrisches Lichtfeld auf der Femtosekunden-Zeitskala. Mit diesem Lichtfeld gelingt uns erstmals die kohärente Kontrolle der Photoemission von Nanospitzen. Mittels der relativen Phase zwischen Fundamentaler und zweiter Harmonischer erreichen wir einen bemerkenswert hohen Kontrast im Elektronenstrom von 94 % und schalten so den Strom mit Lichtfeldern. Der Mechanismus für die Kontrolle ist die Interferenz zwischen zwei kohärenten Quantenpfaden, die jeweils zur Emission führen. Der Vergleich unserer Ergebnisse mit Dichtefunktionaltheorie legt nahe, dass angeregte Zustände die Elektronenemission resonant verstärken. In diesem Experiment und einem anderen Aufbau mit weiter verbesserter Zeitauflösung beschäftigen wir uns darüber hinaus mit der Lebensdauer beteiligter angeregter elektronischer Zustände, für die wir obere Schranken im fs-Bereich finden.

Schließlich präsentieren wir eine Lichtquelle basierend auf nichtlinearer Frequenzkonversion, die Sub-Zwei-Zyklen Pulse um 2 μm mit stabiler Träger-Einhüllenden-Phase bei einer Repetitionsrate von 100 kHz erzeugt. Diese stellen die bisher kürzesten Pulse in diesem Frequenzbereich bei einer solch hohen Repetitionsrate dar. In einer ersten Anwendung

dieser Lichtquelle untersuchen wir den Übergang vom Multiphotonen- zum Tunnelregime der Keldysch-Theorie am Festkörper.

Abstract

This thesis is devoted to the study and control of photoemission from metallic nanotips induced by femtosecond laser pulses. In-situ atomic-scale surface control and the excitation of intense near fields render nanotips an exceptionally valuable model system for light strongly interacting with the solid state. By virtue of their nanometric size they simultaneously represent an attractive source of high-quality femtosecond electron pulses for imaging or diffraction experiments. In our studies we use femtosecond light pulses to determine the near-field strength, and sculpt light waveforms to investigate photoemission, as well as to control it with high fidelity in an all-optical way.

We observe rescattering of a fraction of photoemitted electrons with the parent tip steered by the laser-induced near field, a hallmark of attosecond physics. Assisted by theoretical modelling we determine the strength of the tip's near field at the apex from the cut-off of the characteristic plateau in electron energy spectra. We thereby perform a measurement of the tip's near field on a scale of 1 nm, comparing well with simulations of Maxwell's equations. We present an outlook towards complete temporal characterization of near fields by attosecond streaking.

With a strong fundamental pulse and a perturbative second harmonic we create an asymmetric waveform on the femtosecond timescale. Employing it on a tungsten nanotip we demonstrate coherent control of photoemission from a nanotip for the first time. With the relative phase between fundamental and second harmonic as a tuning knob we control above-threshold photoemission with a contrast of 94 %. We explain our findings in the Brumer-Shapiro picture with interference between two quantum paths leading to photoemission. By comparing our results with density functional theory calculations we find that intermediate states likely resonantly enhance multiphoton emission. We also address the question of the lifetime of excited states in the metal both in this experiment and with another setup with improved temporal resolution and find upper bounds on the fs timescale.

Finally, we present a novel setup of multi-stage nonlinear frequency conversion to yield carrier-envelope phase-stable sub-two-cycle pulses around 2 μm at a repetition rate of 100 kHz, representing the shortest pulses in this wavelength regime at such a high repetition rate. As a first application, we employ this source to investigate the transition from the multiphoton to the tunneling regime of photoemission at the solid state.

Contents

Chapter 1

Introduction

Nanotips have been at the very center of scientific attention over decades. Exactly 60 years ago, in 1955, Erwin Müller and his student Kanwar Bahadur succeeded to visualize atoms for the very first time – atoms on the surface of a metal tip imaged by field ion microscopy [1], a technique that Müller had invented in 1951 [2]. In 1968 Erwin Müller, John Panitz, and Brooks McLane introduced the atom probe [3], which enables atomic-scale composition analysis of alloys in material science. While these initial breakthroughs were made possible by the high electric fields that can be created at sharp structures, further research on high-resolution imaging techniques sought to directly make use of the nanoscale dimensions of tips. In scanning probe microscopy experiments, nanometer or even atomic-scale resolution relies on a tiny probe to confine the interaction with the sample. Examples are scanning tunneling microscopy invented by Gerd Binnig and Heinrich Rohrer in 1982 [4], atomic force microscopy invented by Gerd Binnig, Calvin Quate, and Christoph Gerber in 1986 [5], as well as scanning near-field optical microscopy, realized by Dieter Pohl in 1984 [6]. As another important application, nanotips are used as electron source in electron microscopes of the highest resolution [7], acting as a point-like emitter, and as source of ions for focused ion beam microscopes. It is noteworthy that these three lines of microscopy able to resolve atomic structure all employ nanotips as an integral part of their technique.

Here we discuss photoemission from metallic tips induced by femtosecond laser pulses. Thereby, our experiments combine methods from surface physics, strong-field physics, linear and nonlinear optics, as well as nanooptics. While strong-field physics and attosecond physics have been successfully explored in atomic and molecular systems [8], damage thresholds and averaging over a large, mostly inhomogeneous, volume pose severe challenges to their study at solid state systems [9]. In several ways, metallic nanotips overcome these limitations: They allow atomic-scale surface control and inspection by means of field ion microscopy, rendering them probably the most well-controlled nanoscale solid state system. Moreover, they present a single emitter in the focal spot, avoiding averaging over many emitters under possibly different conditions. Finally, optical near fields are excited at their apex, simplifying the generation of strong light fields without exceeding damage thresholds. All these advantages have recently ignited a soaring interest in fundamental

photoemission studies at metal nanotips [10, 11, 12, 13, 14, 15, 16, 17]. Aside from the character as a model system and with an eye to applications, nanotips are simultaneously in the spotlight for their electron emission properties. Photoemission from nanotips displays a high degree of transverse coherence [18], paving the way to coherent illumination of a large sample in time-resolved electron diffraction measurements [19]. High static fields can be applied to the tip to avoid the spread of the electron wavepacket [20, 21], enhancing temporal resolution in a diffraction experiment. Moreover, large arrays of nanotips can be fabricated with a high degree of homogeneity [22] to scale the emitted electron current; such arrays are currently being explored as electron emitters for coherent x-ray generation [23].

In this work we examine the laser-excited near field at nanotips in detail. By enhancing and simultaneously confining electric fields on sub-wavelength dimensions, near fields offer a very general approach to investigate and manipulate matter on the nanoscale. Since the exact form and strength of near fields depends crucially on even minute structural properties, atomic-scale in-situ control over the surface renders nanotips an ideal testbed for their study. Surprisingly, despite the importance of the magnitude of field enhancement for many studies involving tips aside from photoemission experiments, such as tip-enhanced near-field optical microscopy [24], literature values obtained both experimentally and by simulations diverge considerably. We use photoelectrons that are steered back to the surface of the tip by the near field and scatter elastically there before reaching the detector as a probe. Comparing photoelectron spectra with attosecond physics models we measure the near field on a scale of 1 nm, approaching the length scale of quantum effects [25]. We investigate the dependence of field enhancement on tip geometry and tip material and in this way gain insight into the dominant field enhancement mechanism. Further, as an outlook, we present results from an attosecond streaking experiment, which allows complete reconstruction of the temporal shape of a near field.

Furthermore, as one of the main results of this thesis, we devise and implement an all-optical way to coherently control photoemission from a tungsten nanotip. We thereby introduce a very efficient handle to the manipulation of nanotip photoemission and address the fundamental questions of lifetime and coherence of excited electronic states at solids. Over the years, different concepts for the control of quantum systems using the coherence properties of light, enabled by the unprecedented electric field strenghts and coherence properties of the laser [26], have been put forward. In particular electronic degrees of freedom with a typical energy scale of electron volts – just as the typical photon energies of lasers – have been at the center of attention. Amongst other ideas, Paul Brumer and Moshe Shapiro pioneered a frequency-domain approach to optimize for the desired product state in a chemical reaction [27, 28]. It relies on the interference between different pathways within the quantum system under study, in a particular implementation enabled by the simultaneous presence of optical harmonics in addition to a fundamental frequency [29]. Using an infrared laser pulse and its second harmonic as a weak admixture we synthesize an asymmetric electric field. We observe that the relative phase between the two light pulses either enhances photoemission considerably, or reduces it to almost zero. Spectrally-resolved photoemission experiments reveal that all multiphoton orders are affected by the relative phase between fundamental and second harmonic pulse in the

same way. This observation, together with the measured scaling of the degree of control with second harmonic intensity, strongly suggests a quantum-pathway interference effect in the photoemission process: We simultaneously offer the electrons two coherent pathways involving different number of photons of the fundamental and second harmonic for emission, which interfere constructively or destructively. It is remarkable that despite the solid-state nature of our emitter two pathways suffice to describe the observed switching behavior. In this context we also address the question of excited intermediate states in the metal and confine their lifetime to the femtosecond regime for our parameters. The short lifetimes we observe are of particular importance for the duration of the emitted electron wavepacket. Given the short lifetime of the intermediate states we also find that photoemission from tungsten tips may in the future serve as a nonlinear element for pulse duration measurements.

As another main result, we set up a light source at 2 μm, which features, to our knowledge, the shortest pulses in this wavelength regime at a repetition rate of 100 kHz. Proper choice of nonlinear interactions ensures passive stabilization of the carrier-envelope phase. We thereby obtain a light source tailored for the investigation of strong-field phenomena at nanostructures, where the phase-controlled few-cycle waveform allows precise definition of the external force applied to the system under study and the high repetition rate considerably reduces acquisition times. Moreover, our source is an attractive seed for high-power pulses in this wavelength regime, where high-intensity pulses can generate coherent x-rays in the transparency range of water for imaging of nanoscopic biological samples [30]. We present the current implementation of the setup and analyze the system performance in detail. As a first application of this source we investigate the transition between multiphoton and tunneling regime within the framework of Keldysh theory and record electron energy spectra in the tunneling regime as a function of the carrier-envelope phase. Here we discover a phase-dependent feature indicative of sub-cycle dynamics.

The thesis is organized as follows:

- Chapter 1 introduces our experiments and gives an overview of this thesis.
- Chapter 2 summarizes experimental and theoretical foundations that the experiments in the following chapters rely on. In particular we discuss second- and third-order nonlinear optical processes, the Keldysh theory of photoemission, and particularities of photoemission from solid state systems. We briefly touch upon dynamics after emission, namely electron rescattering. We also introduce the ultrahigh vacuum chamber used for the experiments and discuss sample preparation and characterization.
- Chapter 3 deals with the near fields at metal nanotips. We discuss spatial and temporal characteristics of the near fields, as relevant for our experiments. The focus of the chapter is on the measurement of the near field at the tip apex with rescattering electrons as a probe. As an outlook we discuss attosecond streaking experiments on metal nanotips.

- Chapter 4 addresses time-resolved studies of photoemission at metal nanotips. In the first part we present coherent control of above-threshold photoemission in a Brumer-Shapiro scheme involving two interfering quantum pathways. We discuss the concept, setup, results, and compare experimental observations to theory models. In a second part we turn to time-resolved studies involving two photons of the same color.
- Chapter 5 is concerned with a novel carrier-envelope phase-stable light source at $2\,\mu$m. We introduce the current setup and its performance in detail. We move on to discuss photoemission experiments performed with this source.
- Chapter 6 serves as a summary and gives an outlook to future directions.

Manuscripts in peer-reviewed journals and books

Submitted manuscripts

Two-color coherent control of femtosecond above-threshold photoemission from a tungsten nanotip
M. Förster, T. Paschen, M. Krüger, C. Lemell, G. Wachter, F. Libisch, T. Madlener, J. Burgdörfer, and P. Hommelhoff
submitted, arXiv:1603.01516 (2016).

Attosecond nanoscale near-field sampling
B. Förg, J. Schötz, F. Süßmann, M. Förster, M. Krüger, B.-N. Ahn, W. A. Okell, K. Wintersperger, S. Zherebtsov, A. Guggenmos, V. Pervak, A. Kessel, S.A. Trushin, A. M. Azzeer, M. I. Stockman, D.-E. Kim, F. Krausz, P. Hommelhoff, and M.F. Kling
in press, Nat. Commun. 7:11717 (2016), *arXiv:1508.05611* (2015).

Published manuscripts

Tip-based source of femtosecond electron pulses at 30 keV
J. Hoffrogge, J.-P. Stein, M. Krüger, M. Förster, J. Hammer, D. Ehberger, P. Baum, and P. Hommelhoff
J. Appl. Phys. **115**, 094506 (2014).

Self-probing of metal nanotips by rescattered electrons reveals the nano-optical near-field
M. Krüger, S. Thomas, M. Förster, and P. Hommelhoff
J. Phys. B **47**, 124022 (2014).

Ultrashort laser oscillator pulses meet nano-structures: From attosecond physics at metal tips to dielectric laser accelerators
S. Thomas, M. Krüger, J. Breuer, M. Förster, and P. Hommelhoff
J. Phys.: Conf. Ser. **467**, 012004 (2013).

Probing of optical near-fields by electron rescattering on the 1 nm scale
S. Thomas, M. Krüger, M. Förster, M. Schenk, and P. Hommelhoff
Nano Lett. **13**, 4790 (2013).

From above-threshold photoemission to attosecond physics at nanometric tungsten tips
M. Krüger, M. Schenk, J. Breuer, M. Förster, J. Hammer, J. Hoffrogge, S. Thomas, and P. Hommelhoff
Chapter in *Progress in Ultrafast Intense Laser Science* **IX**
edited by K. Yamanouchi and K. Midorikawa (Springer 2013).

Attosecond physics in photoemission from a metal nanotip
M. Krüger, M. Schenk, M. Förster, and P. Hommelhoff
J. Phys. B **45**, 074006 (2012).

Carrier-envelope phase-stable sub-two-cycle pulses tunable around 1.8 μm at 100 kHz
C. Homann, M. Bradler, M. Förster, P. Hommelhoff, and E. Riedle
Opt. Lett. **37**, 1673 (2012).

Coherent two-dimensional ultraviolet spectroscopy in fully noncollinear geometry
U. Selig, C.-F. Schleussner, M. Förster, F. Langhojer, P. Nuernberger, and T. Brixner
Opt. Lett. **35**, 4178 (2010).

Chapter 2

Theoretical and experimental foundations

In this Chapter we introduce the theoretical concepts as well as the experimental setup and procedures we employ in the course of this thesis. We first examine the foundations of efficient frequency conversion of light waves in the presence of a material in Section 2.1. We evaluate the response of the material in a perturbative expansion that allows us to separately discuss many different processes. In Sections 2.2 and 2.3 we move on to discuss photoemission of electrons from a metal induced by infrared laser pulses and the ensuing dynamics of the electron in the laser field. We discuss how and why we involve models beyond a perturbative picture of light-matter interaction in this case. Sections 2.4 and 2.5 round off this Chapter with an introduction to the ultrahigh vacuum chamber employed in our experiments and a description of sample preparation and characterization.

2.1 Parametric nonlinear optics

2.1.1 Introduction

Imagine a light wave passing through a medium. For simplicity we assume that the medium is nonmagnetic and that free charges and free currents are absent. Since the medium is composed of bound charged particles on a microscopic scale, it will respond to the presence of the electric field of the light wave by the formation of a polarization $\mathbf{P}(\mathbf{r},t)$, a dipole moment per unit volume. This polarization can in turn emit radiation, i.e. mathematically it serves as a source term in the wave equation derived from Maxwell's equations:

$$\nabla \times \nabla \times \mathbf{E}(\mathbf{r},t) + \frac{1}{c^2}\frac{\partial^2}{\partial t^2}\mathbf{E}(\mathbf{r},t) = -\frac{1}{\epsilon_0 c^2}\frac{\partial^2}{\partial t^2}\mathbf{P}(\mathbf{r},t), \tag{2.1}$$

where $\mathbf{E}(\mathbf{r},t)$ is the electric field, c is the speed of light in vacuum and ϵ_0 is the vacuum permittivity.

For sufficiently small electric fields the response of the material, the polarization, will be linear in the applied electric field. One may imagine the response of a bound electron around its equilibrium state, i.e. in a harmonic potential. The restoring force to the equilibrium position will be linear with the displacement. This linear response for weak electric fields essentially corresponds to the wealth of classical optics. However, when our toy system is driven sufficiently far away from equilibrium, the harmonic approximation of the potential will no longer hold, giving rise to nonlinear forces, and thus a nonlinear response of the medium to the external field. While evidence of such nonlinear optical phenomena had been found already in 1941 [31], it is fair to say that the unprecedented electric fields of the laser demonstrated by Maiman in 1960 [26] were an essential prerequisite for the development of the field of nonlinear optics from a barely accessible exotic regime of light-matter interaction to an important enabling technology.

For the description of light-matter interaction the polarization is typically split into its linear $\mathbf{P}^{(1)}(\mathbf{r},t)$ and nonlinear part $\mathbf{P}^{\mathrm{NL}}(\mathbf{r},t)$ and expanded in a power series of higher-order polarization terms:

$$\mathbf{P}(\mathbf{r},t) = \mathbf{P}^{(1)}(\mathbf{r},t) + \mathbf{P}^{\mathrm{NL}}(\mathbf{r},t) = \mathbf{P}^{(1)}(\mathbf{r},t) + \mathbf{P}^{(2)}(\mathbf{r},t) + \mathbf{P}^{(3)}(\mathbf{r},t) + ... \quad . \tag{2.2}$$

We note that this perturbative expansion is well founded for the description of parametric processes at typical field strenghts that we discuss here. However, it can diverge for resonant transitions and for laser fields of strength approximately equal to the atomic field strength [32] and we will see that we have to include such nonperturbative effects in the treatment of photoemission in Section 2.2.

The power series is often written in the frequency domain:

$$P_i = \epsilon_0 \left(\sum_j \chi^{(1)}_{ij} E_j + \sum_{jk} \chi^{(2)}_{ijk} E_j E_k + \sum_{jkl} \chi^{(3)}_{ijkl} E_j E_k E_l + ... \right). \tag{2.3}$$

Here we introduced the optical susceptibilities χ. They are the fundamental quantities that describe the response of the material to an applied field. For clarity of notation we dropped all frequency and position arguments. The optical susceptibility $\chi^{(n)}$ is a tensor of rank $n+1$. This accounts for the fact that the material is in general nonisotropic and that the electric field is a vector. χ has to fulfill symmetry requirements that usually reduce the number of independent components significantly. One particularly important case is that $\chi^{(2)}_{ijk} = 0$ for centrosymmetric materials, i.e. materials with an inversion center. In this case the lowest optical nonlinearity is $\chi^{(3)}$.

Parametric processes are an important sub-class of nonlinear interactions, which leave the quantum state of the material unchanged and so e.g. no energy or momentum is transferred between the light wave and the material. Instead, the light field itself is modified by the presence of the material via the source term in Equation 2.1. This allows creating light with new frequencies and transferring energy between different involved beams. The accessible wavelength range of a light source can so be greatly diversified. We will see exemplarily in Chapter 5 how various parametric processes can be cascaded to form a

light source with highly attractive parameters. For excellent descriptions of perturbative nonlinear light-matter interaction we refer the reader to [32,33] and due to the availability of introductory literature just give a brief account here.

2.1.2 Second-order optical nonlinearities

The second-order susceptibility has the form

$$\chi^{(2)}_{jkl}(\omega_3;\omega_2,\omega_1) \quad . \tag{2.4}$$

It connects two input fields of frequency ω_1 and ω_2 and a response of the material at a third frequency ω_3. Since second-order processes are the lowest-order nonlinear processes they are the most efficient, making them attractive for applications in frequency conversion.

Sum-frequency generation

In this process two photons of angular frequency ω_1 and ω_2 form one photon of angular frequency $\omega_3 = \omega_1 + \omega_2$. The first nonlinear process studied with the laser was second harmonic generation [34], a special case of sum-frequency generation, already in 1961. In this case, two photons of frequency $\omega_1 = \omega_2 = \omega$ yield one photon at frequency $\omega_3 = 2\omega$. In the following we discuss sum-frequency generation in detail and take the chance to look at important concepts of parametric nonlinear interactions in general.

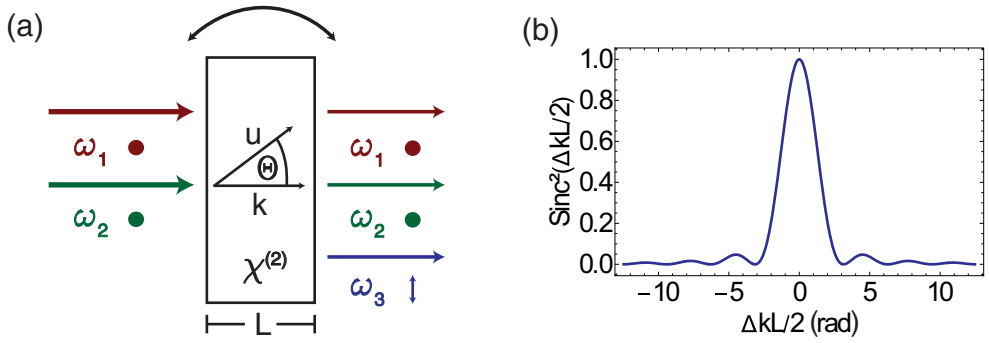

Figure 2.1: Illustration of sum-frequency generation. (a) Generation of the sum-frequency of beams of frequency ω_1 and ω_2 in a negative uniaxial material with $\chi^{(2)}$-nonlinearity. On display is type I phasematching facilitated by angle tuning. The beams of ω_1 and ω_2 share the same ordinary polarization, while the beam of ω_3 is of extraordinary polarization. The **k**-vectors of the laser beams have an angle Θ to the crystal axis **u**. Modified from [32]. (b) Illustration of phasematching according to Equation 2.5.

Consider two laser beams of frequency ω_1 and ω_2 and intensity I_1 and I_2, respectively, travelling along the positive z-direction through a nonlinear medium of length L, see Fig. 2.1(a). For simplicity we assume that the nonlinear interaction is weak so the incoming beams are not depleted, i.e. they have approximately constant intensity throughout

the propagation. They generate a beam at frequency ω_3 and of intensity $I_3(z)$. A simple derivation [32] yields that the intensity of the third beam $I_3(L)$ is given by:

$$I_3(L) = \frac{8d_{\text{eff}}^2\omega_3^2 I_1 I_2}{n_1 n_2 n_3 \epsilon_0 c^2} L^2 \text{sinc}^2\left(\frac{\Delta k L}{2}\right). \tag{2.5}$$

Here d_{eff} is the effective nonlinearity of the medium, a measure of the effectivity of the process for given frequencies, polarizations and propagation directions obtained from $\chi^{(2)}_{jkl}$, and n_1, n_2, and n_3 are the refractive indices for the waves. We draw particular attention to the factor $\text{sinc}^2(\Delta kL/2)$. As we can see in Fig. 2.1(b) it is critical for the efficiency of frequency conversion. Δk is the wavevector mismatch, i.e.

$$\Delta k = k_1 + k_2 - k_3 = \frac{n_1\omega_1}{c} + \frac{n_2\omega_2}{c} - \frac{n_3\omega_3}{c} \quad . \tag{2.6}$$

Equation 2.6 is known as phase matching condition. We found it here for sum-frequency generation, but it is equally important for other parametric processes. The nonlinear interaction is most efficient for $\Delta k = 0$, but a simple transparent material with no resonances will show normal dispersion and for $\omega_1 \leq \omega_2 < \omega_3$ this means $n_1 \leq n_2 < n_3$, and we seemingly cannot fulfill Equation 2.6.

Birefringence is a solution to this problem. We consider a negative uniaxial crystal, where the extraordinary index of refraction is smaller than the ordinary index of refraction for a given frequency: $n_e(\omega) < n_o(\omega)$. Depending on the angle θ of the laser beam with respect to the optical axis of the crystal the following relation holds for the index of refraction for the extraordinary beam $n_e(\theta)$:

$$\frac{1}{n_e(\theta,\omega)^2} = \frac{\sin^2\theta}{n_e^2(\omega)} + \frac{\cos^2\theta}{n_o^2(\omega)} \quad . \tag{2.7}$$

Depending on the polarization of the involved lower-frequency waves we distinguish two different cases:

- Type I phasematching is defined as the case in which the two lower-frequency waves have the same polarization.
- For type II phasematching the polarizations of the lower-frequency waves are orthogonal to each other.

The following two methods arise:

- Angle tuning: A particular angle θ is chosen to ensure fulfilling Equation 2.6. It is also referred to as critical phase matching due to its sensitivity of angular alignment.
- Temperature tuning: θ is fixed at 90° and the appropriate refractive indeces are ensured by heating the nonlinear crystal. It is also referred to as non-critical phase matching.

We note that other methods exist, most notably quasi-phase matching, and refer the reader to [35] for a review.

The nonlinear medium is naturally an important choice for efficient conversion. The effective nonlinearity d_{eff} is a critical parameter and additionally for femtosecond lasers it is essential that the phase-matching condition can simultaneously be fulfilled for the whole spectrum of the laser pulse. This figure of merit is referred to as phase-matching bandwidth. One popular choice among many others is beta barium borate (β-BaB_2O_4), often called BBO for short [36]. It is a negative uniaxial crystal with large transmission window of about $200 - 2600\,\text{nm}$. It is easy to handle, can be fabricated with high quality in arbitrary orientation, and has a high threshold for laser-induced damage. We shall use it extensively in Chapter 5.

Optical parametric amplification and difference-frequency generation

In optical parametric amplification (OPA) one photon of frequency ω_p, usually referred to as pump, is stimulated to split up into a signal and idler photon of frequencies ω_s and ω_i, thus amplifying the signal beam. Optical parametric amplification is employed in many optics laboratories to obtain a wavelength-tunable light source and can be pushed to the extreme to create intense few-cycle laser pulses by virtue of its parametric nature. The appeal of this amplification approach is the large achievable bandwidth and scalability, as no energy is deposited in the nonlinear crystal by the amplification process itself. This is in contrast to a laser amplifier, where creating a population inversion for amplification results in heating the laser crystal due to the quantum defect.

Difference-frequency generation (DFG) is the same process as OPA, but with another outcome in mind: Again a pump photon creates a signal and an idler photon, but this time the idler is the beam that is used. We use this process to transfer a short pulse from the visible to the infrared and at the same time stabilize its carrier-envelope phase in a passive fashion in Chapter 5.

To obtain intense and short pulses, simultaneous amplification of a large spectral bandwidth of the seed pulse is necessary. Analogous to Equation 2.6 we have to fulfill the following requirements for efficient and broadband conversion:

$$\Delta\mathbf{k} = \mathbf{k}_p - \mathbf{k}_s - \mathbf{k}_i = 0 \tag{2.8}$$

$$\frac{\partial \Delta\mathbf{k}}{\partial \lambda_s} = 0 \quad . \tag{2.9}$$

These conditions can be met in two ways: The approach we will not discuss is degenerate OPA, so that $\mathbf{k}_s = \mathbf{k}_i = \mathbf{k}_p/2$. We refer the interested reader to [37]. Instead we focus on noncollinear optical parametric amplification (NOPA), a popular way of broadband amplification of a signal wave [38]. The 'trick' to fulfill both requirements is to introduce an angle Ω between the group velocities of signal and idler beam. Ω has to meet the following relation with the respective group velocities $\mathbf{v}_{\text{g,s}}$ and $\mathbf{v}_{\text{g,i}}$:

$$v_{\text{g,i}} \cos\Omega = v_{\text{g,s}} \quad . \tag{2.10}$$

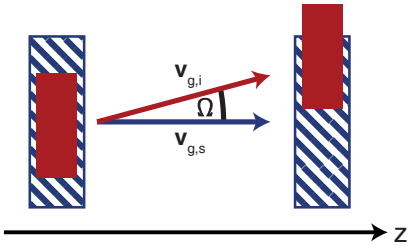

Figure 2.2: Intuitive interpretation of Equation 2.10, adapted from [38]. Broadband phasematching in optical parametric amplification is ensured by introducing an angle Ω between the group velocities of signal and idler. In this way, signal and idler pulse propagate along the z direction with the same speed. Solid red area represents the spatial extent of the idler pulse and hatched blue area the spatial extent of the signal pulse at two instances in time.

We can interpret this requirement as follows: Broadband phasematching can be achieved if the absolute value of the group velocity of the signal equals the projection of the absolute value of the group velocity of the idler, see Fig. 2.2.

In practice one does not readily have access to Ω directly and instead adjusts the angle between pump light and seed light (and therefore signal) α, which then defines Ω, see Fig. 2.3(a). In panel (b) we see examplarily for a typical NOPA pumped with the second harmonic of a Titanium Sapphire amplifier at $\lambda_p = 400\,\text{nm}$ and type I phasematching in

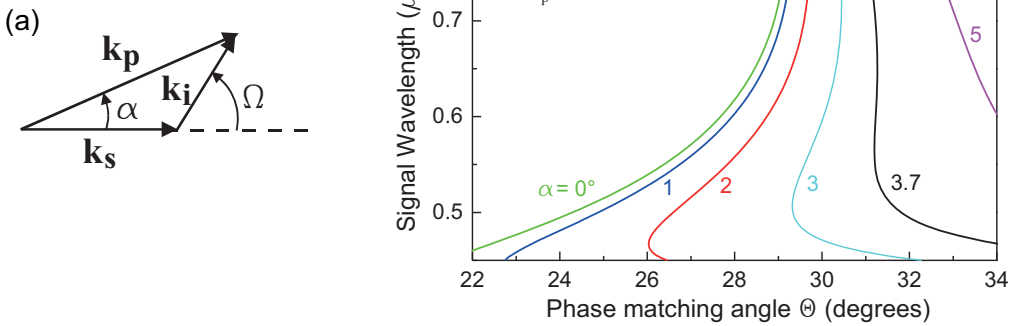

Figure 2.3: Phasematching in the NOPA. (a) Definition of wavevectors and angles: k_p wavevector of pump, k_s wavevector of the signal, k_i wavevector of the idler. α is the angle between pump and signal and Ω is the angle between signal and idler, as introduced before. (b) Phase matching angle Θ as function of desired signal wavelength and the angle α for a pump wavelength of 400 nm in BBO for type I OPA. Green line $\alpha = 0°$, blue line $\alpha = 1°$, red line $\alpha = 2°$, turquoise line $\alpha = 3°$, black line $\alpha = 3.7°$, purple line $\alpha = 5°$. A noncollinearity angle $\alpha = 3.7°$ allows choosing a phasematching angle $\Theta \approx 31°$ for simultaneous phasematching for a broad spectral range. Taken from [37].

BBO how a noncollinearity angle of $\alpha = 3.7°$ allows simultaneous phasematching from $500 - 700\,\text{nm}$ at a phasematching angle of $\Theta \approx 31°$.

For a detailled discussion of design considerations for noncollinear optical parametric amplification we refer the reader to [39].

2.1.3 Third-order optical nonlinearities

Third-order optical nonlinearities are ubiquitous, since they are present also for isotropic media and the number of phenomena associated with them is large. We limit our discussion to the optical Kerr effect. It is responsible for self-focusing of laser beams and self-phase modulation, which ultimately leads to supercontinuum generation, i.e. a dramatic spectral broadening of the laser pulse which preserves the coherence [40]. In Chapter 5 we use a supercontinuum as initial seed for optical parametric amplification.

Optical Kerr effect

For pulsed laser beams the index of refraction n becomes an intensity-dependent quantity. It can be shown that

$$n = n_0 + n_2 \left\langle I(\mathbf{r}, t) \right\rangle_t . \tag{2.11}$$

Here n_0 denotes the intensity-independent refractive index and n_2 the nonlinear index of refraction. $\langle I(r,t)\rangle_t$ is a cycle-average of the light intensity. n_2 is related to the optical susceptibility by

$$n_2 = \frac{3}{4n_0^2\epsilon_0 c}\chi^{(3)}. \tag{2.12}$$

Since the intensity profile of a typical laser beam transverse to its propagation direction is not a flat top but a Gaussian, this leads to a position-dependent refractive index, which effectively corresponds to a lens: The beam will be focused and thus high intensities are reached. This is denoted self-focusing. After a critical intensity has been reached multiphoton ionization in the material creates a partial plasma that balances the focusing effect, leading to a filament.

In this filament the nonlinear index of refraction n_2 modifies the temporal properties of the laser pulse. High intensities may be created by self-steepening and the instantaneous frequency is modified by self-phase modulation. The interplay of these effects leads to a dramatic broadening, termed supercontinuum generation. For the sake of brevity we will not go into detail as the modelling of many simultaneously present nonlinearities is intricate and merely state that octave-spanning laser spectra can thus be routinely obtained.

A popular material choice for supercontinuum generation in the visible is sapphire, while in the UV calcium fluoride is employed [41]. We will use a yttrium aluminum garnet (YAG) crystal for supercontinuum generation in Chapter 5 as it has a lower threshold for self-focusing and thus supercontinuum generation due to its higher n_2 compared to sapphire [42].

So far we have addressed supercontinuum generation in bulk materials. Often, so-called highly nonlinear fibers are employed for spectral broadening, in particular for lower pulse energies. In this case self-focusing is not required and the fiber confines the light to a small area. It can be made of a material with high n_2 and engineered with favourable dispersion properties. We use such a highly nonlinear fiber to spectrally broaden the pulses we generate in Chapter 5 and measure their carrier-envelope phase.

2.1.4 Carrier-envelope phase in parametric processes

One important parameter for few-cycle laser pulses – laser pulses containing only a few optical cycles – is their carrier-envelope phase (CEP), depicted for $\Phi_{\mathrm{CEP}} = \pi/2$ and $\Phi_{\mathrm{CEP}} = 0$ in Fig. 2.4. It helps to define the shape of the electric field, which typically exerts the force in light-matter interaction. Parametric processes affect the CEP of a laser pulse in a defined way. The CEP of the generated pulse can be obtained from the CEP of the generating pulses in simple terms [43, 44], see Fig. 2.5 for the definition of frequencies.

For sum-frequency generation (SFG) the following relations hold true:

$$\omega_3 = \omega_1 + \omega_2 \tag{2.13}$$

$$\Phi_3 = \Phi_1 + \Phi_2 + \pi/2 \tag{2.14}$$

where Φ is the respective CEP.

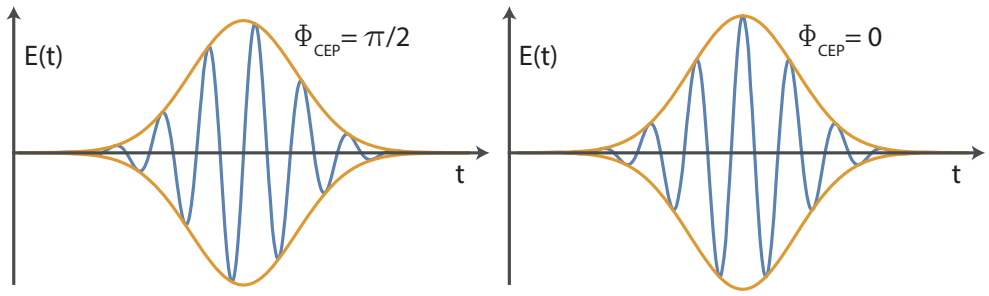

Figure 2.4: Illustration of the carrier-envelope phase. The carrier-envelope phase of a laser pulse is the phase between the carrier wave (depicted in blue) and the envelope (depicted in orange). It plays an important role in light-matter interaction, e.g. in high-harmonic generation.

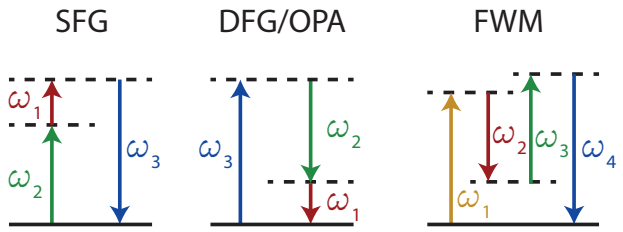

Figure 2.5: Selected parametric processes and definition of involved photon angular frequencies. Reproduced from [43].

In an analogous manner we obtain the following relation for the OPA/DFG process:

$$\omega_2 = \omega_3 - \omega_1 \tag{2.15}$$
$$\Phi_2 = \Phi_3 - \Phi_1 - \pi/2 \quad . \tag{2.16}$$

We note that the CEP of a laser pulse generated by DFG is (up to a constant) the difference of the CEPs of the input pulses. If the input pulses have the same unstabilized – and thus fluctuating – CEP, the laser pulse created by DFG will still be CEP-stable. Performing DFG between two pulses of the same CEP thus allows passive phase-stabilization. This approach was popularized by Baltuška [45] and a comprehensive review can be found in Reference [43]. This method of stabilizing the carrier-envelope phase is all-optical and avoids fast feedback [46] or feedforward [47] mechanisms to stabilize the carrier-envelope phase. The latter two are commonly employed in laser oscillators.

The last process we discuss is self-phase modulation, which is a special case of four-wave mixing (FWM) [48]. Here

$$\omega_4 = \omega_1 - \omega_2 + \omega_3 \tag{2.17}$$
$$\Phi_4 = \Phi_1 - \Phi_2 + \Phi_3 - \pi/2 \quad . \tag{2.18}$$

We emphasize that the preservation of coherence in supercontinuum generation is rather surprising, as noted in [49], but essential for the application of supercontinua as coherent seeds for OPA.

2.2 Photoemission from metal surfaces

Electron emission upon illumination of metal surfaces is a basic non-parametric process of light-matter interaction. Its discovery in 1887 along with other groundbreaking experiments initiated a change in the paradigms that shaped our current understanding of physics. With ultrafast lasers available, photoemission continues to be an active area of research to date, opening the door to attosecond science. Below we give an account of photoemission mechanisms in general and at the solid state in particular. Similar discussions to the one below can be found in references [50, 51].

2.2.1 Field emission

It is instructive to first discuss (cold) field emission, a process where electrons are emitted from a metal by a strong static field. The process was probably discovered already in the 18th century in the context of gas discharges [52], but for a long time not recognised as a separate phenomenon. A complete explanation was not given before Fowler and Nordheim, who used quantum mechanics in 1928 [53]. An electron close to the Fermi edge tunnels out of a material into vacuum through the barrier formed by the presence of a strong external field on the order of GV/m, see Fig. 2.6. The barrier is lowered by ΔW_S due to the image

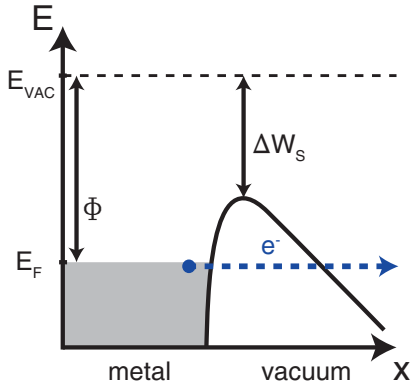

Figure 2.6: A sketch of field emission. A static field leads to the formation of a tunneling barrier, which electrons at the Fermi energy E_F may tunnel through. Simultaneously the Schottky effect lowers the barrier by ΔW_S.

potential, known as Schottky effect [54]:

$$\Delta W_S = -\sqrt{\frac{e^3|E_{DC}|}{4\pi\epsilon_0}} \quad . \tag{2.19}$$

The Fowler-Nordheim equation [55,56] provides a link between the emission current density j to the present DC electric field strength E_{DC}:

$$j(E_{DC}) \propto \frac{1}{t^2(y)} E_{DC}^2 \exp\left(-\frac{4\sqrt{2m_e}}{3e\hbar} v(y) \frac{\phi^{3/2}}{|E_{DC}|}\right) \quad . \tag{2.20}$$

$v(y)$ and $t(y)$ are dimensionless functions, and y is the Nordheim parameter

$$y = \sqrt{\frac{e^3|E_{DC}|}{4\pi\epsilon_0\Phi^2}} \quad . \tag{2.21}$$

Within the range of our parameters we can utilize the approxomations $v(y) \approx 0.85$ and $t(y) \approx 1$ [57]. We note the exponential form of Equation 2.20, typical for tunneling processes.

2.2.2 Photoelectric effect

The photoelectric effect was first described by Heinrich Hertz in 1887 [58]. Hertz was at the time experimenting with spark gaps. He observed that the UV light emitted by a spark in one spark gap of his apparatus enhanced the spark in a second gap. However, he could not identify why the UV light influenced his experiment. The discovery of the electron by Thomson in 1897 [59] enabled scientists to understand the observations in Hertz's experiment with an increased conductivity of the gap by free electrons created by light. Some

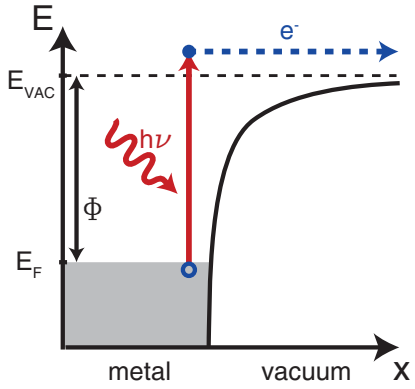

Figure 2.7: Illustration of the photoeffect. A photon transfers its energy $h\nu$ to an electron and thereby allows it to exit the metal.

observations were, however, in disagreement with the present theory of electromagnetism. Einstein explained the photoelectric effect as an interaction on a quantum level [60] in his annus mirabilis 1905, a work that would earn him the nobel prize in 1921.

The mechanism is shown in Fig. 2.7. A photon excites an electron from an occupied state in the metal to a free continuum state of the surrounding vacuum. The maximum kinetic energy $E_{\mathrm{kin,max}}$ of the emitted electron is in this process given by:

$$E_{\mathrm{kin,max}} = h\nu - \Phi, \tag{2.22}$$

where Φ is the work function of the metal, h is Planck's constant and ν the frequency of the photon. Since just one photon is involved in the elementary process the emitted electron current scales linearly with light intensity. As typical work functions of metals lie in the range of $3-6\,\mathrm{eV}$ [61] only illumination with UV or higher energy radiation can lead to photoemission via the photoelectric effect.

2.2.3 Nonlinear photoemission and Keldysh theory

Since nowadays popular femtosecond solid state lasers operate in the near infrared (e.g. Ti:Sapphire $h\nu = 1.5\,\mathrm{eV}$, Yb:YAG $h\nu = 1.2\,\mathrm{eV}$, and Erbium $h\nu = 0.8\,\mathrm{eV}$), one photon cannot provide sufficient energy to an electron for emission. However, lasers offer an unprecedented flux of photons and strong accompanying electric fields in the optical domain, thus enabling emission processes, where the simultaneous presence of several photons is required. Before we look into the intuitive models of emission, we discuss a theoretical approach encompassing them.

Keldysh theory

Due to the invention of the laser Keldysh realized the need for a theory describing the ionization of a quantum system in a strong electromagnetic field. He formulated his theory for atoms in 1965 [62] and it was already in the same year extended to metals by Bunkin

and Fedorov [63]. It provides a very successful theoretical framework for the description of electron emission for the typical experimental situation: 1) The work function Φ is much greater than the photon energy $h\nu$. 2) High intensities enable nonlinear processes.

We first review the assumptions of the theory [62]: It describes photoemission from the ground state of a quantum system to a set of free continuum states. In its simplest form it disregards other bound states than the ground state in the atom or solid and we will limit ourselves to this case first.[1] The particular influence of a strong electric field is then taken into account only by choosing electrons in the free states to be accelerated by the field. The effect of the Coulomb potential on the free electron is not directly included.[2]

Calculations then yield a total emission probability P, which takes the form

$$P(\gamma) \propto \exp\left[-\frac{2\Phi}{h\nu}\cdot\left(1+\frac{1}{2\gamma^2}\right)\cdot\left(\operatorname{arsinh}(\gamma)-\gamma\frac{\sqrt{1+\gamma^2}}{1+2\gamma^2}\right)\right]. \tag{2.23}$$

The theory provides the experimentalist with a single parameter γ, the so-called Keldysh parameter:

$$\gamma = \sqrt{\frac{\Phi}{2U_p}}, \tag{2.24}$$

where U_p is the ponderomotive energy, i.e. the mean kinetic energy of a free electron of charge $-e$ and mass m_e oscillating in a cw light field with amplitude E_0 and angular frequency ω:

$$U_p = \langle E_{\mathrm{kin}}\rangle_t = \frac{e^2E_0^2}{4m_e\omega^2}. \tag{2.25}$$

Two limiting cases emerge from Formula 2.23. For $\gamma \gg 1$ Equation 2.23 is approximated by

$$P(\gamma) \propto E_0^{2\Phi/h\nu}. \tag{2.26}$$

This regime is called 'multiphoton regime'. Conversely, for $\gamma \ll 1$ we obtain

$$P(\gamma) \propto \exp\left(-\frac{8\pi\sqrt{2m_e}\Phi^{3/2}}{3ehE_0}\right). \tag{2.27}$$

This rate is reminiscent of the rate for the tunneling of an electron in the presence of a strong DC field. It is therefore termed 'tunneling regime'.

[1] Interestingly Keldysh discusses the influence of intermediate states already in his seminal paper.

[2] The Coulomb field has been included later amongst other extensions in the work of Perelomov, Popov and Terent'ev [64, 65, 66].

Multiphoton Photoemission

We now discuss multiphoton photoemission, i.e. the limit $\gamma \gg 1$, in detail. Fig. 2.8(a) shows the physical picture. Instead of a single photon now multiple photons transfer their energy to an electron, which is promoted to a continuum state. The emission scales with a power law in laser intensity. The exponent is the lowest number of photons necessary to overcome the work function.[3] In the ideal multiphoton case, the final states of the electrons are not changed by the presence of the laser field and the emission can be described with lowest order perturbation theory.

Multiphoton photoemission has first been studied at atoms [67, 68] and later also at surfaces [69], where heating of the solid and subsequent thermionic emission complicated interpretation due to the high deposition of energy with micro- and nanosecond laser pulses. We will later turn to thermionic emission, but first discuss above-threshold photoemission.

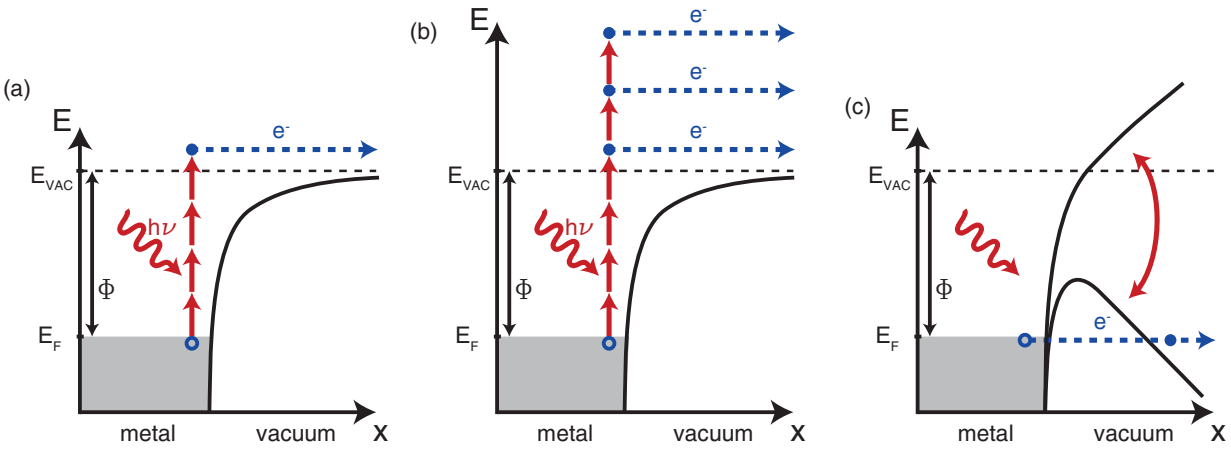

Figure 2.8: (a) Sketch of multiphoton photoemission. An electron is promoted to a continuum state, absorbing the energy of four photons. (b) Sketch of above-threshold photoemission (c) Sketch of light-induced tunneling: A barrier is formed for a fraction of an optical cycle, through which the electron may exit the metal. Note that this notion corresponds to a classical limit, where the photon energy is no longer involved.

Above-threshold photoemission

With a high photon flux available, not all electrons will acquire the energy of the minimum number of photons needed for emission - some of them will collect more quanta, as is depicted in Fig. 2.8(b). In a corresponding electron spectrum multiple peaks appear, spaced by the photon energy. This intuitive physical picture was nicely demonstrated in the first experiments at gases [70] and solids [71].

[3] The non-integer value in Equation 2.26 is an artifact of the derivation. The actual scaling is $P(\gamma) \propto E_0^{(2n)}$, where n is the closest larger integer to $\Phi/h\nu$ [50].

Around $\gamma = 1$ the situation is further complicated by the beginning influence of the laser field on the final electron states. Interestingly already the authors of the initial experiments of multiphoton photoemission [67, 68] report that the scaling law of the observed current with laser intensity does not quite fit their expectation and attribute this to Stark shifts of the final states. The dressing of the final states with the laser field can prohibit electron emission into these states, effectively closing the lower emission channels. This is also observed in above-threshold photoemission from metal tips [13, 14].

Light-induced tunneling

For $\gamma \ll 1$ many of the lower-lying final states of electron emission are closed and new, higher lying-final states gain in importance. While it is in principle still possible to describe emission in terms of the photon picture [13] it is helpful to take the classical limit and consider the photons as a classical field again.

In this model the electric field of the laser is so strong that it leads to the formation of a tunneling barrier at the illuminated target. With a certain probability the electron can penetrate this barrier and appear on the vacuum side, leading to emission. For gases, emission can take place for both maxima of the electric field oscillation, at surfaces the symmetry is broken and for our purposes here allows emission only during one half cycle of the optical oscillation, see Fig. 2.8(c). Besides [13] also [17] shows first results of the investigation of electron emission in the tunneling regime at nanotips.

2.2.4 Photoemission via intermediate states

Candidates for intermediate states

In our treatment of photoemission we have so far neglected higher-lying bound states. They can resonantly enhance photoemission and serve as a reservoir of excited electrons with a certain lifetime. For photoemission from metal surfaces it is obviously a simplification to ignore such states, as one way of defining metals is to state that the Fermi energy intersects the conduction band. This means that there are unoccupied allowed states above the Fermi level in the metal. These volume states can extend to the surface and there may serve as intermediate states for electron emission.

Additionally, the broken translational symmetry at the surface allows for so-called surface states. Tamm [72] and Shockley [73] in the 1930s first discussed the existence of electronic states at the interface between metal and vacuum. In a simple model we can assume the electron wave to be trapped by the surface potential on the one side and Bragg reflection from the periodic structure on the other side, thus effectively leading to a localized state, exponentially decaying in both directions.

At metal surfaces there is another kind of state called image potential state, which is localized mostly in the vacuum region contrary to the Tamm and Shockley state [74]. Image potential states were predicted by Echenique and Pendry [75] in 1978. They are quite similar in nature to Rydberg states at atoms. They have energies just below the

vacuum level and their center of gravity moves away from the surface for higher lying states, freeing them of the influence of the bulk. They are known to have lifetimes up to picoseconds. While their presence seems unlikely, it is currently unknown whether these sensitive image potential states also survive the curved and atomically structured surface of a metal nanotip. An excellent review on the lifetimes of states at the surface of metals can be found in [76].

Once an intermediate state is excited, emission may proceed via the optical fields or DC tunneling. To collect the electrons we bias the tip with a voltage in the range of 100-1000 V with respect to the detector, so that the electric field at the tips is on the order of 1 GV/m. The accompanying Schottky effect lowers the potential barrier, as displayed in Fig. 2.9, so that tunneling may proceed.

Photofield emission

One way to populate higher lying states is the direct excitation of an electron from close to the Fermi level to the intermediate state by absorption of a photon. This was observed in the excitation of a tungsten tip with a CW argon ion laser with UV and alternatively visible radiation [77] and for illumination of a tungsten tip with an IR femtosecond laser in [10, 78].

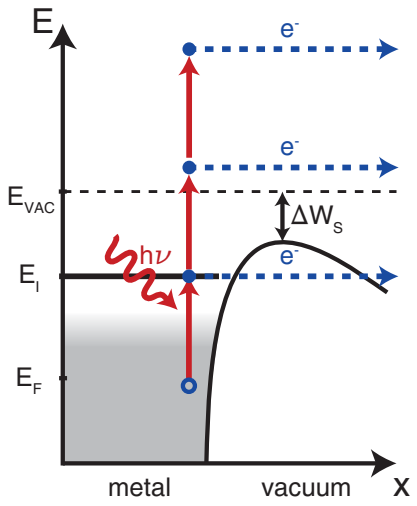

Figure 2.9: Schematic of emission processes via an intermediate state located at E_I. Population of this intermediate state may occur via the absorption of one photon by an electron or by (transiently) heating the electron gas in the metal to sufficient temperatures. This state may then serve as the starting point of electron emission. For example, optical field emission and multiphoton photoemission may occur from here, as well as field emission due to the typically applied DC bias field. ΔW_S is the effective lowering of the work function by the Schottky effect.

Thermally enhanced field emission

Another way to populate the intermediate state is a high temperature of the electron gas of the metal tip as a whole, as shown in [51]. Deposition of energy in the electron gas and electron-electron scattering first leads to an elevated electron temperature. Electron-phonon scattering then leads to a thermalization of the electrons with the lattice and thermal conduction transports the heat to the tip shank. Emission via a heated electron gas is shown to lead to electron pulses of several hundred femtoseconds duration in an IR-pump and THz-probe study [79].

2.3 Electron rescattering in strong laser fields

We have so far discussed the process of electron emission driven by strong laser fields. However, the emitted electron is still subject to the forces of the laser field and we will now discuss possible ensuing dynamics. While most electrons directly move to the detector, a small fraction interacts with the parent matter again. Even though it is only a small fraction, it encompasses very exciting physics and has thus been studied intensively for gas phase targets [8]. A simple intuitive model that nevertheless accurately describes experimental observations is the three-step model, first introduced by Corkum [80] and Kulander [81]:

(I) The first step is the emission of the electron by optical tunneling as described in Section 2.2.3. The electric field creates a potential barrier that the electron can tunnel through to be freed. The electron starts with zero momentum.

(II) The second step is the propagation of the electron in the laser field according to Newton's laws. The electron will be accelerated and acquire some amount of kinetic energy.

(III) In a third step the electron reencounters the parent matter, where it was emitted. Four outcomes are conceivable [8]:

- Detachment of another electron, so-called non-sequential double ionization: The active electron frees another electron from the parent matter.
- Excitation of bound electrons in the parent matter: Energy is deposited to the parent matter in an inelastic collision.
- Recombination: The electron recombines with the hole it left behind in the quantum system. The electron's energy difference is released in the form of a high-energy photon. In contradiction with traditional perturbative nonlinear optics photon spectra show a plateau in count rate towards high energies with a cutoff at $3.17U_p + \Phi$ [80,81]. With sufficiently short IR driving pulses this leads to the formation of attosecond bursts of light.

- Rescattering: The active electron is backscattered elastically at the parent matter and acquires high kinetic energies. This also leads to the formation of a plateau, this time in electron spectra, where the cutoff is located at $10.007U_p + 0.538\Phi$ according to quantum orbit theory [82].

At tips the first observation of the plateau caused by electron rescattering was demonstrated in [15]. The authors could also show that the shape of the plateau depends on the carrier-envelope phase of the laser pulse, thus identifying attosecond features. A different study also demonstrated that the quiver motion of the electron can be quenched for infrared radiation [16]: The electron then has a larger oscillation amplitude and therefore experiences the decay of the near field (which extends on the order of the tip radius as we will see later) and does not return to the tip for rescattering.

2.4 Ultrahigh vacuum chamber and detection system

Experiments are performed in an ultrahigh vacuum (UHV) chamber[4] with a base pressure of around $5 \cdot 10^{-10}$ mbar to avoid collisions of photoelectrons with atoms, enable single-electron sensitivity, ensure low surface contamination, and enable the characterization techniques described below, especially field-ion microscopy. References [56, 83] describe the chamber in detail and we will only give a brief account here.

A rotary vane pump[5] creates a fore-vacuum of around 10^{-3} mbar. At the chamber a turbomolecular pump[6], an ion pump[7], and a titanium sublimation pump[8] are attached to reach UHV conditions. After each venting the chamber is baked out at around 120 °C for around 10 h. A leak valve[9] is attached to the chamber to fill the chamber with gas, in particular nitrogen for venting and noble gases for field ion microscopy.

The wire with the nanotip at its end is spot-welded to a v-shaped wire, whereof both ends have connections to the outside, see Fig. 2.10. This enables cleaning of the tip via resistive heating and also allows applying high voltage to the tip for characterization, cleaning, and to bias the tip for photoelectron measurements. The nanotip is attached to a 3D translational nanopositioner[10] to move the tip into the stationary laser focus created by an off-axis parabolic mirror[11], which is adjusted with a microscope objective[12]. The laser beams enter the vacuum chamber through a 4 mm thick viewport of BaF_2[13], which we selected due to negligible dispersion around 2 μm and the possibility of excellent dispersion compensation with double chirped mirrors for the standard Titanium:Sapphire laser pulses.

[4] CVT Ltd. UK
[5] Pfeiffer Vacuum, Duo 010M
[6] Pfeiffer Vacuum, HIPace 80
[7] Gamma Vacuum, TiTan CV 100L
[8] Gamma Vacuum, TSP
[9] MDC, E-MLV-22
[10] Attocube, 2x ANPx101 and 1x ANPz101
[11] Kugler, custom made, $f = 15$ mm
[12] Mitutoyo, $f = 20$ mm, NA = 0.55
[13] Torr Scientific Ltd., BVPZ38BaF2

The vacuum chamber contains two charged-particle detectors: A microchannel plate detector (MCP)[14] and an electron spectrometer[15]. They can be exchanged with manual feedthroughs without opening the vacuum chamber. The microchannel plate detector is used for spectrally integrated electron count measurements and spatially-resolved tip characterization and photoelectron measurements. For spatially-resolved measurements a CCD camera monitors the MCP backside[16]. For single-electron pulse counting we connect the MCP front side to a bias-tee[17] and terminate the DC component. The AC component is amplified in a pulse amplifier[18]. Pulses are subsequently discriminated[19] and adapted to TTL standard[20], before being counted at a DaQ device[21]. Data acquisition is either performed with the help of MATLAB or LabView. The electron spectrometer is a retarding-field spectrometer, containing a grid on a variable negative potential U_{grid} relative to the tip to decelerate the electrons. Only electrons with sufficient kinetic energy can overcome this high-pass filter and be counted on the far side as a voltage pulse. Count rate as a function of U_{grid} is an integrated electron spectrum that can be differentiated to yield the electron spectrum. Due to fluctuations in count rate the differentiation is aided by a Savitzky-Golay filter [84] to smooth the data. Data acquisition is facilitated by the same DaQ card as mentioned above. The resolution of the spectrometer is about 80 meV.

[14] Photonis, Micro Channel Plate detector APD 2 PS 40/12/10/12 46:1 P20
[15] Staib Instruments, RFA2000 retarding field analyzer
[16] Imaging Source DMK21BU04
[17] MiniCircuits, ZFBT-66+
[18] Miteq, AM-3A-000110
[19] PSI FD 103 discriminator
[20] Level adapter LA 8000
[21] National Instruments, PCIe-6343

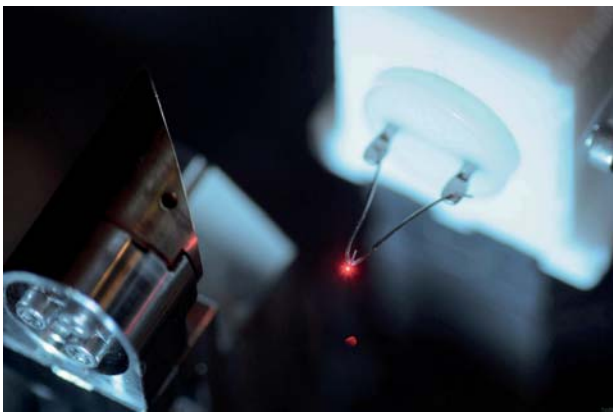

Figure 2.10: Photograph of our experiment. A near-infrared laser pulse is focused to the apex of a tungsten nanotip by an off-axis parabolic mirror (left). The tip is located at the end of the v-shaped wire and appears as bright red spot due to scattering of the laser light. Courtesey of T. Naeser.

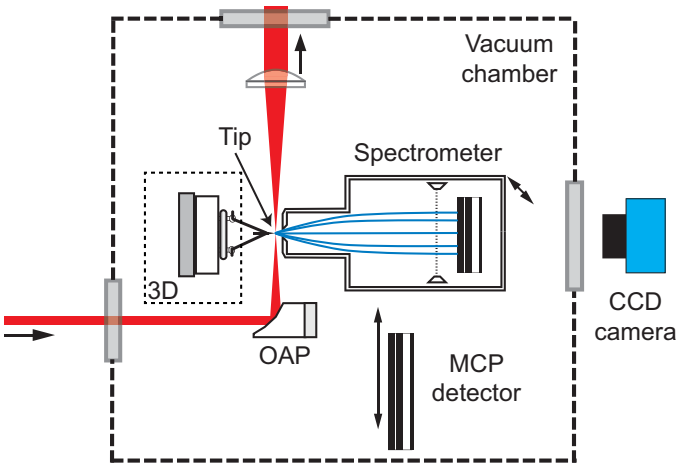

Figure 2.11: Setup of the UHV chamber. The nanotip is attached to a v-shaped wire, which in turn rests on a 3D nanopositioner. Two detectors for charged particles, a microchannel plate detector (MCP) and an electron spectrometer can alternatively be placed in front of the tip without breaking the vacuum, allowing for true in-situ characterization before photoemission measurements. The laser pulses enter the vacuum chamber through a viewport and are focused tightly with an off-axis parabolic mirror (OAP). Tip-laser-alignment is aided by the laser beam exiting the vacuum chamber through another viewport. A CCD camera allows to view electron and ion emission patterns. Modified from [50].

2.5 Nanotip preparation and characterization

One of the great advantages of metal nanotips over other nanostructures for photoemission experiments is the possibility to inspect and modify them in-situ, resulting in a single nanoemitter with well-characterized properties. Since they have been employed for quite some time as electron sources, a number of fabrication processes has been explored. In the following we discuss our methods for tip fabrication and characterization.

2.5.1 Tip preparation

Lamellae drop-off technique

We fabricate metallic nanotips by electrochemical etching in the lamellae drop-off technique [85]. A wire of the tip material is mounted vertically and positioned in the center of two electrodes, which have a relative distance of around 0.5 cm and a diameter of 0.5 – 1.0 cm, illustrated in Fig. 2.12. The arrangement is briefly dipped into the etchant solution, resulting in two films of etchant in the rings. A potential difference is applied between the upper ring and the wire, starting the electrochemical etching process[22]. Since etching is more efficient in the center of the film, etching is anisotropic and the wire thins most in the center of the film. At some point the wire breaks under the influence of gravity and

[22]Obbligato Objectives, Schrodinger's Sharpener model SS03

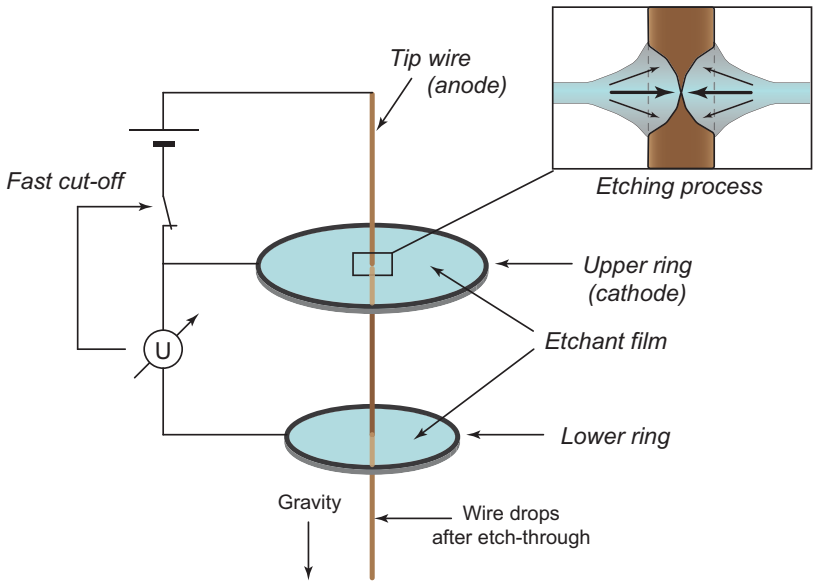

Figure 2.12: Nanotip etching in the lamellae drop-off technique, taken from [50]. A thin metal wire is mounted vertically in the center of two horizontally oriented ring electrodes filled with etchant solution. An etching voltage is applied between the wire and the upper ring. The wire thins until the lower part falls down due to the action of gravity. An electronic circuit detects the wire break and initiates a fast cut-off of the etching voltage to obtain small nanotip radii.

the lower part drops down. An electronic circuit detects the break of the wire and initiates a fast cut-off of the etching voltage for small nanotip radii. The upper part of the wire with the nanotip at its end is used for experiments. Typical radii of curvature, depending on the tip material, are in the range of $5 - 200\,\mathrm{nm}$.

Tungsten tips

To etch tungsten (W) tips with the procedure above we use gold[23] as ring material and a 3 molar aqueous solution of NaOH[24]. The applied voltage is 6 V DC. Two different tungsten wires are routinely used. A polycrystalline wire[25] with a diameter of 0.1 mm and a monocrystalline wire[26] with a diameter of 0.127 mm. After etching the tip is rinsed with destilled water. Typical tips have a radius of curvature of $5 - 20\,\mathrm{nm}$ and a half opening angle of about 3°. The polycrystalline wire usually yields tips in W(110) orientation, i.e. the [110] direction is oriented along the wire. In most photoemission experiments we use tips from monocrystalline wire, so that the [310] direction points along the tip axis. Since the (310) plane of tungsten displays the lowest work function [86], electron emission from these tips is mostly in forward direction, simplifying coupling into the electron spectrometer

[23] Alfa Aesar, 99.95% metal basis, 0.5 mm
[24] Sigma Aldrich, sodium hydroxide pellets 99.99%
[25] Alfa Aesar, 99.95% metal basis
[26] Kore Technology Ltd., PN 12127

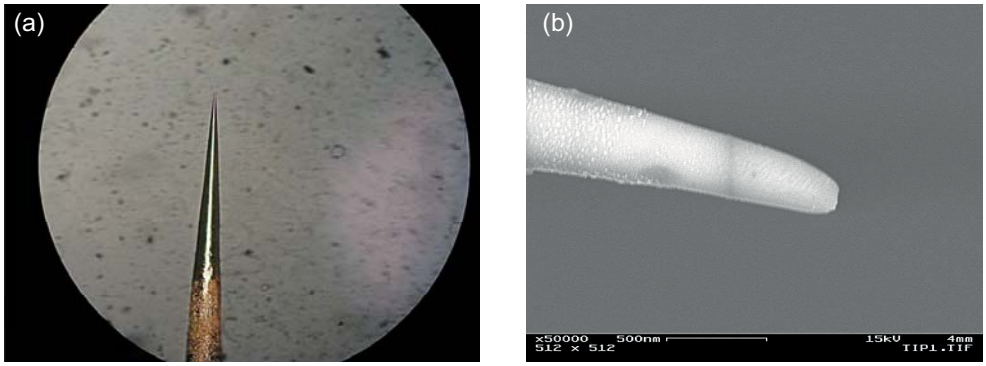

Figure 2.13: Characterization of etched gold tips (a) Optical microscope image of a gold tip etched with KCl. The high surface quality is evidenced by the shiny surface. (b) Electron microscope image of a gold tip with radius of curvature $r \approx 100\,\text{nm}$.

and harnessing the highest optical field, as we will see later.

Gold tips

For the etching of gold (Au) tips we use platinum[27] as ring material and a 90% saturated aqueous solution of KCl [87]. The applied voltage is 10 V DC. We use polycrystalline gold wire[28] with a diameter of 0.1 mm. After etching the tip is rinsed with acetone. Tips produced in this fashion have a radius of curvature in the range of $20 - 200\,\text{nm}$ and a half opening angle of $3 - 6°$. With this procedure we usually obtain tips in [100] direction.

2.5.2 In-situ cleaning

Etched tips are inserted into the UHV chamber for cleaning and characterization before photoemission experiments.

Tip cleaning by heating

Electrochemically etched tungsten tips possess a nm-thick layer of WO_3 and also other remnants from the etching process may be present [88]. Sublimation of the oxides by annealing the tip at around 1100 K removes the oxide layers. To avoid tip blunting care has to be taken not to mobilize the surface atoms to diffusion by heating to temperatures in excess of 1300 K. In practice this can be ensured by a pyrometer. Heating as a cleaning method applies to tungsten tips but not gold tips due to fast blunting of gold tips at elevated temperatures. We note that heating may also heal crystal defects.

[27] Alfa Aesar, 99.95% metal basis, 0.5 mm, annealed
[28] Alfa Aesarc 99.998% metal basis, Premion

Tip cleaning by field evaporation

Upon applying a static potential between tip and a counter electrode, the field at the apex of the tip is given by

$$E = \frac{U}{kr}, \tag{2.28}$$

where r is the tip's radius of curvature and k depends on the geometry of tip and surrounding electrodes and is usually taken to be approximately $k = 5$ [89]. For example, 100 V between a tip of $r = 10\,\mathrm{nm}$ and its counter electrode already results in an electric field at the surface of approximately $|E_{DC}| = 2\,\mathrm{GV/m}$. It is the ease with which high static electric fields can be applied that makes the cleaning by field evaporation and the characterization techniques below feasible.

At static fields of +57 V/nm for tungsten and +35 V/nm for gold [90] protruding atoms of the surface evaporate, leaving a more homogeneous tip behind. Adsorbates or oxides can also be removed this way, making field evaporation a versitile method for ensuring a clean and homogeneous apex. However one should keep in mind that only the apex is cleaned this way due to the static field enhancement and not the shank of the tip.

2.5.3 In-situ tip characterization

Different methods exist for in-situ characterization of metal nanotips and we will restrict ourselves to the ones most employed in this thesis, field emission microscopy and field ion microscopy. Another popular technique, the Fowler-Nordheim plot, is for example discussed in [56].

Field Emission Microscopy

Field emission microscopy is a projection microscope that images the surface of a sharp tip onto a screen, see Fig. 2.14. It was invented by Erwin Müller in 1936 [91]. A negative high voltage is applied to the tip, resulting in the formation of a tunneling barrier at field strengths on the order of GV/m. Field emitted electrons are projected onto the screen. The local work-function differences result in a modulation of tunneling probability and such current density [86], which produces the contrast in the image. The magnification of the field emission microscope can be geometrically determined and is for typical experimental geometries on the order of 10^6.

Field Ion Microscopy

Field ion microscopy developed by Müller in 1951 [2] was the first method to resolve single atoms on a surface [92]. Same as field emission microscopy it is a projection microscope, where the role of the electrons is now played by ions of an imaging gas. Due to the associated reduction in de-Broglie wavelength of the probing particles the resolution is

significantly improved to the atomic scale. The magnification is similar on the order of 10^6.

In practice the UHV chamber is backfilled with an imaging gas of a pressure of about $5 \cdot 10^{-6}$ mbar. A strong positive electric field is created at the tip surface by applying a positive high voltage in the range of 10 kV to it. The imaging atoms are ionized in a thin sheath close to the surface: Due to the strong field an electron will tunnel to the tip and leave the ion to be repelled by the electric field. The ion is accelerated and hits a microchannel plate detector a few cm away from the tip. The different rates of ionization due to the local differences in field strength give rise to the contrast of the image.

The imaging gas is in our case a noble gas: For tungsten we choose helium and for gold neon or argon. The best image field, i.e. the field giving best results, are 44 GV/m for helium[29], 35 GV/m for neon[30], and 19 GV/m for argon[31] [93].

The resolution of the field ion microscope is given by the thickness of the ionization sheath, the lateral velocity of the ions at the instant of field ionization and the quantum mechanical uncertainty of the lateral velocity. Under optimal conditions the field ion microscope reaches a resolution of 0.2 nm [94]. Finally, we would like to note that the combination of a tungsten tip imaged with helium gas allows for simultaneous field evaporation of adsorbed atoms and imaging of the tip surface.

From a field ion microscopy image, one can precisely determine the local radius of curvature of a tip by the 'ring counting method' illustrated in Fig. 2.15. The local radius of curvature r is determined by counting the number of steps n between two known

[29] Linde, Helium 5.0
[30] Linde, Neon 4.5
[31] Linde, Argon 5.0

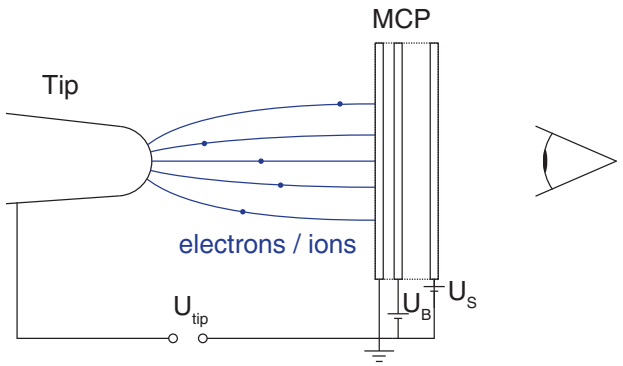

Figure 2.14: Sketch of field emission microscopy (FEM) and field ion microscopy (FIM). This sketch is not to scale for illustration purposes; instead the tip is strongly enlarged. For FEM a negative potential is applied to the tip. Electrons are field emitted from the tip, travel to the MCP and are detected. For FIM the tip is on a positive potential, the UHV chamber is filled with a low-pressure noble gas. Ions form in the vicinity of the surface, travel to the MCP and form the image. The MCP backside is biased at $U_B = 1 - 2\,\mathrm{kV}$ and $U_S = 4\,\mathrm{kV}$.

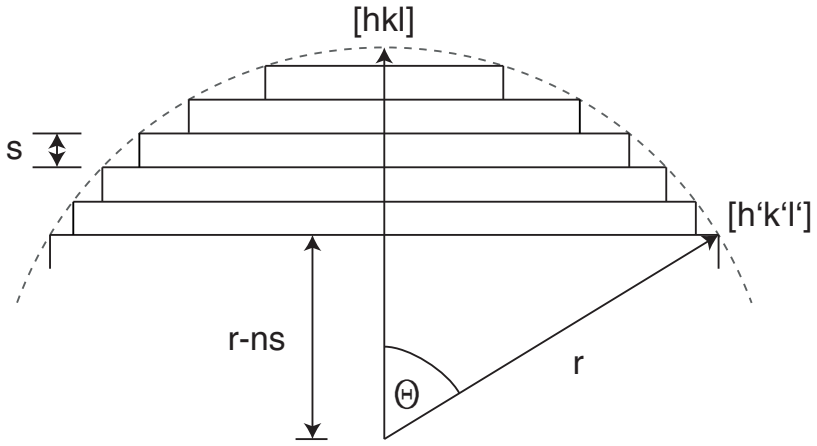

Figure 2.15: Illustration of the 'ring counting method', adapted from [95]. It is used to determine the local radius of curvature r by counting the number of crystallographic steps n of height s between the directions $[hkl]$ and $[h'k'l']$ with the known angle Θ between them.

crystallographic directions $[hkl]$ and $[h'k'l']$, enclosing the angle Θ:

$$\cos\Theta = \frac{r - ns}{r} \quad . \tag{2.29}$$

The step height s evaluates for a cubic lattice as follows:

$$s = \frac{a}{\delta\sqrt{h^2 + k^2 + l^2}} \quad , \tag{2.30}$$

where a is the lattice constant and $\delta = 1$ for even $h + k + l$ and $\delta = 2$ for odd $h + k + l$. With the scalar product we relate Θ to the Miller indices:

$$\cos\Theta = \frac{hh' + kk' + ll'}{\sqrt{h^2 + k^2 + l^2} \cdot \sqrt{h'^2 + k'^2 + l'^2}} \quad . \tag{2.31}$$

Exemplary characterization of a tungsten nanotip

To demonstrate the discussed characterization techniques and show spatially-resolved photoemission from a nanotip induced by a few-cycle Titanium:Sapphire oscillator, we include Figure 2.16. Panel (a) shows a field ion micrograph of the surface of the tip recorded with helium as imaging gas. Clearly the crystal planes can be identified. Single bright dots correspond to single atoms in this picture. Panel (b) displays a field emission micrograph. Only the low-workfunction (310) crystal planes emit electrons, resulting in a single, defined spot. Fig. 2.16(c) shows laser-induced electron emission from a strongly DC-biased tip. Electron emission is in this case not quite as localized as in the case of field emission in panel (b), but clearly dominated by the contributions of the (310) planes.

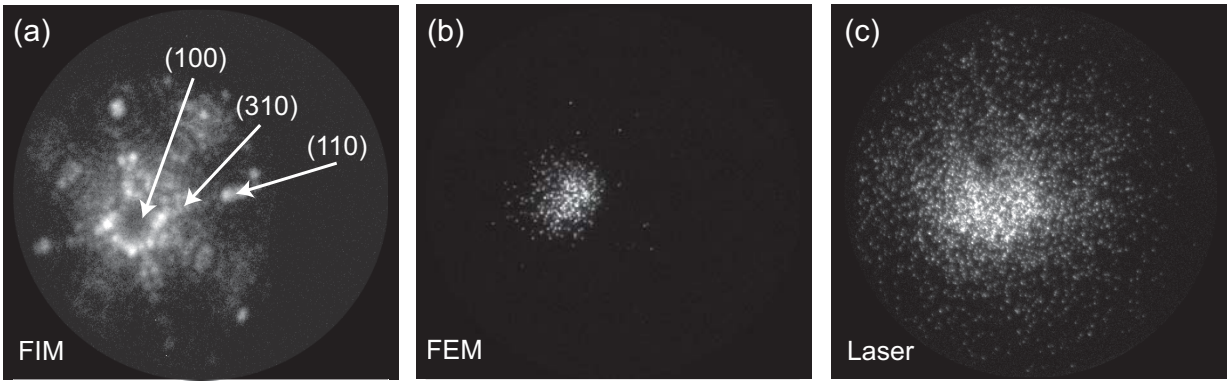

Figure 2.16: Characterization and laser-induced photoemission from a W(310) tip. (a) FIM image with $U_{\mathrm{tip}} = +7.5\,\mathrm{GV/m}$. Field emission and laser-induced emission takes place predominantly close to the low-workfunction (310) planes. (b) FEM micrograph with a static field strength of $E_{DC} \approx -2.7\,\mathrm{GV/m}$. (c) Image of laser-induced electron emission for laser intensity of $I_0 \approx 4 \times 10^{10}\,\mathrm{W/cm^{-2}}$ and static field of $E_{DC} \approx -1.3\,\mathrm{GV/m}$. Modified from [50].

Chapter 3

Near fields at metal nanotips

While localization of electromagnetic energy in free space is limited by diffraction caused by the focusing aperture to about the wavelength of the radiation [96], the presence of matter allows much better confinement. Nano-optics is the study of these phenomena with visible light, reviewed in [97]. Various ways of localizing electromagnetic radiation have been explored: The optical properties of metals like gold or silver allow the propagation of collective excitations, e.g. surface plasmon polaritons, where the fields are concentrated on nanometer scales at the surface [98]. Also the presence of features of sub-wavelength dimensions of dielectric materials will result in concentrated radiation at these features, used for example at dielectric gratings for laser acceleration [99, 100].

'Near fields' as referred to here are thus fields in the vicinity of the surface of a material. Both characteristic features of near fields can be harnessed for applications, localization and enhancement. In particular, nanoscale tips are an important class of nanostructures for application of these effects. Scanning near-field optical microscopy (SNOM) conceived by Synge [101] and realized in the optical domain by Pohl [6] allows to record optical images with sub-wavelength resolution by restricting light-matter interaction with the help of a sub-wavelength aperture, a coated fiber tip. At the same time, the achievable signal/noise of tip-enhanced near-field optical microscopy profits considerably from field enhancement [24] to the extent that these methods allow tip-enhanced Raman scattering of single molecules [24, 102]. Further, field enhancement benefits second harmonic emission [103, 104, 105, 106] from metal nanotips and the subject of our studies, photoemission from metal nanotips [10, 12].

In this chapter we introduce near fields at metallic tips and show a method for the determination of their strength based on the publications [107, 108]. The method can determine the maximum field strength with a resolution on the scale of 1 nm. We also give an outlook on how to completely characterize the temporal form of near fields [109].

3.1 Field enhancement factor at the nanotip apex

3.1.1 Near-field distribution and complex field enhancement factor

As we discussed, near fields are of general interest and of particular importance in highly nonlinear electron emission from metallic nanotips. For a first impression we show a finite-difference time-domain (FDTD) simulation of Maxwell's equations[1] yielding the time-averaged field strength of a tungsten nanotip under laser illumination in Fig. 3.1(a). The polarization of the incident light is linear and aligned with the tip axis, a configuration which we employ in almost all experiments. We see that the electric field is concentrated and enhanced at the tip apex. This localizes nonlinear electron emission to the apex. We also note that the length scale of field decay at the apex is given by the apex radius rather than the wavelength of light. Rotating the incident polarization moves the enhanced near-field region on the apex away from the forward direction [110].

In the temporal domain [Fig. 3.1(b)] simulations show that the shape of the apex near field is very close to that of the exciting field with only a slight ringing after the laser pulse has passed [111]. We can therefore, to a first order approximation, describe the near field at the apex E_n as a stronger and phase-delayed copy of the bare laser field in the focus E_0:

$$E_n(t) = \xi \cdot E_0(t) \tag{3.1}$$

$$\xi = |\xi| \cdot e^{\mathrm{i}\phi} \tag{3.2}$$

with a phase shift ϕ. The absolute value of ξ is of particular interest, as it determines the strength of the near field. Interestingly, it has been under discussion for a long time with values determined from both simulations and experiment displaying an incompatible spread.

3.1.2 Determination of the near-field strength at metal nanotips

Rescattering of electrons discussed in Section 2.3 offers a way to probe the near field at the nanotip apex by comparison to well-established theory. Electrons are emitted by the near field and their movement after emission is governed by it. Depending on the emission time a fraction of the photoelectrons returns to the parent tip, scatters elastically off the surface, and subsequently reaches the detector. These are the 'rescattering' electrons that we are interested in here. The highest energy the electrons can reach with this process, the cut-off energy T_{CO}, is in the framework of quantum orbit theory [82] given by:

$$T_{CO} \approx 10.007 U_p + 0.538\Phi \tag{3.3}$$

$$U_p = \frac{e^2 E_n^2}{4 m_e \omega^2} \quad . \tag{3.4}$$

[1] FDTD method, Lumerical 7.0.1

U_p is the ponderomotive potential of the electron in the near field, Φ the tip work function, $-e$ and m_e electron charge and mass and ω the angular frequency of light. We see that the cutoff energy T_{CO} is directly linked to the near-field strength E_n, so that the near-field strength can be extracted by determining the cutoff. Measurement of the laser intensity in the bare focal spot without nanotip will then yield $|\xi|$.

As a laser source for our experiment we use a commercial Titanium:Sapphire laser oscillator[2] with a pulse duration of approximately 6 fs and a central wavelength of 800 nm and focus this laser light onto the metal nanotip, located in the experimental UHV chamber described in Section 2.4. For dispersion compensation of the vacuum window and a half-wave plate in the beampath we use double chirped mirrors and barium fluoride wedge

[2]VENTEON PULSE:ONE Power edition

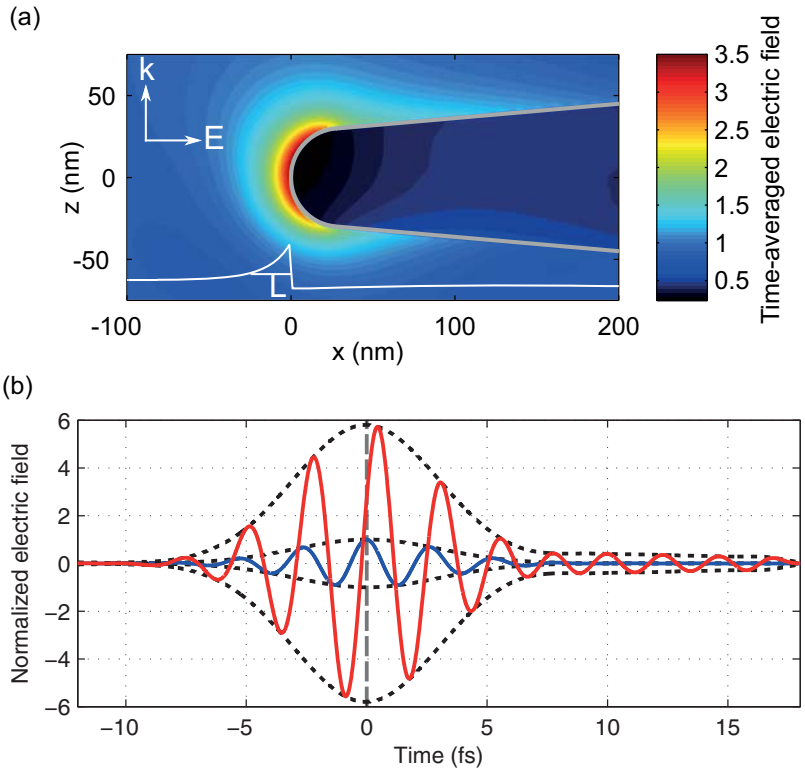

Figure 3.1: (a) Time-averaged electric field strength relative to the bare laser focus at a tungsten nanotip with radius of curvature $r = 30$ nm and a total cone opening angle of 10° illuminated with a 5 fs laser pulse at wavelength $\lambda = 800$ nm. The incident laser propagates in positive z direction and is polarized along the tip axis. The white line shows the near field along a cut at $z = 0$. It indicates that the near-field decay length scale is given by the tip's radius. Taken from [107]. (b) A 5 fs laser pulse at wavelength $\lambda = 800$ nm (blue) excites the near field (red) at a 5 nm tungsten tip. The field is enhanced and phase-delayed, and a small excitation remains after the pulse has passed. Due to the nonlinearity of the observed processes we can neglect this weak field. Courtesey of S. Thomas.

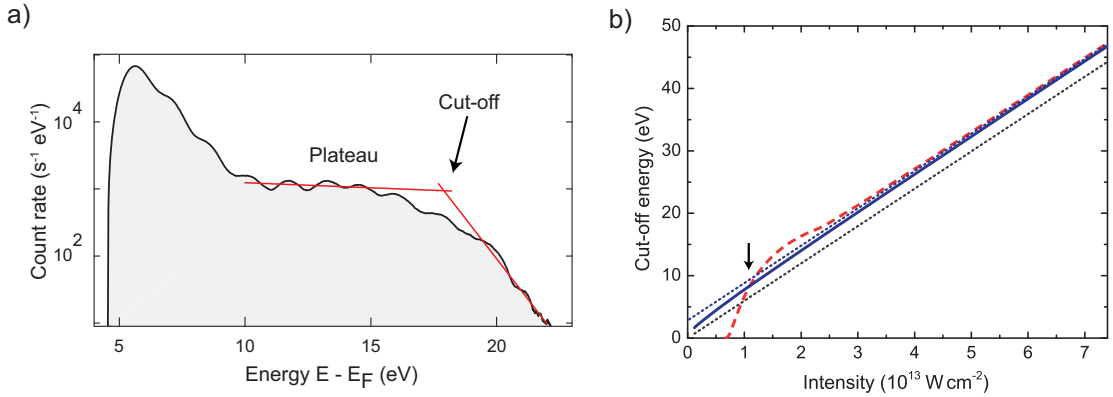

Figure 3.2: Concept of the measurement of the field enhancement factor. a) Exemplary experimental electron spectrum from a tungsten tip using a 6 fs laser pulse centered at 800 nm focused to a far-field intensity - the intensity in the bare laser spot without tip - of $1.3 \cdot 10^{11}$ W/cm^2. In addition to above-threshold photoemission peaks a rescattering plateau emerges. Its cutoff is determined with two exponential fits (red lines). b) Cutoff energy of rescattered electrons in different theoretical models. We show the $10\,U_p$-law (dotted black line), the extended three-step model (dashed red line), a complex trajectory three-step model (solid blue line) and the asymptotic limit (dotted blue line). The arrow indicates the intensity in our experiment, where all models agree within ±12%. Modified from [108].

pairs from the laser manufacturer. With laser powers in the 10 mW-range we observe electron spectra displaying a plateau indicative of the rescattering mechanism [112], as we show exemplarily in Fig. 3.2(a). In panel (b) we display the dependence of the cut-off energy on the intensity in different single-active-electron models. We show the $10\,U_p$-law from the three-step model [80], an extended three-step model including a non-zero electron displacement by tunneling [113, 114, 115, 116], a complex trajectory three-step model [117], and the initially discussed quantum orbit model [82], which is strictly valid only in the tunneling regime and therefore represents a high-intensity limit. All of these theories yield the same relation between cut-off energy and present intensity within ±12% for our parameters, indicated by an arrow in the figure. Therefore, we can confidently use Equation 3.3 to extract the field enhancement, keeping in mind the excellent agreement between single-active-electron calculations, experimental data, and time-dependent density functional theory calculations at nanotips [118, 119].

For the range of parameters of our experiment the distance from the tip the electron gathers information over is on the order of 1 nm. We can neglect the decay of the near field, which decays to $1/e$ from the value directly at the tip within a distance of about $0.8 \cdot r$ since we employ tips of radii $r \geq 8.5$ nm. For longer wavelengths or higher intensity, the near field inhomogeneity has to be considered [16, 120, 121].

We use monocrystalline (310) tungsten and polycrystalline gold tips, where tungsten offers the highest control over the sample and gold is a popular choice in the literature for tip-based experiments and also origin of the indicated discrepancy in reported field enhancement values. For tungsten we clean and inspect the tip in the experiment in-situ

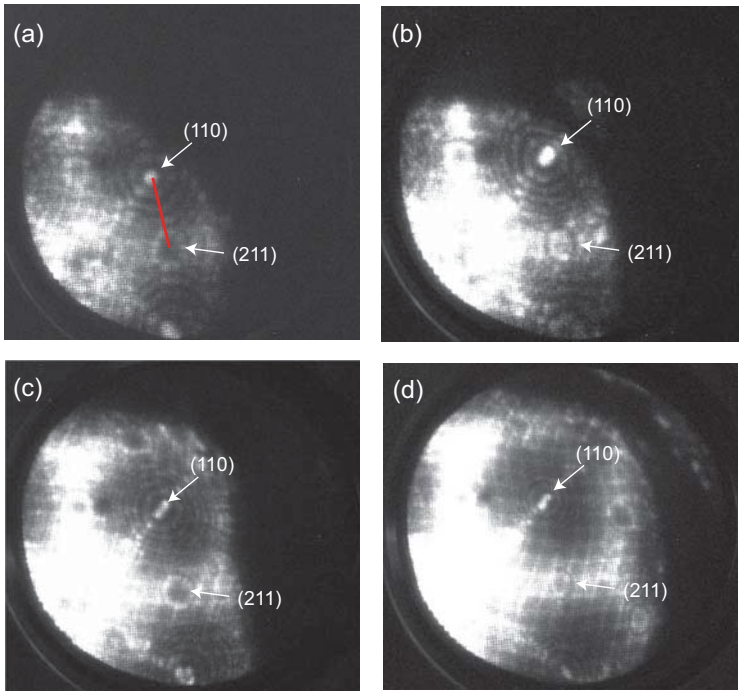

Figure 3.3: Field ion microscopy images of a W(310) tip, gradually blunted by field evaporation. Tip radii r determined by the ring counting method between (110) and (211) poles (red line) are (a) $r = (8.5 \pm 1.7)\,\mathrm{nm}$, (b) $r = (13.6 \pm 1.7)\,\mathrm{nm}$, (c) $r = (15.3 \pm 1.7)\,\mathrm{nm}$, and (d) $r = (18.7 \pm 1.7)\,\mathrm{nm}$. Modified from [108].

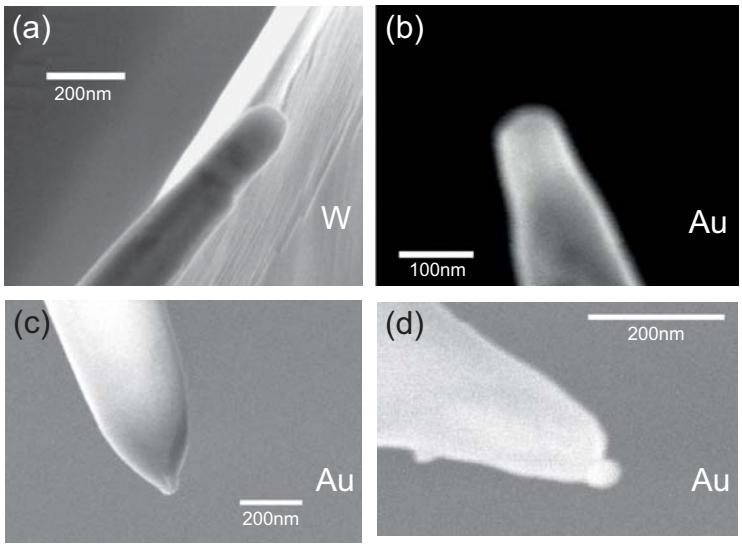

Figure 3.4: Scanning electron micrographs of tungsten and gold tips. (a) Image of the tungsten tip at its final radius of $r = (51 \pm 5)\,\mathrm{nm}$. b)-d) Images of gold tips with radii of (b) $r = (46 \pm 3)\,\mathrm{nm}$, (c) $r = (31 \pm 3)\,\mathrm{nm}$, and (d) $r = (28 \pm 4)\,\mathrm{nm}$. Taken from [108].

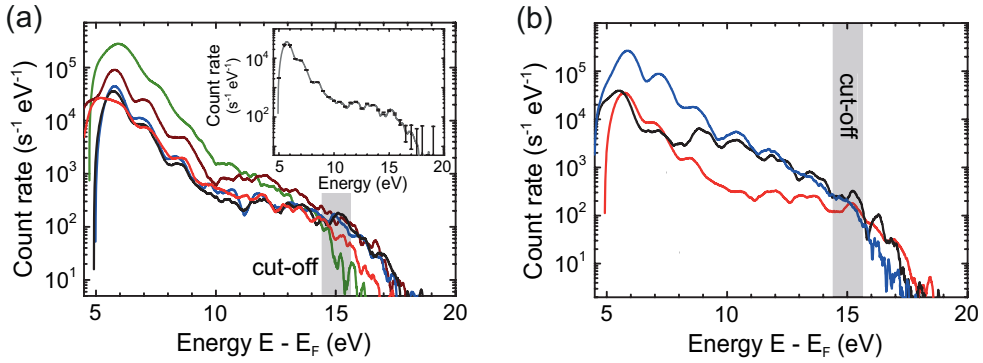

Figure 3.5: Electron energy spectra displaying a rescattering plateau for different tip radii and tip materials. The cut-off is adjusted to occur at the same kinetic energy by tuning the incident laser intensity. (a) Data for the tunsten tip (red: 8 nm, black: 14 nm, blue: 15 nm, brown: 19 nm, green: 51 nm). Inset: Spectrum of the 14 nm tip with error bars (standard deviation). (b) Gold tip (blue: 28 nm, black: 31 nm, and red: 46 nm). Taken from [108].

by field ion microscopy and gradually blunten the tip by field evaporation (see Fig. 3.3). To obtain a data point at around $r = 50$ nm radius of curvature we blunten the tip further by heating and take scanning electron micrographs ex-situ after the experiment to determine the radius of curvature. We prepare three gold tips and perform field ion microscopy and field evaporation in the chamber to ensure a smooth clean crystal. As the resolution of the field ion microscope negates in-situ ring-counting in this case, we determine the radius of curvature ex-situ by scanning electron micrographs after the photoemission experiments

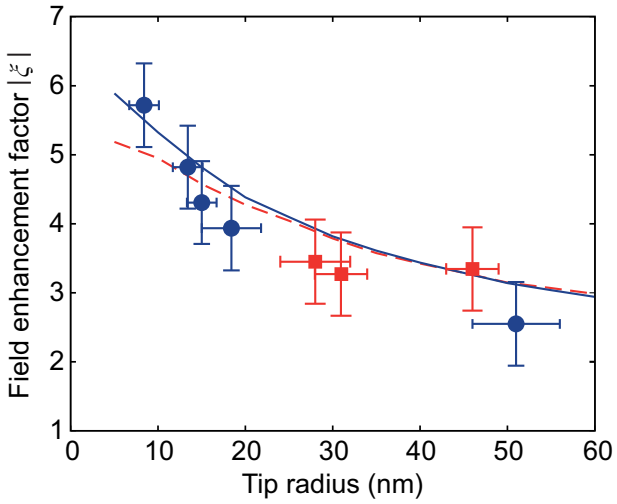

Figure 3.6: Absolute value of the field enhancement factor $|\xi|$ as a function of tip radius. Lines correspond to FDTD simulations with tip opening angles of 5° for tungsten (blue solid line) and 0° for gold (red dashed line). Experimental values for tungsten (blue circles) and gold (red squares) coincide well with the simulations. Modified from [108].

for all three tips, see Fig. 3.4.

For all tip radii and materials we observe a plateau in electron spectra caused by rescattered electrons and we adjust the incident laser intensity such that the cut-off of the plateaus for different tips is at the same position, see Fig. 3.5. Thereby we avoid exceeding the range of accessible kinetic energies of our electron spectrometer and along the way mitigate effects of possible imperfections in its spectral response. While we observe that the relative ratio of rescattered electrons to direct electrons varies between the experiments due to the different tip shapes, all spectra allow the determination of a distinct cut-off.

From the cut-off and the present bare laser intensity we extract the field enhancement factor $|\xi|$ as a function of tip material and tip radius r, the main result of the measurements presented here. We obtain field enhancement factors of 6 to 2.5 for tip radii from 8 to 51 nm, see Fig. 3.6. For both tip materials the observed field enhancement factors are comparable and agree very well with completely independent FDTD simulations of the respective tips.

3.1.3 The origin of field enhancement and comparison to literature

We interpret the smooth increase of field enhancement with decreasing tip radius as a geometrical effect of the discontinuity of the dielectric function leading to field enhancement, contrary to plasmon or antenna resonances. The sharp structure leads to the accumulation of surfaces charges at the apex, similar in nature to the electrostatic lightning-rod effect. Compared to other published results of field enhancement from tips evaluated from second harmonic emission, photoemission, or simulation, our data for tungsten agrees well with experimental [105, 122] and theoretical [122, 123] values. For gold, the reported values diverge considerably and some authors report much higher field enhancement factors in experiment [12, 105] and theory [104, 123]. With high likelihood the deviations can be attributed to two effects. First, the field enhancement is sensitive to atomic-scale details of the structure that have not been controlled in other experiments. Second, simulations have recently predicted a strong dependence of the field enhancement on the opening angle of the shank of the tip [124]. This fact should also significantly contribute to the large discrepancy in the literature, as different electrochemical etching schemes are known to yield different opening angles [87, 125, 126].

Our measurements provide nanoscopic information on the near field. As we measure only forward-emitted electrons the probed volume is on the order of $10\,\mathrm{nm}^3$. Complementarily, maps of localized plasmon resonances have been recorded at gold triangles with electron energy loss spectroscopy (EELS) using a transmission electron microscope with $\approx 1\,\mathrm{nm}$ resolution [127]. Also, the shape of near fields at carbon nanotubes and silver nanowires has been determined with nm spatial resolution with the help of a laser-triggered electron microscope [128]. However, in these experiments the strength of the near field has not been determined. Also, simulations have recently shown that EELS maps cannot directly be interpreted in terms of the photonic local density of states [129].

Recently the field of quantum plasmonics has emerged. It describes the influence of

quantum effects on near fields, and in our case predicts that the spill-out of the electron wavefunctions at the metal-vacuum boundary leads to a screening of the near field. This screening was suggested by simulations to occur close to, but below, the nm-scale [25, 130]. Since our results can be reproduced by classical Maxwell simulations we do not see the influence of quantum effects and have in this sense measured the field enhancement close to the spatial resolution, where a classical field enhancement factor can be meaningfully assigned.

3.2 Reconstruction of near fields in amplitude and phase

As an outlook we briefly discuss an ongoing, conceptually new project that aims to characterize the complete temporal shape of optical near fields in the group of Matthias Kling at the Max-Planck-Institute of Quantum Optics in Garching and Ludwig-Maximilians-Universität München, with whom we are collaborating on this project. We just give the flavour of the experiment here, for details we refer the reader to [109]. The basic setup is shown in Fig. 3.7(a). It relies on the well-established technique of attosecond streaking [8]. A 4.5 fs near-infrared (NIR) pulse centered at 720 nm and an attosecond XUV pulse of duration 220 as and central energy of 95 eV are simultaneously focused onto a gold nanotip in a vacuum chamber with a variable time delay Δt between them. A time-of-flight electron spectrometer records the final kinetic energy of the emitted electrons. By selectively considering only electrons of high kinetic energy, the electrons that are emitted via the photoelectric effect by the XUV beam are separated from the electrons emitted by the near field excited by the near-infrared pulse, as depicted in Fig. 3.7(b). Depending on the time delay between XUV and NIR the XUV photoelectrons are emitted into the near field at different near-field phases. By propagation through this near field, electrons acquire a shift in energy depending on both the near-field phase and amplitude that they are emitted into, see Fig. 3.7(e). From this shift of kinetic energy as a function of pulse-to-pulse delay one can determine the near field in amplitude and phase, see panel (f). The tip can be replaced by a conventional neon gas target for a reference measurement of the exciting NIR and XUV laser pulses. Depending on near-field decay length, XUV energy, and the period of the NIR field, different streaking regimes have to be considered [131]. Our experiment is situated in the ponderomotive regime. This means that the vector potential of the near field can be determined directly by measuring the energy shift as a function of XUV-NIR delay, analogous to streaking from gas targets.

From the measurements we could completely reconstruct the optical near field at the shank of the tip, which dominates the XUV photoelectron count rate due to a much larger surface than the tip apex. A determination of the apex contribution is currently underway. However, already these results represent the characterization of an optical near field on nanometer spatial and attosecond temporal scales.

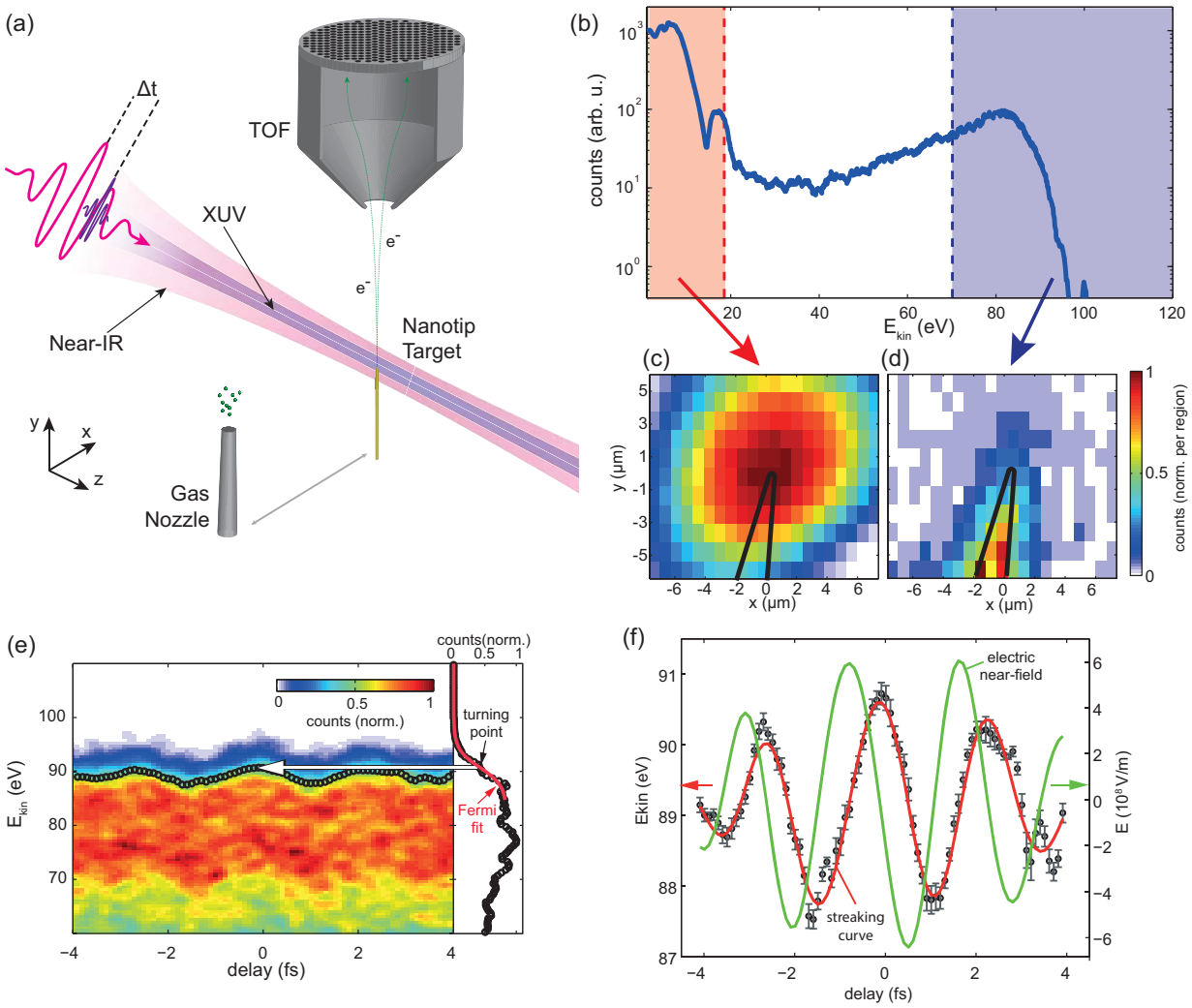

Figure 3.7: Attosecond streaking of near fields at nanotips. (a) Experimental setup. Extreme ultraviolet (XUV) and near-infrared (NIR) pulses are simultaneously focused onto the apex of a gold nanotip. Photoelectrons are detected in a time-of-flight spectrometer (TOF). A gas nozzle allows reference streaking measurements on neon. (b) Recorded photoelectron spectra with both NIR (emitting low-energy photoelectrons, red highlighting) and XUV (emitting high-energy photoelectrons, blue highlighting) present on the tip. The high-energy edge is assigned to the photoemission of 5d electrons. Intermediate photoelectron energies are accessible by rescattering due to the NIR pulse, XUV photoemission from energetically lower-lying states, and inelastic scattering of XUV-photoelectrons. (c) NIR photoemission is strongly localized at the apex due to field enhancement. (d) XUV photoelectrons are emitted predominantly from the tip shank, so that we sample the near field at the taper in this experiment. (e) Photoelectron energy as a function of NIR-XUV delay. Clearly, the attainable maximum kinetic energy is modulated, as quantified by Fermi fits (red line) to the high-energy edge. The turning points of these fits are added as black circles to the main figure. (f) Reconstructed near field (green line) from the streaking data (black circles with fit errors) and a fit to the data (red). Figures assembled from [109].

Chapter 4

Time-resolved studies of photoemission at metal nanotips

In this chapter we examine and control the photoemission process from a tungsten nanotip. By inducing photoemission with two laser pulses of variable time delay, we are able to investigate the dynamics governing photoemission. We report on two different studies: First, we consider the case of a fundamental mixed with its second harmonic, which allows to control above-threshold photoemission from the metal tip using the relative phase between the two laser pulses in a Brumer-Shapiro scheme [29]. In a second experiment we examine the lifetime of excited states involved in the photoemission process with enhanced temporal resolution and two pulses of the same frequency. Our studies confine the lifetime of excited states to the femtosecond regime.

4.1 Two-color coherent control of above-threshold photoemission

Here we explore the control of above-threshold photoemission from a tungsten tip in a ω-2ω scheme. We will see that the nanometric size of the tip and in-situ atomic-scale surface control surpass the limitations of focal averaging and inhomogeneous broadening that many gas-phase and surface experiments suffer from. Photoemission induced by a fundamental pulse is perturbed with a weak second harmonic to the extent that the relative phase between the colors modulates the emitted current by 94%. We will see that despite the different final photoelectron energies we can understand the mechanism of control of the total current by considering just two almost perfectly constructively or destructively interfering quantum pathways, each individually leading to electron emission. Finally we compare experimental results to time-dependent density functional theory (TDDFT) simulations. We note that recently a ω-2ω experiment was performed on a silicon tip array [22]. However, the authors report no phase-resolved signal, signifying that coherent control was not achieved.

4.1.1 Principles of coherent control

The advent of the laser [26] introduced light fields of unprecedented intensity and coherence. This sparked much interest in the physical chemistry community to control chemical reactions on a fundamental quantum mechanical level [132]. Two main schemes were initially proposed. Paul Brumer and Moshe Shapiro introduced a frequency domain approach, where interference between quantum pathways is exploited to optimize for the desired product state [27,28]. David Tannor and Stuart Rice pioneered an approach, where the motion of electron wave packets is guided directly in the time domain [133]. When femtosecond pulse shaping became available, Rabitz and Judson [134] proposed a third approach: The use of closed-loop self-learning, so that the optimized control pulse could be found in an iterative scheme, in principle without a priori knowledge of the system that the two other methods profit from. Speaking in terms of these categories, our experiment is part of the frequency-domain approach and we will thus limit our discussion to it in the following.

In one of their seminal papers [29] Brumer and Shapiro proposed control over the transfer of population in a quantum system from an initial state $|i\rangle$ to a final state $|f\rangle$ by simultaneous illumination with fundamental (ω) and third harmonic (3ω), thus creating two quantum pathways for the transition:

$$P_\omega(|i\rangle \rightarrow |f\rangle) = \langle f| \hat{O}_\omega |i\rangle \tag{4.1}$$

$$P_{3\omega}(|i\rangle \rightarrow |f\rangle) = \langle f| \hat{O}_{3\omega} |i\rangle \tag{4.2}$$

Here P_ω and $P_{3\omega}$ denote the probabilities of the transitions along the respective quantum pathways and $\hat{O}_\omega$ and $\hat{O}_{3\omega}$ are the transition operators for the two pathways.

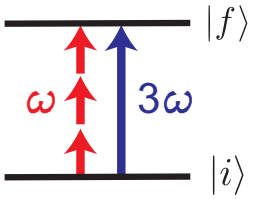

Figure 4.1: Exemplary schematic of two-pathway coherent control from initial to final state with one three photon and one single photon pathway as proposed in the original work of Brumer and Shapiro.

Due to the coherence of laser light, in particular the coherence between a fundamental and its harmonics generated by parametric processes in nonlinear crystals that we discussed in Section 2.1, these pathways can interfere, so that the phase between these pathways $\Delta\Phi$ becomes a control knob in the experiment:

$$P_{tot}(|i\rangle \rightarrow |f\rangle) = P_\omega + P_{3\omega} + 2\sqrt{P_\omega P_{3\omega}} \cdot \cos(\Delta\Phi) \quad . \tag{4.3}$$

$\Delta\Phi$ contains the phase of the laser fields as well as a phase related to the quantum mechanical states involved Φ_{qm} [135]:

$$\Delta\Phi = \Phi_{3\omega} - 3\Phi_\omega - \Phi_{qm} \quad . \tag{4.4}$$

When the pathway probabilities P_ω and $P_{3\omega}$ have comparable amplitude, the scheme allows switching the total transition probability P_{tot} on and off by controlling $\Delta\Phi$.

Since its invention the concept has been generalized and applied to many quantum systems. For example, gas phase chemical reactions [135] and photoemission from gases [136,137,138] have been examined. Also, orientation of molecules by two-color interference has been achieved [139, 140]. At solid targets, the control of currents in semiconductors [141,142], surface currents and photoemission at surfaces [143,144,145], and recently driving of currents in a single nanowire [146] have been reported. Other intriguing applications include control of high harmonic generation [147, 148], THz wave generation in air [149], nonlinear frequency conversion [150, 151], and homodyne detection of weak signals [152].

In our implementation we use two laser pulses: One at fundamental frequency ω and another at the second harmonic 2ω. This is a slight variation on the original gas phase ω-3ω proposal. Speaking in abstract terms, both are taking advantage of interference between N-photon and M-photon routes. Using ω and 3ω both pathways contain an odd number of photons, whereas implementing ω and 2ω the contained photon numbers are different in parity. This reduces control in gas phase experiments to control of the angular distribution of photoelectrons, while the total number of photoelectrons cannot be influenced [153]. However, as symmetry is broken at the tip surface and electrons can only be emitted in forward direction, a ω-2ω scheme will still yield full control over the emitted current, as we shall see in the following.

4.1.2 Experimental setup

In Fig. 4.2 we give a schematic overview of our experimental setup. It can broadly be devided into an optical setup and the UHV chamber containing the sample, which we introduced in Section 2.4, and only briefly discuss here.

The optical setup discussed below provides phase-locked pairs of fundamental (ω) and second harmonic (2ω) pulses, where the intensity of the two colors, the polarization of the second harmonic, and the delay between fundamental and second harmonic can be individually adjusted.

First, the output of a commercial Erbium-doped femtosecond fiber laser and amplifier[1] passes through a free-standing 100 μm thick, type-I phasematched β-barium borate (BBO) crystal cut at 19.8°. We ensure that the ratio of frequency of the second harmonic to fundamental pulse is 2.00 ± 0.01 and the corresponding central wavelengths of fundamental and second harmonic are 1560 nm and 780 nm. With interferometric autocorrelations we determine the pulsewidth of the fundamental to 74 fs and of the second harmonic to 64 fs. Due to the parametric nature of the generation process in the nonlinear crystal, these pulses are phase-locked. Subsequently, the pulses are sent into a home-built Mach-Zehnder interferometer with dichroic beamsplitters[2] to separate the colors to allow individual ma-

[1] Menlo Systems, C-Fibre A

[2] Thorlabs, DMLP1180

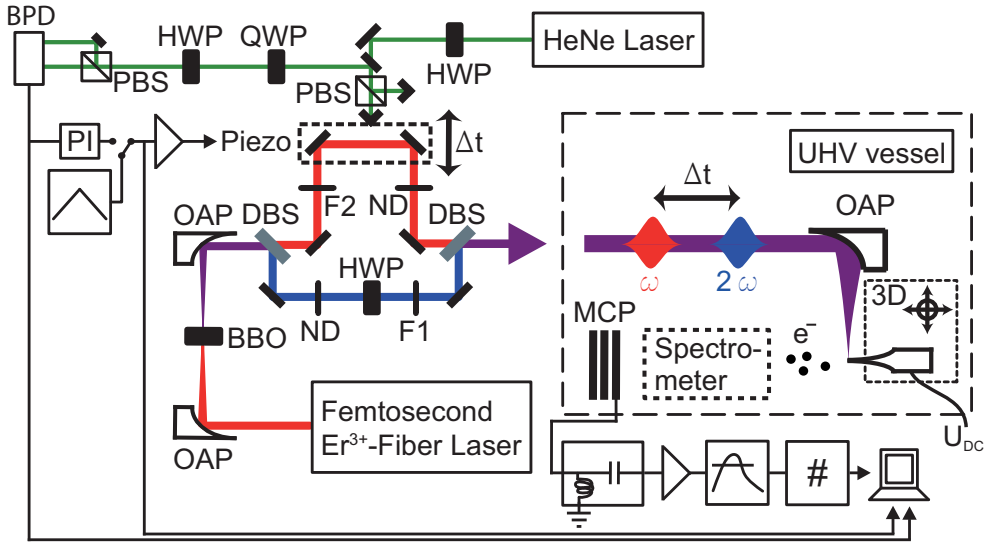

Figure 4.2: Experimental setup for ω-2ω coherent control. The second harmonic of Er^{3+}-doped fiber laser pulses is generated in BBO with off-axis parabolas (OAP) for dispersion-free focusing and collimation. Beams enter a Mach-Zehnder interferometer with dichroic beam splitters (DBS), where the fundamental passes a variable delay stage. Intensities are independently controlled with neutral density filter wheels (ND) and the beams are spectrally filtered (F1, F2). The polarization of the second harmonic is rotated with a half wave plate (HWP). After recombination of the two pulses with variable time delay Δt they are focused onto a tungsten tip with an off-axis parabola (OAP). Electrons are detected on a microchannel plate (MCP) or with a spectrometer using single electron pulse counting. Pulse delay is monitored and controlled with a Helium-Neon laser passing a Michelson interferometer using Pancharatnam's phase. With two half wave plates (HWP), a quarter wave plate (QWP), two polarizing beam splitter cubes (PBS), and a balanced photodetector (BPD) we gain access to the delay with attosecond resolution. Via a proportional-integral controller phase-locking of the interferometer is enabled. Alternatively, an unlocked continuous-scan mode of operation is implemented with a computer-controlled function generator.

nipulation. Color[3] and interference filters[4] ensure clean separation of the two colors[5], as even small admixtures of e.g. fundamental light in the second harmonic arm strongly affect the measured photoemission rate due to optical interference. Intensities of the beams are adjusted with neutral density filter wheels[6]. A half wave plate[7] in the 2ω arm allows to rotate the 2ω polarization, which is chosen to align with the fundamental polarization unless stated otherwise.

A variable delay stage equipped with a piezo stack[8] allows to introduce a ω to 2ω

[3]Thorlabs, FGL9
[4]Thorlabs, FEL1150
[5]Experimental upper limit for leakage intensity/intentional intensity admixture for both colors: 10^{-4}
[6]Thorlabs, NDC-50C-2M
[7]Bernhard Halle Nachfl. GmbH, $700 - 2500\,\mathrm{nm}$
[8]Spindler and Hoyer

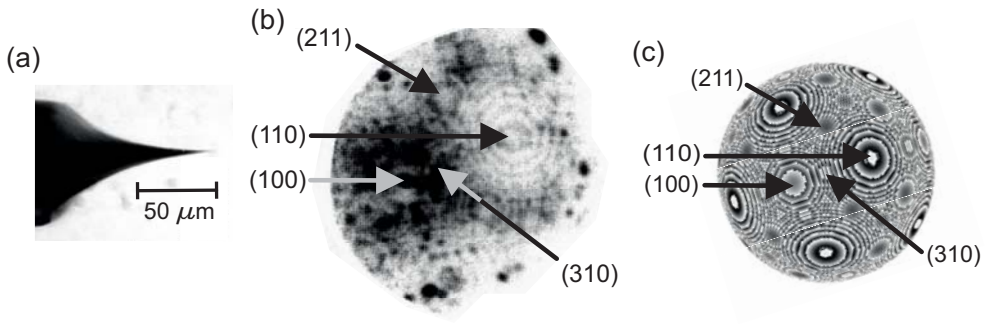

Figure 4.3: Tungsten nanotip used as an electron emitter. (a) Optical microscope image of the tip. (b) Field ion microscopy image of the tip's apex. (c) Ball model of the apex of a (310) tungsten tip adapted to the image in (b) revealing different crystallographic planes. By counting the number of atomic steps between the (110) plane and the (211) plane the tip radius is determined to $r = (10.2 \pm 1.7)$nm.

delay Δt of up to 2 picoseconds. A Michelson interferometer operated by a Helium-Neon laser[9] serves to optically measure the position of the delay stage. For this reason one end retroreflector[10] of the Michelson interferometer is mounted onto the delay stage, while the other one is fixed. The piezo stack can either be operated with a computer-controlled DaQ card and a home-built high-voltage amplifier - usually with a triangular pattern for a continous delay scan - or alternatively locked at a certain value by a home-built analogue proportional-integral controller. As the measured delay value is encoded in the optical polarization, rotating the half wave plate in the reference interferometer setup allows for moving the phase-locked two-color interferometer [154]. The differential photocurrent of the home-built balanced photodiode and the piezo driving voltage are recorded together with the observed electron emission. This allows post-processing of measured delay scans onto an equidistant axis Δt with a MATLAB routine, which the nonlinear piezo response renders necessary.

The laser pulses are directed into the UHV chamber (base pressure of $5 \cdot 10^{-10}$ hPa) and focused with an off-axis parabolic mirror onto the apex of a (310)-oriented tungsten nanotip. The tip's radius of curvature is (10.2±1.7) nm, determined in situ by field ion microscopy [92], see Fig. 4.3. The photoemitted current is either determined spectrally integrated with the microchannel plate (MCP) detector or alternatively spectrally resolved with the retarding-field high-pass filter and subsequent counting, as described in Section 2.4. The tip bias field is $0.3 - 0.5$ GV/m in the following experiments.

[9] Melles-Griot, 05-LHP-271-299
[10] Thorlabs, PS974-A

4.1.3 Two-color control of photoemission from a W(310) tip

To determine the expected photoemission mechanism for each of the colors alone in the absence of any excited state we evaluate the Keldysh parameters γ_ω and $\gamma_{2\omega}$. We include the expected field enhancement factor of 7 and 6 for fundamental and second harmonic, respectively, and take into account the work function for the (310) facet of tungsten of 4.31 eV [86]. For the parameters of our study we obtain minimum Keldysh parameters $\gamma_\omega = 4.8$ for the fundamental and $\gamma_{2\omega} = 53$ for the second harmonic, thereby placing photoemission with both colors in the multiphoton regime. Conceptionally, the second harmonic is a weak perturbation with a typical ratio of second harmonic ($I_{2\omega}$) to fundamental (I_ω) near-field peak intensity $I_{2\omega}/I_\omega \leq 4\%$. Electron emission by the fundamental alone is for the range of our parameters always more than one order of magnitude, usually more than two orders of magnitude, larger than electron emission by the second harmonic alone.

In temporal overlap of the ω and 2ω pulses on the tip we observe a strong change in the emission characteristics, which we refer to as 'cooperative signal'. For illustration Fig. 4.4 shows scans of the delay Δt between ω and 2ω for increasing second harmonic intensities. For low 2ω intensities the electron count rate is symmetrically modulated, whereas for higher intensities electron emission in temporal overlap of the two pulses is in general enhanced and on top strongly modulated.

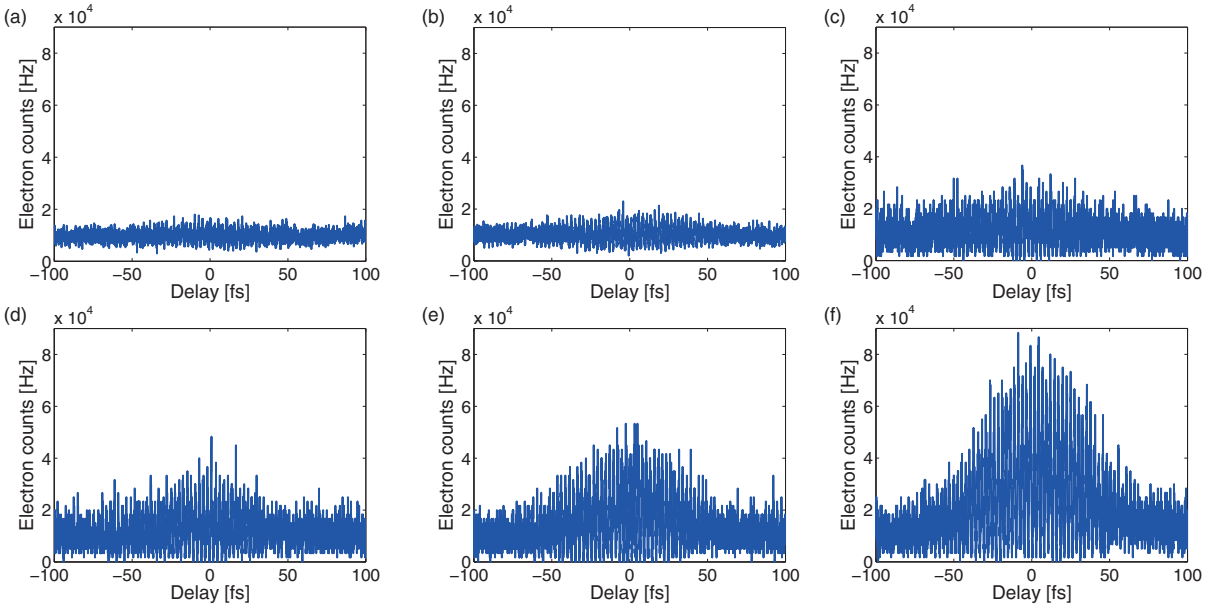

Figure 4.4: Emitted electron current as a function of delay between ω and 2ω pulse for $I_\omega = 330\,\mathrm{GW/cm^2}$. For positive values of delay the 2ω pulse encounters the tip first. (a) $I_{2\omega} = 0.23\,\mathrm{GW/cm^2}$, (b) $I_{2\omega} = 0.78\,\mathrm{GW/cm^2}$, (c) $I_{2\omega} = 1.6\,\mathrm{GW/cm^2}$, (d) $I_{2\omega} = 3.1\,\mathrm{GW/cm^2}$, (e) $I_{2\omega} = 6.6\,\mathrm{GW/cm^2}$, (f) $I_{2\omega} = 14\,\mathrm{GW/cm^2}$. Evidently, electron emission is strongly modified by two simultaneously present pulses.

In Fig. 4.5 we discuss our observations quantitatively. In (a) we display a delay scan for $I_\omega = 330\,\mathrm{GW/cm^2}$ and $I_{2\omega} = 6.6\,\mathrm{GW/cm^2}$. The average count rate is enhanced and oscillates sinusoidally as a function of the delay, magnified in panel (d). The modulation is very pronounced, so that electron emission is either drastically enhanced or reduced as compared to the case of temporally nonoverlapping laser pulses. Despite the very weak 2ω admixture the achievable electron current in temporal overlap is four times higher than outside of temporal overlap.

For further analysis we Fourier transform our data and exemplarily show the spectrum in Fig. 4.5(b) as the Fourier transform of the data in Fig. 4.5(a). The cooperative signal of the two pulses contains two main contributions: A low-frequency component in region of interest 0 (ROI 0) and an oscillatory component in ROI 1 peaking at 390 THz, the

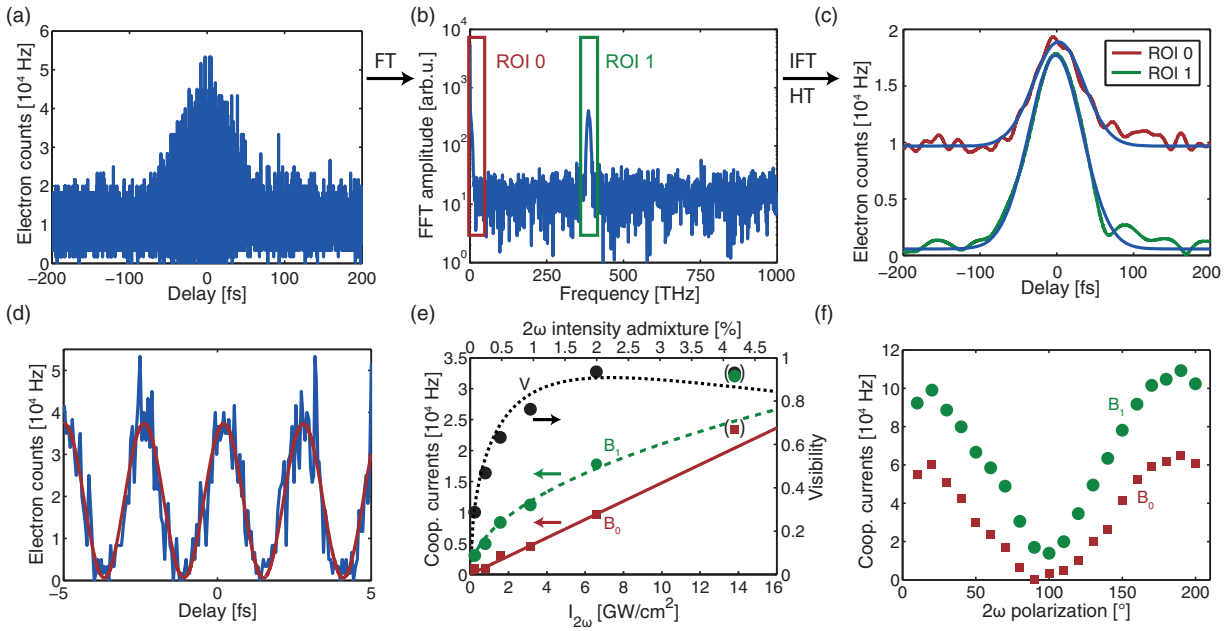

Figure 4.5: Experimental data. (a) Electron current as a function of delay between ω and 2ω pulse for $I_\omega = 330\,\mathrm{GW/cm^2}$ and $I_{2\omega} = 6.6\,\mathrm{GW/cm^2}$. For positive values of delay the 2ω pulse encounters the tip first. (b) Absolute value of the Fourier transformation (FT) of the data in (a). A low-frequency part (ROI 0) and an oscillatory part at 2f (ROI 1) constitute the cooperative signal. (c) Inverse Fourier transform (IFT) of ROIs and subsequent Hilbert transform (HT) of ROI 1 signal to extract the signal envelope, separating the contributions. Gaussian fits are shown in blue. (d) Magnification of the central area of (a) (blue line) together with a sine-fit (red line). (e) ROI amplitude fit parameters B_0 and B_1 as a function of the second harmonic intensity for a fundamental intensity of $I_\omega = 330\ \mathrm{GW/cm^2}$. B_0 and B_1 are proportional to $I_{2\omega}$ (red solid line) and $\sqrt{I_{2\omega}}$ (green dashed line), respectively. The contrast (visibility) of the current oscillation calculated using Eq. 4.6 (black dots) and Eq. 4.16 (black dotted line) reaches up to 94% in this experiment. (f) B_0 (red squares) and B_1 (green spheres) (see text) as a function of the rotation angle θ of the polarization direction of the second harmonic with respect to the tip axis and the fundamental field for $I_\omega = 410\,\mathrm{GW/cm^2}$ and $I_{2\omega} = 13\,\mathrm{GW/cm^2}$.

frequency of the second harmonic. To elucidate the origin of these signal components we cut the data around the respective ROI ($0-50$ THz for ROI 0 and $370-410$ THz for ROI 1) and perform an inverse Fourier transform and for ROI 1 additionally a Hilbert transform to extract the envelope of the oscillation (see Fig. 4.5(c)). These contributions can be well approximated by Gaussian fits of the form

$$G_i(\Delta t) = A_i + B_i \exp\left(-\frac{4\ln(2)\Delta t^2}{\mathrm{FWHM}_i^2}\right) \tag{4.5}$$

for all second harmonic admixtures. Here $i = 0, 1$ for ROI 0 and ROI 1, Δt is the ω-2ω delay, and FWHM_i are the full widths at half maximum of the signals, which contain the widths of the temporal overlap of the pulses and the response of the tip. The fit parameters B_i serve as direct measure of the cooperative effect in the region of temporal overlap. It is important to note that we find that B_0 and B_1 scale differently with the second harmonic intensity $I_{2\omega}$. While B_0 increases linearly with $I_{2\omega}$, B_1 shows a $\sqrt{I_{2\omega}}$ dependence, see Fig. 4.5(e). This is also visible in Fig. 4.4, where the oscillatory component dominates the cooperative signal for small second harmonic admixtures. The visibility of the oscillating current signal

$$V = \frac{N_{\max} - N_{\min}}{N_{\max} + N_{\min}} \tag{4.6}$$

reaches up to 94% for an intensity admixture of the 2ω-component of 2% to the fundamental pulse at $I_\omega = 330$ GW/cm^2. For admixtures of 4% an additional Fourier component at 4ω emerges from the white-noise background, indicating the onset of a new interaction process. We therefore exclude the data point at $I_{2\omega} = 14$ GW/cm^2 from the analysis.

We have also measured the variation of the electron emission as a function of the orientation of the linear polarization of the second harmonic pulse, displayed Fig. 4.5(f). Maximum cooperative signal is found for the 2ω component aligned with the tip axis and

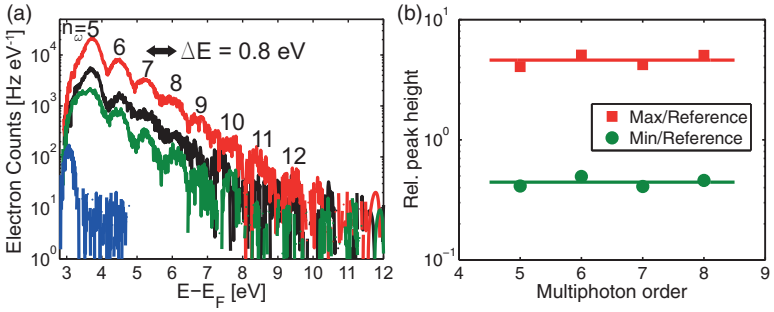

Figure 4.6: (a) Experimental electron spectra for $I_\omega = 410\,\mathrm{GW/cm^2}$ and $I_{2\omega} = 13\,\mathrm{GW/cm^2}$. Blue: 2ω pulse alone. Black: ω pulse alone. Red: ω and 2ω pulses, with relative phase locked at emission maximum. Green: ω and 2ω pulses with rel. phase locked in emission minimum. (b) Multiphoton peak heights for two-color illumination with relative phase set for maximum (red curve in (a)) and minimum (green in (a)) emission divided by the corresponding heights for fundamental illumination only. Solid lines show horizontal line fits.

parallel to the ω component ($\theta = 0°$). With increasing angle θ the cooperative signals are reduced and reach their minimum for $\theta = 90°$ (perpendicular to the tip axis). This is expected for two reasons: Perpendicularly polarized light moves the region of near-field enhancement to the edges of the tip apex [110], i.e., away from the low work function (310) direction, lowering emission. Moreover, the resulting reduced overlap of the ω and 2ω near fields is expected to diminish the cooperative effect.

To gain further insight into the relevant processes we record electron spectra shown in Fig. 4.6(a). We first turn our attention to electron spectra for fundamental and second harmonic alone (black and blue). While we observe only two-photon photoemission for the second harmonic, we see many above-threshold photoemission orders in the spectrum of the fundamental, where the lowest (i.e. fourth) order is suppressed due to the nonnegligible ponderomotive energy of 0.1 eV for the fundamental intensity (channel closing) [14]. We confirmed experimentally that a lower fundamental intensity recovers this peak. For spectra with both ω and 2ω present and the pulse delay locked to minimum (green) and maximum (red) of total emission, we observe that all photon orders display minimum and maximum of their individual rate for the same delay. Also, we show in Fig. 4.6(b) that every multiphoton peak has the same relative magnitude compared to the case of emission with the fundamental alone.

4.1.4 Quantum pathway interference model

Having presented the experimental data we will now discuss a quantum pathway model to explain our findings. We propose that for each photon order two ionization pathways exist, where one involves absorption of n fundamental photons and the other absorption of $n-2$ fundamental photons and 1 second harmonic photon (see Fig. 4.7). The observed oscillations when varying the time delay are manifestations of the coherence of these two pathways. In the following we model the total emitted current.

The electron spectra for the two-color case show multiple photon orders. Therefore the total electron emission rate R_{tot} is given by the sum over all photon orders:

$$R_{\mathrm{tot}} = \sum_{n=4}^{\infty} r_n \ , \tag{4.7}$$

where r_n is the emission rate for each photon order.

With the proposed two interfering pathways this evaluates further to:

$$R_{\mathrm{tot}} = \sum_{n=4}^{\infty} p_n \cdot (\alpha^2 I_\omega^2 + \beta I_{2\omega} + 2\sqrt{\alpha^2\beta} I_\omega \sqrt{I_{2\omega}} \cdot \cos(\phi_{2\omega} - 2\phi_\omega - \phi_{qm,n})). \tag{4.8}$$

Here the term $\alpha^2 I_\omega^2$ belongs to the pathway with the absorption of two fundamental photons, the term $\beta I_{2\omega}$ is the pathway with the absorption of a single second harmonic photon, and $2\sqrt{\alpha^2\beta} I_\omega \sqrt{I_{2\omega}} \cdot \cos(\phi_{2\omega} - 2\phi_\omega - \phi_{qm,n})$ is the interference term. p_n denotes the probability that the electron acquires the remaining necessary energy from fundamental photons

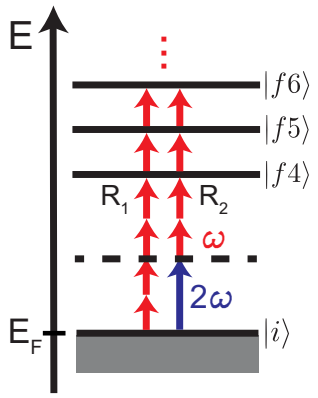

Figure 4.7: Multipath interference: Schematic of the relevant emission pathways R_1 and R_2 in multiphoton photoemission originating from initial states $|i\rangle$ close to the Fermi energy E_F to final states $|fn\rangle$, $n \in \mathbb{N} \wedge n \geq 4$. One conceivable intermediate state, via which electron emission could proceed is shown dashed.

to reach the final energy and the detector. This factor may also contain strong-field effects, such as peak suppression.

Experimentally we observe that all photon orders have maxima and minima at the same relative optical phase $\phi_{2\omega} - 2\phi_\omega$ (see Fig. 4.6) and that therefore the contribution of $\phi_{qm,n}$ is independent of n.

$$R_{\text{tot}} = (\alpha^2 I_\omega^2 + \beta I_{2\omega} + 2\sqrt{\alpha^2\beta} I_\omega \sqrt{I_{2\omega}} \cdot \cos(\phi_{2\omega} - 2\phi_\omega - \phi_{qm})) \cdot \sum_{n=4}^{\infty} p_n \tag{4.9}$$

Without the second harmonic $I_{2\omega} = 0$ only the pathway remains that contains exclusively fundamental photons:

$$R_{\text{tot},I_{2\omega}=0} = \alpha^2 I_\omega^2 \cdot \sum_{n=4}^{\infty} p_n \quad . \tag{4.10}$$

Experimentally we measure electron emission from the nanoemitter as a function of light intensity when only fundamental hits the tip and find that it scales with I_ω^4, see Fig 4.8. We therefore identify

$$\sum_{n=4}^{\infty} p_n = \alpha^2 I_\omega^2 \tag{4.11}$$

to obtain

$$R_{\text{tot}} = \alpha^4 I_\omega^4 + \alpha^2\beta I_\omega^2 I_{2\omega} + 2\sqrt{\alpha^6\beta} I_\omega^3 \sqrt{I_{2\omega}} \cdot \cos(\phi_{2\omega} - 2\phi_\omega - \phi_{qm}) \quad . \tag{4.12}$$

Equation 4.12 has the form of two interfering emission pathways: Pathway 1 with rate R_1 for electron emission corresponds to the absorption of four photons of the fundamental,

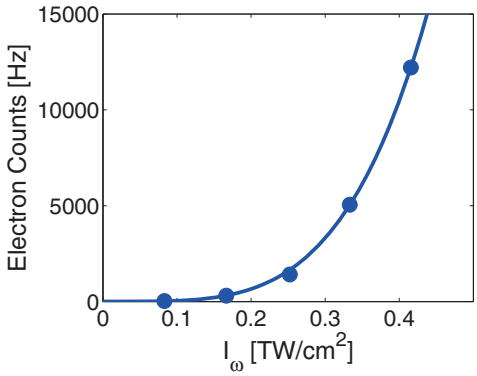

Figure 4.8: Emitted electron current with only fundamental present on the tip as a function of fundamental intensity I_ω (blue dots). The blue line is a fit to the data with $A \cdot I_\omega^4$.

since the total current from fundamental alone scales with I_ω^4, where I_ω represents its peak intensity. In pathway 2, absorption of two photons of the fundamental and one photon of the second harmonic results in electron emission with rate R_2. R_{12} denotes the interference term between R_1 and R_2, which oscillates with the relative phase between the pathways $\phi(\Delta t) = \phi_{2\omega} - 2\phi_\omega - \phi_{qm} = \frac{2\pi\Delta t}{T_{2\omega}} - \phi_{qm}$ that we control with the pulse delay Δt. $T_{2\omega}$ is the period of second harmonic light and ϕ_{qm} denotes the unknown phase contribution of the electronic states connected by the optical transition. With this picture in mind we expect the following dependences on intensities:

$$R_1 = \alpha^4 \cdot I_\omega^4 \tag{4.13}$$

$$R_2 = \alpha^2\beta \cdot I_{2\omega} I_\omega^2 \tag{4.14}$$

$$R_{12} = 2\sqrt{R_1 R_2}\cos(\phi) = 2\sqrt{\alpha^6\beta} \cdot \sqrt{I_{2\omega}} I_\omega^3 \cos(\phi), \tag{4.15}$$

where α^4 and $\alpha^2\beta$ are the respective scale factors for emission along pathway 1 and 2, which in this model also determine the magnitude of the oscillatory term. We can now identify the cooperative signal in ROI 0 with pathway R_2 and the signal in ROI 1 with R_{12}.

In the following we quantitatively compare the observed scaling behavior of the cooperative signals in total current with the quantum-pathway interference model. Evaluating R_1 and therefore α^4 from the observed count rate with fundamental alone at $I_\omega = 330\,\mathrm{GW/cm^2}$ we extract $\alpha^4 = (8.068 \pm 0.080) \cdot 10^{-43}\,\mathrm{Hz\,cm^8\,W^{-4}}$. Evaluating R_2 for extracting $\alpha^2\beta$ from the scaling of the ROI 0 cooperative signal with second harmonic intensity in Fig. 4.5(f) yields $\alpha^2\beta = (1.22 \pm 0.15) \cdot 10^{-29}\,\mathrm{Hz\,cm^6\,W^{-3}}$. Using these two values we obtain the expected scale factor for the interference term R_{12}: $2\sqrt{\alpha^6\beta} = (6.27 \pm 0.38) \cdot 10^{-36}\,\mathrm{Hz\,cm^7\,W^{-3.5}}$. The experimentally observed prefactor for the scaling of the oscillatory part, independently extracted from the scaling of the signal in ROI 1 with $I_{2\omega}$ (Fig. 4.5(e)), is $2\sqrt{\alpha^6\beta} = (5.70 \pm 0.52) \cdot 10^{-36}\,\mathrm{Hz\,cm^7\,W^{-3.5}}$. We note the very good agreement of the two values indicating that the simple model correctly describes the scaling behavior. We can therefore evaluate the visibility of the interference fringes

via:

$$V(I_\omega, I_{2\omega}) = \frac{R_{12}}{R_1 + R_2} = \frac{2\sqrt{\alpha^6\beta}\sqrt{I_{2\omega}}I_\omega^3}{\alpha^4 I_\omega^4 + \alpha^2\beta I_{2\omega} I_\omega^2}\,. \tag{4.16}$$

Fig. 4.5(e) shows $V(I_\omega, I_{2\omega})$ with the experimental data points. The agreement is excellent.

Summarising, we have proposed a model of two interfering quantum pathways for each photon order. Subsequently, with the help of our spectrally-resolved observations, we could simplify the modelling of the total current by just considering two interfering effective quantum pathways. The scaling of the cooperative signal contributions with second harmonic intensity and the sinusoidal variation of the phase-dependent current are in excellent agreement with this model and even quantitatively fit the data. The 94%-contrast we observe in our measurements is amongst the highest values reported for coherent control experiments [151]. This fact is surprising due to the complexity of the solid state. We attribute this to the advantage that we use just a single, sub-wavelength, nanoemitter and thereby surpass all effects related to inhomogeneous broadening and focal averaging. In gas phase experiments, for example, particularly the Gouy phase shift and varying intensities over the focal spot pose challenges. At surfaces, surface roughness is an additional problem, which we surpass with field-ion microscopy and field evaporation.

4.1.5 The influence of excited states

In our analysis we have so far not needed to include the presence of unoccupied states in the metal above the Fermi energy E_F and before we consider excitation of electrons to these unoccupied states we note that the interference mechanism stated above is valid with and without the presence of excited states.

We first approach the matter from the side of simulations, performed by our colleagues at TU Vienna in the group of Joachim Burgdörfer. A series of time-dependent density functional theory (TDDFT) calculations of the experimental situation, a two-color field incident on a 1D-jellium with a work function matched to W(310), reproduces high-contrast oscillations of the count rate as a function of phase delay for optimized parameters. However, the simulations do not reproduce the sinusoidal variation of count rate with phase delay that is apparent from the experiment, as shown in Fig. 4.9. Rather they yield results closer to the expectations for tunneling of electrons through the surface barrier according to Equation 2.27. Also the simulated scaling of cooperative signals does not match well with the observed scaling of $\propto \sqrt{I_{2\omega}}$ for the oscillatory part and $\propto I_{2\omega}$ for the DC part. Instead both signal components scale almost linearly with $I_{2\omega}$ in the TDDFT simulation. This qualitative disagreement between experiment and TDDFT is surprising, since this line of simulations compared well with photoemission from tungsten tips in previous studies [118, 119].

An important simplification in the performed TDDFT simulations is a jellium density of states. To resolve the discrepancy our colleagues performed density functional theory (DFT) simulations to determine the density of states at the surface and in the the bulk of W(310), see Fig. 4.10. In fact the local density of states is strongly modulated compared

to the jellium $\sqrt{E}$ density of states and the strongest deviation is a peak at $E_F + 4\hbar\omega$ in the bulk. These states may resonantly enhance multiphoton processes, so that multiphoton processes are underestimated in the jellium simulation compared to the experiment, explaining the discrepancy.

Experimentally we can get insight into excited states by their lifetime. The first pulse of the two-pulse sequence may create excited electrons, resulting in a higher probability for the second pulse for photoemission during the lifetime of excited electrons. We note that besides electron-electron scattering escape to the bulk can be a very efficient loss mechanism on femtosecond time scales, too. When the excited electron wavefunction is mostly localized in the bulk it can effectively escape detection in photoemission experiments.

We analyse the temporal full width at half maximum (FWHM) of the cooperative signals for different intensities of the second harmonic with Gaussian fits to the data as in Fig. 4.5(c). Independent of second harmonic intensity we obtain $\mathrm{FWHM}_0 = 78 \pm 10\,\mathrm{fs}$ for ROI 0 and $\mathrm{FWHM}_1 = 84 \pm 10\,\mathrm{fs}$ for ROI 1. As comparison we estimate the expected width of the signals in the absence of an excited state lifetime following the quantum pathway model. We remind ourselves that the total current in the absence of a second harmonic scales $\propto I_\omega^4$, so that the ROI 0 signal should scale $\propto I_\omega^2 I_{2\omega}$ and the ROI 1 signal should scale $\propto I_\omega^3 \sqrt{I_{2\omega}}$. Taking into account the involved exponents, we therefore estimate the durations of the cooperative signals using the laser FWHM pulse durations τ_ω and $\tau_{2\omega}$ as

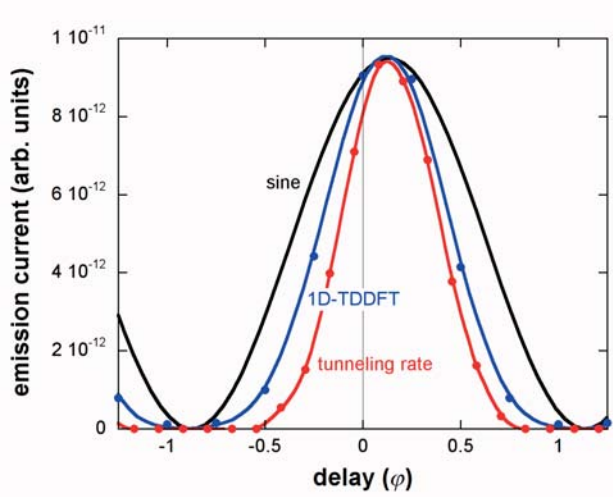

Figure 4.9: Comparison of the dependence of emitted electron current on the phase between fundamental and second harmonic for different models. The experimentally observed sine-shape that is also expected from the interference of quantum pathways is depicted as black line. The result of a 1D TDDFT simulation is shown in blue and emission only allowing tunneling through the surface barrier in red. Simulations were performed for $I_\omega = 330$ GW/cm^2 and $I_{2\omega} = 6.6$ GW/cm^2. Courtesey of Ch. Lemell.

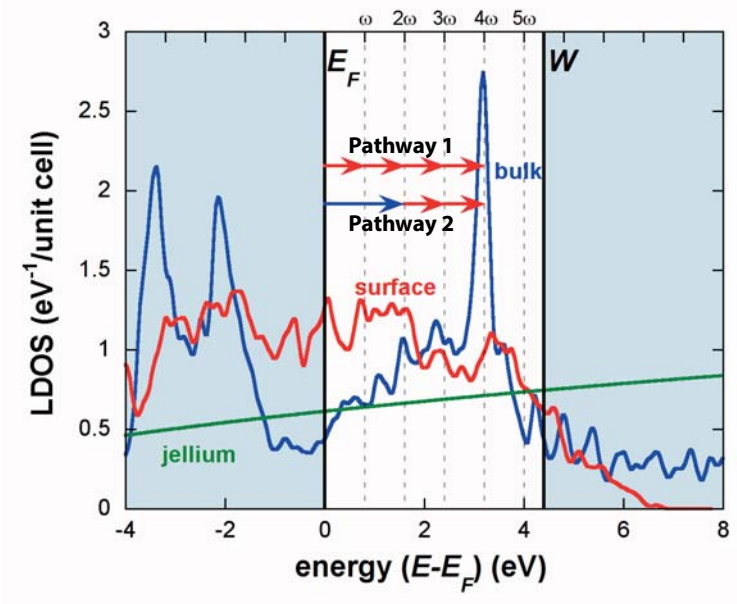

Figure 4.10: Local density of states of W(310) from slab calculations (20 layers) at the surface (red line), for jellium (green line), and from a bulk calculation (blue). Possible pathways to intermediate surface and volume states are indicated by arrows. Courtesey of F. Libisch and Ch. Lemell.

follows:

$$\mathrm{FWHM}_{0,\mathrm{model}} = \sqrt{\left(\frac{\tau_\omega}{\sqrt{2}}\right)^2 + \tau_{2\omega}^2} \tag{4.17}$$

$$\mathrm{FWHM}_{1,\mathrm{model}} = \sqrt{\left(\frac{\tau_\omega}{\sqrt{3}}\right)^2 + \left(\tau_{2\omega}\cdot\sqrt{2}\right)^2} \quad . \tag{4.18}$$

We obtain $\mathrm{FWHM}_{0,\mathrm{model}} = (83 \pm 9)\,\mathrm{fs}$ and $\mathrm{FWHM}_{1,\mathrm{model}} = (100 \pm 10)\,\mathrm{fs}$. Within our error bars both values agree with the experimental values. If there were an excited state of appreciable lifetime involved in our experiment, it should show as a broader experimental value FWHM_0 compared to the prediction $\mathrm{FWHM}_{0,\mathrm{model}}$ [76], since one laser pulse could create an excited state population that the other pulse could subsequently emit. However, these values agree well, so that emission is within our resolution instananeous. In addition we see no shift in signal maximum between ROI 0 and ROI 1, nor an asymmetry of the signals with respect to $\Delta t = 0$. Both observations also indicate that electron emission is instanenous within the experimental resolution [155]. Therefore, our observations exclude all excited states with a lifetime longer than $\approx 10\,\mathrm{fs}$, for example pure surface image potential states, which are known to have lifetimes of several tens of femtoseconds [156]. The absence of tails of the cooperative signals to ps time scales and the high visibility of the oscillations exclude a hot electron gas as an intermediate step for photoemission [51, 79]. Electron-electron scattering on fs timescales would quickly dephase the electrons with

respect to the laser fields.

We therefore have strong indications from TDDFT and DFT calculations that excited states play a role in our experiment. By analyzing the temporal width of the cooperative signals and comparing them to the expected width in the quantum pathway interference model with the observed scaling, we can experimentally exclude a certain class of states and a heated electron gas as intermediate steps in photoemission and place an upper bound on the lifetime of other involved states within our temporal resolution of about 10 fs.

4.2 Interferometric two-pulse correlation measurements

In order to study the lifetimes of excited states preceding photoemission at the W(310) tip with higher temporal resolution we have set up an interferometric two-pulse correlation (I2PC) measurement [76]. A laser pulse is split into two identical copies in an interferometer and focused onto the tip. The electron emission current is recorded as a function of time delay between the two pulses. This measurement is compared to an interferometric autocorrelation trace, where the nanotip is replaced by a nonlinear crystal and the generated second harmonic is recorded as a function of pulse-to-pulse delay. The response of the nonlinear crystal is parametric and therefore considered to be instantaneous, so that the pulse duration can be estimated from this measurement. Any additional broadening in the photoemission current recorded with the tip therefore has to stem from either the near-field, which we saw in Chapter 3 is not significantly distorted compared to the laser far field, or the photoemission process, in particular from a non-vanishing lifetime of excited states. In this experiment we employ 5.5 fs pulses from a Titanium:Sapphire oscillator[11] with a center wavelength of 800 nm. We thereby improve the temporal resolution of our experiment from ≈ 10 fs in the two-color experiment to ≈ 1 fs in this experiment. Since the photon energy of the Titanium:Sapphire oscillator is the same as that of the second harmonic in the two-color experiment of the last section, our studies explore the ladder of photon steps that we have found in the two-color experiment. We find that despite our temporal resolution of about 1 fs we observe no broadening of the DC component of the autocorrelation trace. This directly places an upper bound on the lifetime of one conceivable excited state. Also it hints that tungsten nanotips may under our conditions be applied as a nonlinear element in autocorrelators to estimate even the shortest pulse durations.

4.2.1 Optical setup and experimental conditions

To simplify interpretation of our data and enable a direct comparison of the photoemission current to the second harmonic signal generated in BBO, we use the static voltage U_{DC} at the tip to induce a surface field of 1.6 GV/m, creating a lowered surface barrier. The static field leads to a reduction of the barrier by $\Delta W = 1.52$ eV. Keeping the work function

[11] VENTEON, PULSE:One CP version

of W(310) of 4.31 eV in mind this means that an electron absorbing two photons is free to escape the metal, see Fig. 4.11(a). In this way our experiment should only probe the lifetime of the state at $E = \hbar\omega$. We verified that the emitted tip current as a function of laser intensity displays a nonlinearity of 2, and therefore scales the same as the second harmonic generation.

We create two identical pulse copies of the Titanium:Sapphire laser pulse in a home-built dispersion-balanced interferometer, see Fig. 4.11(b). Dispersion is managed with glass wedges and double chirped mirrors. A broadband 50:50 beamsplitter[12] is cut with a diamond wire saw and reassembled with one half flipped to result in an equal amount of material for both beams. Delay between the beams is facilitated with a delay stage driven

[12]Layertech, custom fabrication

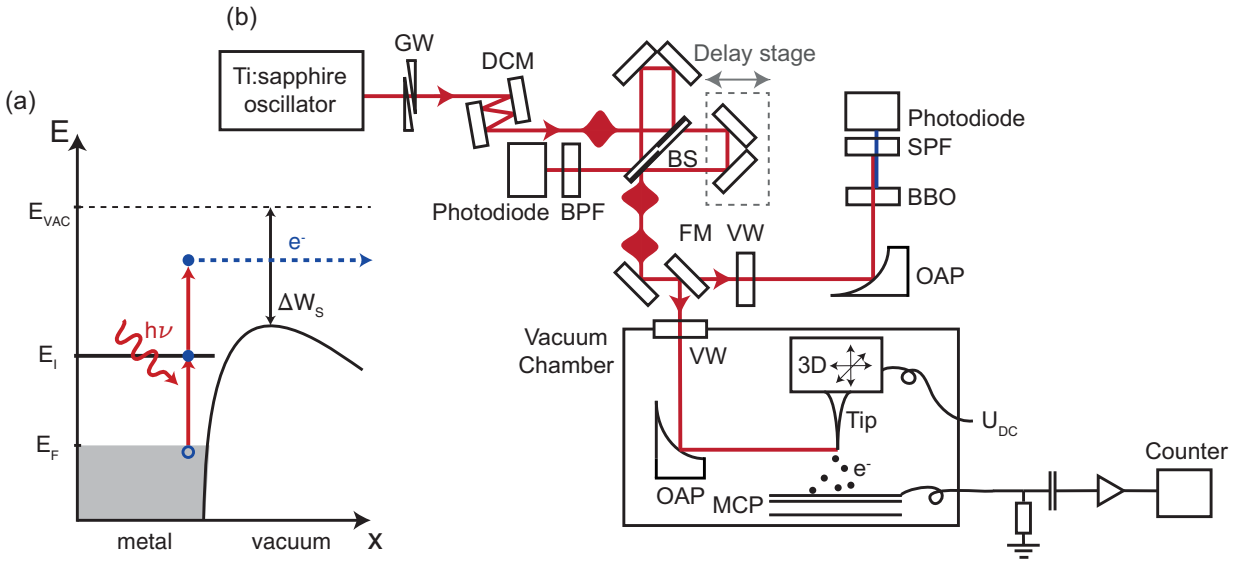

Figure 4.11: (a) Illustration of the photoemission mechanism. Two photons lift the photoelectron to a continuum state via an intermediate state at $E_I = E_F + \hbar\omega$, thereby probing the lifetime of the intermediate state. The Schottky effect lowers the barrier by ΔW_S. (b) Experimental setup for interferometric two-pulse correlation. 5.5 fs pulses from a Titanium:Sapphire oscillator pass glass wedges (GW) and double chirped mirrors (DCMs) for dispersion compensation. They enter a dispersion-balanced interferometer with a broadband beamsplitter (BS). A delay between the pulse copies can be set by a delay stage. A band pass filter (BPF) and a photodiode gauge the translation axis. A flip mirror (FM) sends the pulses either to the photoemission experiment or to a reference measurement with BBO. For photoemission pulses enter the chamber via a vacuum window (VW) and are focused with an off-axis parabola (OAP) onto the tip. Electrons are detected by counting pulses at the front side of the MCP. For the reference measurement the pulses pass an identical copy of the vacuum window (VW) and are focused with an OAP into a 10 μm thick BBO, where the second harmonic is generated. A short-pass filter isolates the second harmonic, which is detected on a photodiode.

by a piezo stepper[13]. A rather narrow band pass filter with a FWHM transmission in the range of (800 ± 10) nm and a photodiode serve to gauge the delay stage. The two pulses with variable delay are via a flip mirror either sent into the vacuum chamber towards the nanotip or towards a reference measurement with a 10 μm thick BBO crystal, where we place a replica of the vacuum window in the beampath. To optimize for the shortest pulse durations and account for different angles of the laser beam passing the viewports (VW), we slightly adjust the glass wedges separately for the shortest trace for BBO and tip. The laser power for the nanotip measurement for both pulses constructively combined is 3.2 mW, which, including an expected field enhancement of 7, translates into a peak intensity of the excited near-field at the apex of $2.5 \cdot 10^{12}\,\mathrm{W/cm^2}$. Photoemitted electrons are detected with the microchannel plate detector via pulse counting, as described in Section 2.4.

4.2.2 Time-resolved data on W(310) tip and interpretation

Our results are summarized in Fig. 4.12. As expected from a nonlinearity of 2, both tip and BBO yield traces with a peak to baseline ratio of 8:1. Apart from a better signal to noise ratio in the case of BBO, the measurements appear very similar on first glance. To gain further insight we perform a Fourier Transform and observe three signal components in the absolute value, see Fig. 4.12(c). We observe that a DC component, a contribution centered at the center frequency of the laser ν, and a contribution at 2ν constitute our data. The three Fourier components give insight into the lifetime of coherence and population of the system under study [76]. Of particular importance for our purposes is the DC component, since it allows us to assess the lifetime of the intermediate state at $E_I = E_F + \hbar\omega = E_F + 1.5\,\mathrm{eV}$. We perform a cut in the Fourier domain and an inverse Fourier transform of the signal components to isolate the respective time-domain signals and plot them in Fig. 4.12(d)-(f). From the traces displayed in panel (d) we extract pulsewidths of (5.5 ± 1.0) fs for tip and (5.4 ± 1.0) fs for BBO under the assumption of an instaneneous nonlinearity and Gaussian pulse profiles. This evaluated pulse duration is in agreement with independent measurements of the pulse duration with the SPIDER technique[14]. If the intermediate state for photoemission had a significant lifetime, it would appear here as additional broadening of the DC trace employing the tip, which we do not observe. We can therefore set an upper bound for the lifetime of the intermediate state at $E = E_F + 1.5\,\mathrm{eV}$ at a (310) tungsten tip in photoemission of ≈ 1 fs. The estimated error arises from statistical fluctuations, and mostly from the uncertainty in gauging the piezo steps with the interferometer. It is likely that the lifetime of the excited state is limited by escape of the excited electron to the bulk, where it can hide from detection in photoemission experiments. This diffusion is considered an efficient loss mechanism at photon energies at or below 1.5 eV in metals [76]. We note that at higher laser intensities a heated electron gas will persist several hundred femtoseconds at tungsten tips [79]. We have so far not

[13]New Focus, 9066M driven by Newport, Picomotor Actuator 8301NF
[14]VENTEON PULSE:FOUR SPIDER

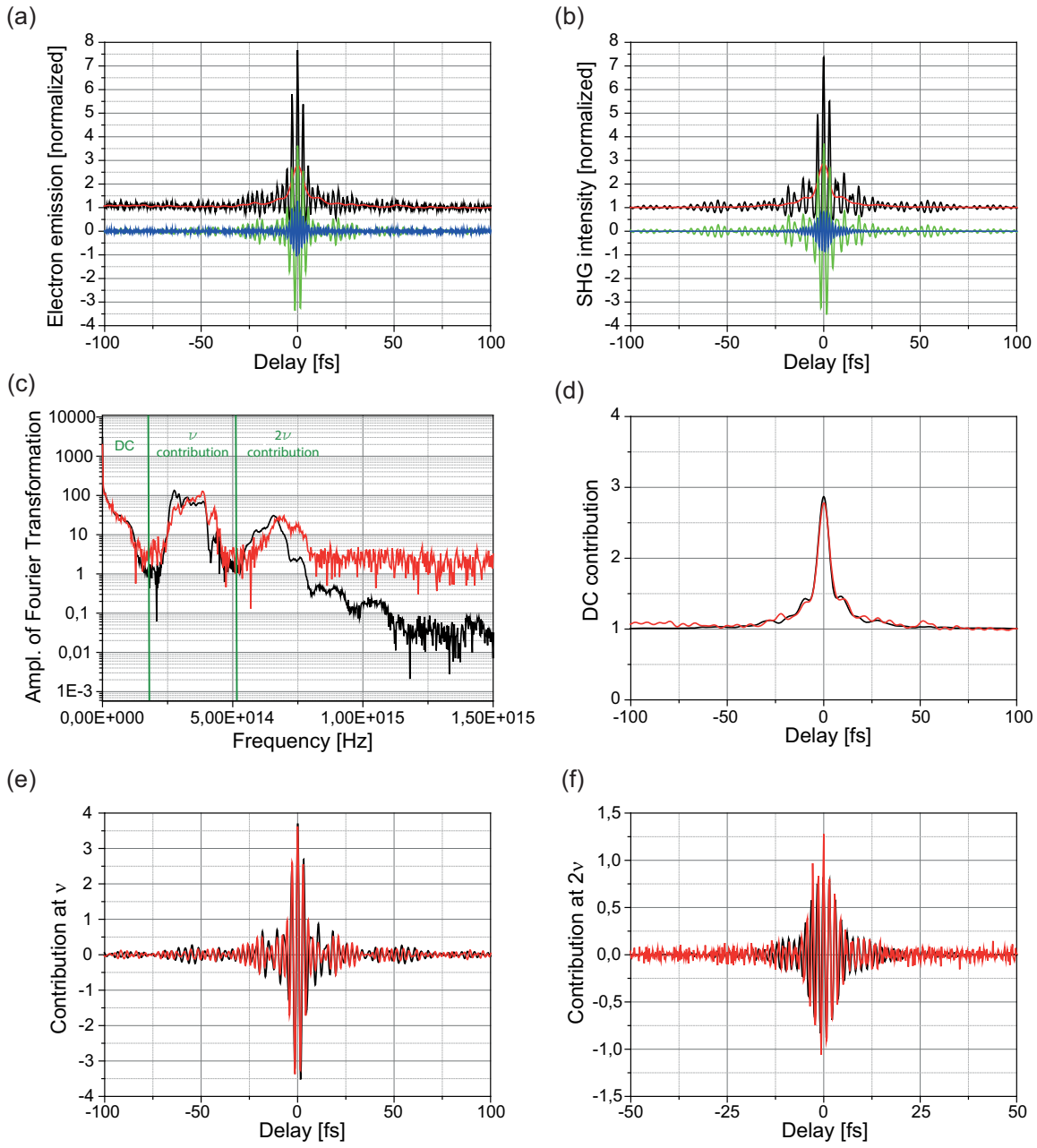

Figure 4.12: Overview of the experimental results. (a) Tip as nonlinearity. On display are the experimental data (black line), as well as the contributions as extracted from filtering by Fourier domain analysis according to (c). Red line: DC component, green line: ν component, and blue line: 2ν component. Due to a slow drift of total count rate the data has been upshifted by 0.1 for better comparison. (b) BBO as nonlinearity, designations are analogous to (a). Black line: Experimental data, red line: DC component, green line: ν component, blue line: 2ν component. (c) Comparison of Fourier amplitude of BBO (black line) with that of tip (red line). Green lines indicate the cuts before inverse Fourier transform for separate analysis. (d) DC component for BBO (black line) and tip (red line). (e) Contribution around ν for BBO (black line) and tip (red line). (f) Contribution at 2ν for BBO (black line) and tip (red line).

discussed the other components of the signal at ν and 2ν displayed in Fig. 4.12(e)-(f). They contain information on the coherence lifetime between all involved states, which may be extracted by modelling via an optical Bloch equation approach. With a continuously scanning interferometer instead of a stepping motor - and therefore a considerably improved signal to noise ratio - we will in the future be able to study the components at ν and in particular 2ν in more detail to get a deeper insight into the lifetime of coherence in the system, which is expected to be even shorter than the population lifetime.

4.2.3 W(310) nanotip as ultrafast nonlinear element

It is noteworthy that the spatiotemporal characterization of light pulses on femtosecond-nanometer scales is still very challenging. Direct extension of far-field techniques as SEA TADPOLE employing fibers [157] and NSOM tips [158] is challenging due to the requirement of interferometric stability and allows only characterization of pulses focused with limited numerical aperture. Nanoobjects and nanocrystals hold promise of another route to 'beat' the diffraction limit [159,160,161,162], but the performance has not been demonstrated for pulses shorter than $\approx 10\,\mathrm{fs}$.

Following our results, photoemission from tungsten nanotips can be applied as an exceptionally broadband nonlinear element on the nanoscale. Regarding the temporal resolution, simulations yield that the excited near-field is essentially a copy of the exciting pulse and we experimentally determined that the lifetime of states involved in photoemission can be shorter than 1 fs. Gold tips have led to an apparent pulse broadening in a similar photoemission experiment [163] and in second harmonic generation [106]. The authors attribute this to plasmonic effects on the near-field, not expected or observed in simulations for tungsten. Also the lifetime of excited intermediate states may play a role for gold. To absolutely rule out any undesired effects of the excited near-field at tungsten, experiments can be repeated with a BBO in the vacuum chamber at the exact same position as the tip. Due to the nanoscale dimensions of the tip, we expect that further studies will allow spatially resolved autocorrelation measurements even in tight laser foci, while the influence of the tip shank still has to be investigated. The response for other central wavelengths is currently unknown and should be examined, too. The incorporation of PRISM, a novel pulse characterization technique relying on a pulse shaper and a spectrally integrated nonlinear measurement [164], may enable full pulse characterization in amplitude and phase. Perhaps one of the most obvious applications of such pulse characterization with nanotips would be in photoemission experiments aiming to determine the lifetime of resonances such as image potential states [155, 165], where an in-situ measurement of pulse durations in the vacuum chamber is required and a photoelectron detector is readily available.

Chapter 5

A few-cycle CEP-stable source at 2μm and its applications

5.1 The light source

In this section we describe a laser source tailored for studies of strong-field phenomena. The source delivers carrier-envelope phase-stable sub-two-cycle pulses at a wavelength of about 2 μm at 100 kHz repetition rate. This constitutes, to the best of our knowledge, the shortest pulses achieved in this wavelength range at repetition rates higher than 1 kHz. A description of the first version of the setup has been published [166] in collaboration with the group of Eberhard Riedle at Ludwig-Maxilimilians-Universität München.

5.1.1 The wavelength regime and the concept of the light source

Laser sources at 2 μm have a broad range of practical applications, ranging from medical surgery to LIDAR [167]. A part of the attraction stems from the fact that these sources are 'eye-safe', i.e. that radiation in the range $1.4 - 2.6\,\mu$m will in the worst case be absorbed in cornea and lens and not reach the much more sensitive retina. At nanotips sources of longer wavelength are promising since they allow a route to enter the tunneling regime of electron emission without increasing the incident intensity ($\gamma \propto 1/\lambda\sqrt{I}$) [62] and moreover give access to dynamics of the electron in the inhomogeneous near-field at the tip due to a larger excursion length of the electron's quiver motion [16]. Another motivation for short infrared pulses comes from high harmonic generation. The cutoff of high harmonic photons is given by $\Phi + 3.17U_p$, where $U_p \propto I\lambda^2$ and so pulses at 2 μm have successfully been used to generate bright, coherent light in the soft x-ray water window [30] and thus paved the way to realize the proposed microholography of living samples [168].

Currently nonlinear frequency conversion is the only way to generate CEP-stable few-cycle pulses at 2 μm and their generation is still challenging. The concept revolves around passive carrier-envelope-phase stabilization by difference-frequency generation, see [43, 45]

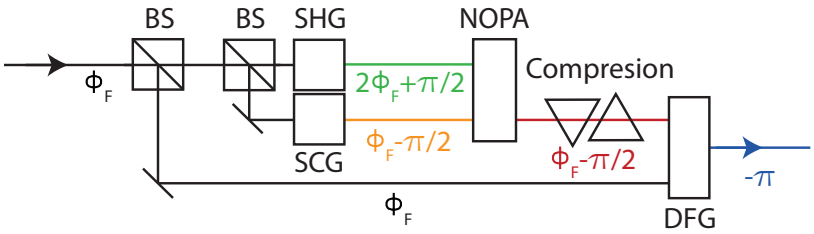

Figure 5.1: Concept of the setup. A laser pulse of carrier-envelope phase (CEP) Φ_F is split up into several copies by beamsplitters (BS). The first part undergoes second harmonic generation (SHG), resulting in a CEP of $2\Phi_F + \pi/2$. The second part is used for supercontinuum generation (SCG) with resulting CEP of $\Phi_F - \pi/2$. This supercontinuum serves as seed for noncollinear optical parametric amplification (NOPA), where it is amplified to yield a stronger pulse than the original seed with the same CEP. After temporal compression in a prism compressor this pulse is used for difference-frequency generation (DFG) with the third part of the fundamental. The result is a pulse of constant CEP regardless of the value of Φ_F.

and Section 2.1.4. A sketch of our setup is shown in Figure 5.1. A driving laser of a few hundred femtoseconds is split up into three copies. One is used for supercontinuum generation (SCG) in a YAG crystal. Another copy is frequency doubled (SHG) and serves as pump for noncollinear optical parametric amplification of the supercontinuum. The signal of this OPA is compressed and difference-frequency mixed with the third copy of the fundamental pulse. Since supercontinuum generation and optical parametric amplification retain the CEP fluctuations, the difference frequency between OPA signal and third fundamental pulse copy is CEP stable.

Similar schemes have in recent years been employed to generate short pulses [169, 170, 171, 172, 173, 174, 175] and high-repetition rate pulse trains [176, 177, 178, 179, 180], but the simultaneous demonstration of a few-cycle high repetition rate source has remained elusive. While our experiment has low requirements on pulse energy, it will immensely benefit from a considerably faster data acquisition for the same signal to noise ratio.

We briefly mention other emerging femtosecond technologies at 2 μm: Thulium, holmium, and chromium lasers. For the case of Tm and Ho recently 135 fs pulses were generated directly [181]. Using nonlinear broadening and compression has also allowed generation of sub-100 fs pulses [182, 183], based on Tm and Ho lasers. Very recently 3-cycle pulses have been demonstrated with a Cr^{2+}ZnS crystal [184]. However, the CEP of none of these sources is stabilized.

5.1.2 Detailed implementation

The current implementation of the conceptual setup in Fig. 5.1 is shown in Fig. 5.2. As driving laser we use a D2.fs from Jenoptik GmbH, containing an Ytterbium fiber laser and a thin disc amplifier. It is connected to a water-water chiller[1]. Due to high-voltage

[1] Termotek AG, P306-18775

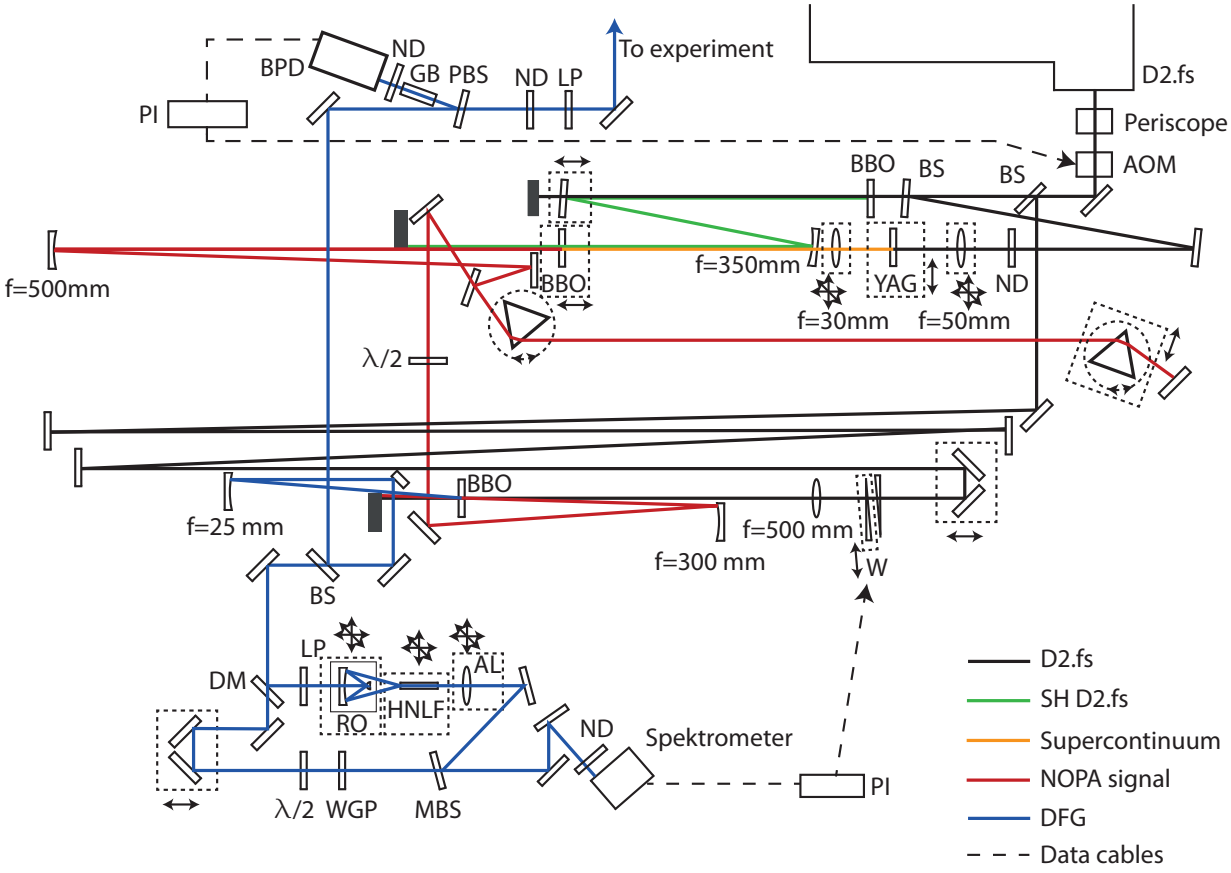

Figure 5.2: Detailed setup: CEP-stable few-cycle laser pulses at around 2000 nm are generated in a two-stage process by first generating a short visible pulse by noncollinear optical parametric amplification and subsequent difference-frequency generation. The lower part of the figure shows the f-2f interferometer. Degrees of freedom are indicated by dashed boxes and arrows. Abbreviations: AOM: Acousto-Optical Modulator, BS: Beam Splitters, BBO: Beta-Barium Borate, ND: Neutral Density Filter, YAG: Yttrium Aluminum Garnet, $\lambda/2$: Half wave plate, W: BK 7 wedges, PI: Digital PI loop, PBS: Polarizing Beam Spliter, GB: Glass Block, BPD: Balanced Photo Diode LP: Low-pass filter, DM: Dichroic Mirror, RO: Reflecting Objective, HNLF: Highly NonLinear Fiber, AL: Aspheric lens, WGP: Wire Grid Polarizer, MBS: Metallic Beam Splitter.

switching for pulse picking for amplification it emits radiofrequency pulses that we shield by a factor of about 10 with a Faraday cage made out of a copper mesh surrounding the laser. Thereby it does not disturb electron couting in the vacuum chamber, where we typically observe signal levels on the 10 mV-range. It delivers pulses centered at 1030 nm with pulse durations of 280 fs and 40 μJ pulse energy at 100 kHz repetition rate. The mirrors in the following setup are narrowband dielectric mirrors for the high-intensity beams[2] and silver mirrors for beams with large spectral bandwidth[3].

[2]Laser Components
[3]Thorlabs, Newport

The NOPA is set up in a double-Z configuration, so that the pump and seed arm both experience the same number of reflections in the same geometry before the OPA nonlinear crystal. This passively cancels pointing instabilities of the driving laser in the NOPA, since they translate identically to pump and seed, minimizing the detrimental effect on amplification. We use around 600 nJ for white-light generation in a 4 mm thick YAG crystal[4]. Focusing and recollimation lenses are mounted on 3D translational stages[5] for optimization of focusing conditions. In particular we optimize the position of the first lens in beam propagation direction as to obtain the lowest power threshold for supercontinuum generation. Consecutively we adjust the pulse energy with the neutral density filter wheel in the beampath to about 10% above the supercontinuum generation threshold, where we have found minimal pulse-to-pulse fluctuations of the energy in the white-light continuum. We choose YAG over the commonly employed sapphire due to a higher n_2 [42], simplifying supercontinuum generation with our rather long driving laser pulses. The YAG crystal is mounted on a manual translation stage to shift the crystal in case of local damage without the need to realign the setup. We find that for a clean laser lab the YAG crystal typically requires no shifting on a time-scale of several weeks of operation. 32 μJ of the D2.fs are frequency doubled in a 0.8 mm thick BBO cut at 23.5° for type I phasematching with an efficiency of about 50% to serve as pump. Due to the small beam size of the driving laser ($1/e^2$ radius of 880 μm) no focusing is required. Seed and pump are focused into a 3 mm thick BBO cut at 20° with an external noncollinearity angle of 3.3°. The amplified pulse is centered around 700 nm, supports pulse durations around 10 fs, and has slight spectral tunability. The signal pulse energy is typically 2−4 μJ. Following collimation with a spherical mirror, the NOPA pulses are compressed to below 20 fs with a pair of fused silica prisms. They are equipped with the standard rotational and translational degrees of freedom[6] for a prism compressor and mounted on magnetic platforms[7] for quick positioning. While the prism compressor increases the size of the setup and thus likely reduces the interferometric stability, it offers flexibility for wavelength tuning and in particular also dispersion management for the DFG. Insertion of neutral density wheels or the entrance window of a vacuum chamber can in this way be precompensated in the visible domain.

For DFG around 2 μJ of the fundamental beam are split off at the beginning of the setup to avoid using the fundamental pulse that has undergone high-efficiency second harmonic generation, which will lead to spatio-temporal pulse distortions. It traverses a pair of motorized[8] BK 7 wedges, which can be used to eliminate small drifts of the CEP of the DFG. This pulse and the NOPA output are focused into a 0.8 mm thick BBO cut at 23.5° for type-I DFG, after the NOPA has passed a half-wave plate[9]. Beam radii are approximately 120 μm for the fundamental beam and 70 μm for the NOPA. To avoid the necessity of dichroic optics, the beams are combined under a small angle below

[4] Altechna
[5] Newport, M-DS-25
[6] Newport, M-UMR5.16 and M-RS40
[7] Edmund Optics, PN 55-527
[8] New Focus, 9066M driven by Newport, Picomotor Actuator
[9] Union Optics

the divergence of the IR pulse. Temporal overlap is ensured with a delay stage in the fundamental beam. Optimized for pulse duration we obtain sub-two-cycle pulses centered between 1.6 and 2.0 μm. By suitable combination of the polarizations the DFG polarization is chosen to be parallel to the optical table.

To verify CEP stability and enable a slow-loop PI-control on the CEP we implemented a home-built f-2f interferometer. For an introduction to CEP measurements we refer the reader to [43]. Conveniently, the BBO used for DFG is simultaneously phase matched for second harmonic generation of the DFG beam and generates sufficient second harmonic for use in an f-2f interferometer. We separate the DFG from its second harmonic with a dichroic mirror (DM). The f-arm passes a long-pass filter[10] to remove residual second harmonic before being focused into a highly nonlinear fiber[11] with a Cassegrain reflecting objective[12] for spectral broadening. Collimation is facilitated with an aspheric lens, minimizing beam distortions. Reflecting objective, highly nonlinear fiber, and aspheric lens all require 3D translational stages. With a flip mirror (not shown in Fig. 5.2) we can image the output of the highly nonlinear fiber to a CCD camera[13] to facilitate coupling of the invisible beam into the fiber. The long-pass filter in front of the objective can be removed to let stray light pass into the fiber for initial alignment. The 2f-arm passes a manual delay stage, a $\lambda/2$-plate, and a wire grid polarizer[14] for rotation and cleanup of polarization. Upon beam recombination with a 50:50 metallic beam splitter (MBS) the beams are collinearly sent to a spectrometer[15].

Since we observe output power fluctuations and drifts of the D2.fs on the per cent level we tackle them with an acousto-optical modulator (AOM)[16]. Uncompensated they amplify due to the sequence of nonlinearities in our laser system. We use the 0th order beam and deflect power fluctuations into the 1st order, which is dumped. Feedback to the AOM is provided by splitting off a small part of the DFG with a pellicle beam splitter (PBS) onto a home-built extended InGaAs balanced photodiode (BPD) after passing a 48 mm long block of fused silica to reduce the peak intensity of the beam, since the response of the photodiode to the laser power will otherwise be nonlinear. A digital PI-loop programmed in LabView gives feedback to the AOM to stabilize the output power.

Compared to the original setup [166] we have therefore meanwhile improved the source by the following measures:

- Implementation of an acousto-optical modulator (AOM) with PI loop feedback on the sound wave intensity. It serves to stabilize the output power of the DFG measured by a balanced photodiode or a thermal powermeter by modulating the power of the D2.fs, which by itself sporadically shows power fluctuations and drifts exceeding 1 %,

[10] Schott, RG 1000
[11] OFS, HNLF
[12] Ealing, x36 25-0522
[13] Monacor, TVCCD240
[14] Moxtek, UBB01A
[15] Ocean Optics USB 4000
[16] EQ Photonics I-M080-3C10G-4-AM3 driven by A35080-S-1/50-P4K7U

with a digital LabView PI loop. The 0th order beam of the AOM is sent into the setup, while the 1st diffraction order is dumped.

- Changed the geometrical setup of the NOPA to a balanced double-Z configuration for second harmonic and supercontinuum ensuring passive cancellation of pointing instabilities of the driving laser in the NOPA process.
- Splitting off the fundamental beam for DFG before SHG to avoid pulse distortions.
- Use of highly stable optomechanics[17] and lowering of beam height over the optical table to 95 mm.

These changes enhance the stability of the system, while the operating parameters remain unchanged.

5.1.3 System performance

In Figure 5.3 we present spectra and autocorrelation measurements of the DFG. Evidently, wavelength-tuning of the NOPA allows a slight tunability of the system between central wavelengths of about 1.6 μm to 2.0 μm. Under optimized conditions the pulse duration remains sub-two cycle over the whole tuning range. Intensity autocorrelations are measured with a second-harmonic all-reflective split-mirror autocorrelator with a 10 μm BBO crystal cut at 23° allowing few-cycle pulse characterization[18].

[17]Mirror mounts Radiant Dyes, MDI-HS series and solid 1 inch stainless steel posts for mounting
[18]identical to Horiba Jobin Yvon, NOPA-PAL

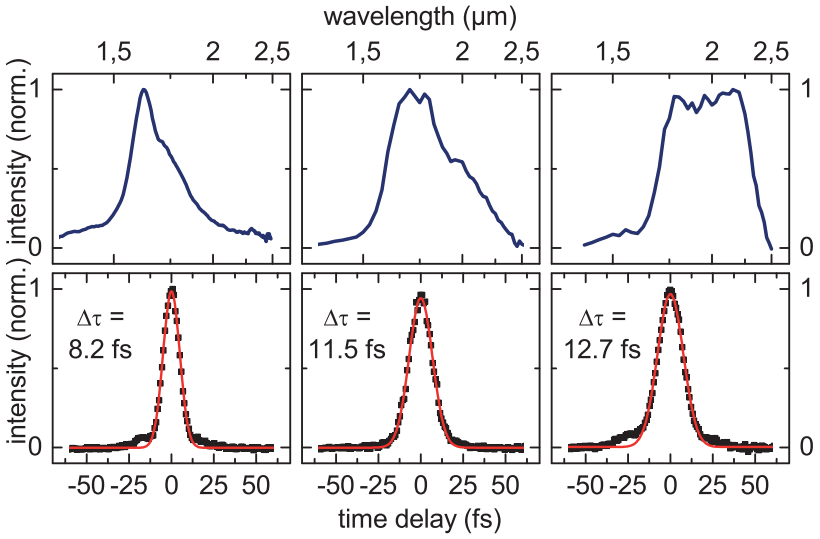

Figure 5.3: Laser spectra and corresponding intensity autocorrelation traces showing a sub-two-cycle pulse duration over the whole spectral tunability. $\Delta\tau$ denotes the deconvolved pulse duration assuming a Gaussian pulse shape. Taken from [166].

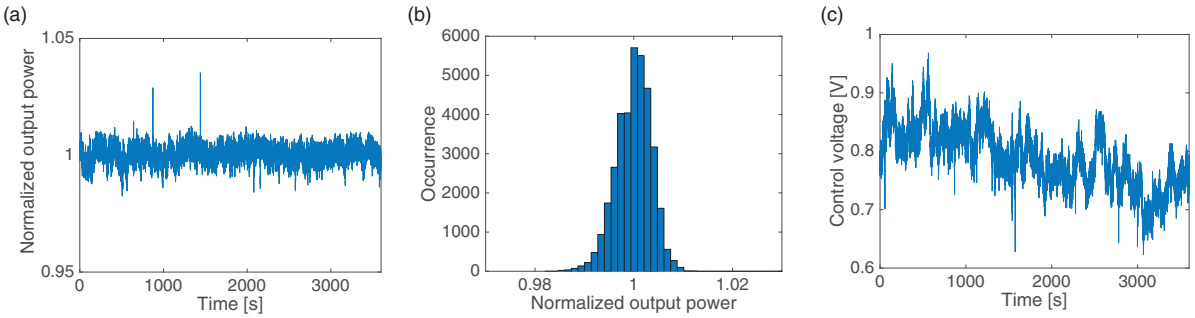

Figure 5.4: Long-term stability of the laser source with feedback to the AOM. (a) Output power as measured by an out-of-loop thermal powerhead. (b) Histogram of the data in (a). (c) Corresponding feedback signal to the AOM. The feedback range is $0 - 1.1\,\mathrm{V}$ and we typically choose an operating point around $0.8\,\mathrm{V}$ for linearity of the deflecting power with a change in control voltage.

The DFG pulse energy is on the order of 100 nJ. To some degree the alignment involves a tradeoff between shortest pulse duration and high output energy. For example, for the shortest pulse durations output energies of typically 40 nJ are achieved, while up to 150 nJ are obtained when 3-cycle pulses are acceptable. Output power stability over one hour involving a PI-feedback loop with an InGaAs photodiode for in-loop feedback is displayed in Fig. 5.4. In this example we determine a standard deviation of the output power of $\sigma = 0.36\,\%$ with an out-of-loop thermal powerhead. When the power requirements of the experiment are low, a slightly better performance can be obtained with a thermal in-loop detector, as detection with the photodiode tends to overestimate the fluctuations. Without

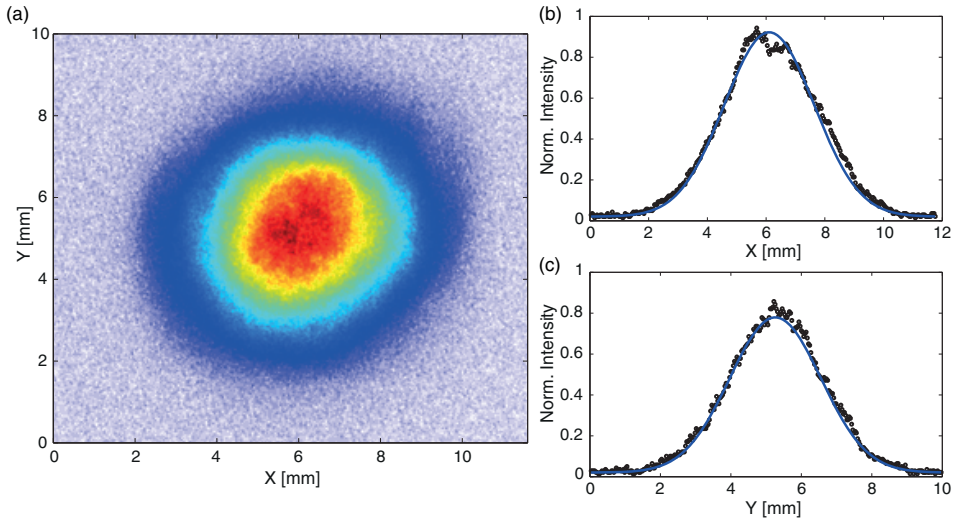

Figure 5.5: (a) Beam profile of the DFG as seen on an IR card. (b) and (c) Cross sections with Gaussian fits in x and y direction. Taking into account the nonlinearity of the detector card we evaluate $1/e^2$ intensity radii of the beam of $w_X = 6.8\,\mathrm{mm}$ and $w_Y = 6.1\,\mathrm{mm}$.

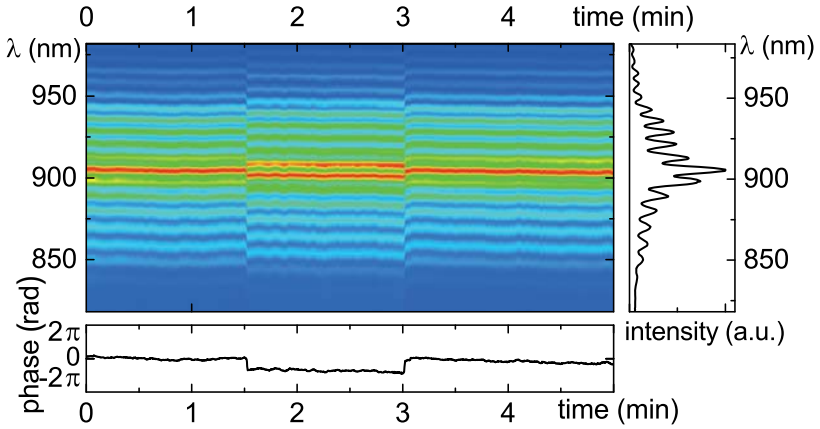

Figure 5.6: f-2f interferogram and evaluated phase over 5 min. At 1.5 min and 3.0 min the CEP is shifted by π by moving the wedges W by approximately 6 μm. Spectrometer acquisition time is 0.5 s and we observe 79 mrad rms phase fluctuations. The high fringe visibility is proof of low shot-to-shot CEP fluctuations. Modified from [166].

the feedback loop, power fluctuations and drifts increase by up to an order of magnitude.

To judge the beam profile we direct a silicon CCD[19] onto an infrared detector card[20] that the DFG beam is impinging onto. We observe a homogeneous, almost spherical beam profile of the output illustrated in Fig. 5.5. Gaussian fits in panels (b) and (c) fit the data well. We also verified that the beam can be focused tightly, close to the diffraction limit, to a spot size of about 4 μm by an off-axis parabolic mirror.

In the f-2f interferometer we observe a strongly modulated interferogram between the f and 2f arm with stable fringes over several minutes even without active feedback, see Fig. 5.6. This proves the passive CEP stability of the setup expected from the theory of parametric interactions, as discussed in Section 2.1. With a Fourier algorithm we extract the respective CEP values from the recorded spectra and find 79 mrad phase fluctuations for an integration time of 0.5 s. While we have no direct shot-to-shot resolution, the high fringe visibility evidences that the shot-to-shot CEP fluctuations are low.

5.2 First applications of the source

5.2.1 Transition between multiphoton and tunneling regime

As a first application of our source we investigated the transition regime between multiphoton photoemission and tunneling photoemission from a W(310) tip. We record the electron current as a function of laser intensity in the vicinity of $\gamma = 1$, see Fig. 5.7(a). We observe a kink in the photoemitted current close to the predicted value of $\gamma = 1$, evaluated with the expected field enhancement at the tip. In Keldysh theory this kink sig-

[19] Imaging source, DMK21BU04
[20] Thorlabs, VCR 4

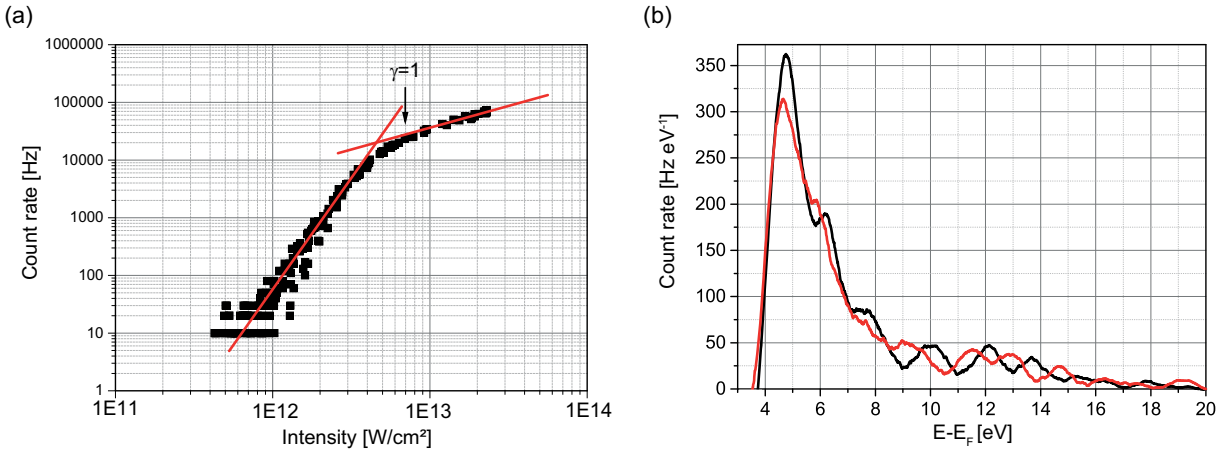

Figure 5.7: Photoemission from W(310) nanotips in the transition region from multiphoton to tunneling regime. (a) Detected electron count rate as function of estimated near-field intensity. Pulse duration $\tau = 22\,\text{fs}$ and central wavelength $\lambda_c = 1720\,\text{nm}$. The estimated transition point $\gamma = 1$ is marked. (b) Carrier-envelope-phase(CEP)-resolved electron spectra of a different W(310) tip for two CEPs differing by π, laser pulse duration of 17 fs, central wavelength of 1850 nm, and a Keldysh parameter of $\gamma \approx 0.5$. A structure with spacing of approximately 2.5 eV appears, much larger than the photon energy of 0.7 eV, which is sensitive to the CEP.

nifies the transition from multiphoton to tunneling regime when strong-field effects start to suppress the lower photon orders, which in sum counterintuitively leads to a flattening of the observed nonlinearity [13, 17] and our data agrees well with this notion. However, for our parameters the predicted transition from multiphoton to tunneling regime and the emission of more than one electron per laser pulse coincide, similar to [13]. This may lead to a subsequent suppression of electron emission due to the formation of space charge. We have therefore investigated the influence of different anodes collecting the photoemitted current. In practice we measured the current either directly with the MCP or with the electron spectrometer, so that the anode was in one case a few millimeters and the other case a few centimeters away from the tip. Also we investigated the influence of different bias voltages between tip and these anodes. For our range of parameters the kink position was independent of the static field and of the chosen anode. This clearly favors the explanation that the kink is caused by the transition between photoemission regimes. Further systematic studies including spectral resolution will unambiguously assign the effect to one or the other process and may additionally give insight into the role of excited states.

Moreover, we have investigated the influence of the carrier-envelope phase on the photoelectron spectrum at an estimated Keldysh parameter of $\gamma \approx 0.5$, see Fig. 5.7(b). Interestingly, we find a structure in the photoelectron spectra with a spacing of about 2.5 eV, much larger than the photon energy of 0.7 eV. This structure is dependent on the carrier-envelope phase of the laser pulse, which strongly suggests an interference mechanism for the occurrence of the structure. We note that it is also observed in a recent, very similar

study at gold tips [17], but its origin is not discussed there. As they are not critically dependent on the material, the features probably represent sub-cycle dynamics of photoemission, for example the interference of short and long trajectories in rescattering [185]. The corresponding temporal separation, simply evaluated by $\Delta t = h/E$, is on the order of 1.7 fs. Another possibility is interference involving electrons that enter the tip while driven by the laser field. Recently a study has been conducted at tungsten tips with 800 nm pulses [186], which reports an additional delayed emission channel involving such electrons, albeit without coherent effects.

5.2.2 Value for further studies

In addition to photoemission studies at metal nanotips the operating parameters make our laser system a highly attractive source for a plethora of immediate applications. With tight focusing peak intensities in the $10^{13}\,\mathrm{W/cm^2}$ range are attainable even without field enhancement, corresponding to field strengths on the V/Å level, so that studies of high harmonic generation at bulk materials with controlled electric field shape are within reach [187, 188] and we have already conducted preliminary studies on harmonic generation at metal nanotips [189]. Additional amplification of the output of our source will result in high-contrast pulses for high-harmonic generation in gases. Two-color studies around $\gamma = 1$ with a perturbative second harmonic will elucidate the transition between multiphoton and tunneling regime further. Our source is also of interest for dielectric laser acceleration [100, 190], where electrons are accelerated in the near fields of dielectric nanostructures. When the laser wavelength is shifted from 800 nm to 2 μm, silicon structures can be employed and decades of experience in nanofabrication can be harnessed.

Chapter 6

Conclusion and Outlook

In this thesis we discussed three advances in understanding and controlling light-matter interaction, studied by photoemission from metallic nanotips. First, we used the fraction of the electrons that undergoes rescattering after photoemission as a probe of the laser-excited near field at the tip's apex on a scale of 1 nm. Second, we devised and implemented a two-color scheme for coherent control of multiphoton photoemission, achieving a phase-dependent contrast of photoemission of up to 94 %. We have demonstrated that despite the complexity of a solid state system – that one may also expect to manifest itself in photoemission experiments – our results can be interpreted in terms of just two almost perfectly interfering quantum pathways. Third, we set up a light source yielding, to our knowledge, the shortest carrier-envelope phase-stable pulses around 2 μm at such high repetition rate. In a first application we investigated the transition from the multiphoton to the tunneling regime of photoemission.

To measure the strength of the near field at nanotips we used near-infrared laser pulses from a Titanium:Sapphire oscillator. They are focused tightly onto the nanotip to excite the near field, which in turn leads to photoemission. Electrons that undergo rescattering at the metal surface driven by the near field achieve the highest kinetic energies and their energy can be related to the strength of the near field during photoemission. In a systematic study we varied tip material and tip radius of curvature. We find field enhancement factors from 2.5 to 6 for radii of curvature from 51 to 9 nm for both gold and tungsten tips. Our experimental data agrees well with simulations of linear Maxwell's equations and indicates that field enhancement is in our case predominantly a geometrical effect.

To coherently control photoemission we relied on a two-color approach using the fundamental ω and second harmonic 2ω laser pulses of an amplified Erbium-doped fiber laser. Depending on the relative phase of the overlapping light pulses, electron emission is considerably enhanced compared to temporally separated pulses or suppressed to almost 0. Electron spectra reveal that all multiphoton orders are synchronously and similarly affected. This observation in addition to the scaling of the cooperative signals with laser pulse intensities strongly suggests a model of interfering quantum pathways: Two simultaneously present emission pathways involving different numbers of photons of the two colors

interfere with each other, which for similar total transition amplitudes leads to almost perfect constructive or destructive interference. Thereby, modulating the relative phase of two light waves, we were able to switch electron emission confined to the femtosecond time scale.

While most studies of photoemission from nanotips have been performed with readily available Titanium:Sapphire lasers, light sources of longer wavelength offer studying the tunneling regime with ease. Due to the lack of laser sources directly yielding carrier-envelope phase-stable few-cycle pulses in the range of 2 μm we set up a light source based on nonlinear frequency conversion. We first generate a short intense visible pulse by non-collinear optical parametric amplification and then perform difference-frequency generation with the driving laser to the infrared. This scheme ensures passive carrier-envelope-phase stabilization and requires only correction for slow thermal drifts. We used this light source to investigate photoemission from the multiphoton to the tunneling regime and found good agreement with Keldysh theory. In addition we performed initial spectrally-resolved measurements in the tunneling regime and find an interference structure sensitive to the carrier-envelope phase indicative of sub-cycle features in electron emission.

Outlook

We would like to devote the last section of this thesis to the future of the discussed line of experiments. Further investigations of fundamental character will enhance our understanding of light-matter interaction at the solid state and first applications promise to stock up our toolbox for time-resolved investigations of matter and the characterization of light waves on the nanoscale.

High harmonic generation at metal tips

The observed process of elastically rescattering electrons is at the heart of attosecond science. At atoms, it is known to be complemented by inelastic processes upon reencountering the parent matter, specifically by coherent recombination, leading to high harmonic generation (HHG). In a quantum mechanical picture of HHG, a part of the electron wavefunction is split off and returns to the parent matter driven by the external electric field; the interference of the returning and the stationary part of the wavefunction leads to the generation of high-energy photons [8]. While in the case of atoms the coherence between the two components of the wavefunction is ensured, the solid state displays efficient decoherence mechanisms and the observation of high harmonic generation at metal tips complemented by electron spectra would give fundamental insight into the associated timescales. For this purpose we have set up a suitable experiment and are currently searching for high-energy photons [189].

Optimization and enhanced characterization of near fields

Recent simulations [124] have revealed that a larger tip opening angle than typically obtained with our electrochemical etching methods should lead to a stronger near field at the tip apex. Many applications could profit from this finding and currently work is underway to confirm this result experimentally. Moreover, the rescattering method for measuring near fields can conceptually be extended to a tomographic reconstruction of the near field at the tip apex by employing laser pulses of adjustable wavelength and intensity. An electron spectrometer with angular resolution [191] will allow to determine the field over the whole apex. Ultimately we believe that attosecond streaking will yield information of the near fields at both shank and apex of the nanotip and fields at other nanoscale systems with amplitude and phase resolution.

Avenues for coherent control at nanotips

Following our pioneering investigations, probing of various materials in specific crystallographic orientations will give insight into how the mechanism, for example the number of involved pathways and the relative amplitude of each pathway, depends on the system under investigation. We have observed (but not discussed in this thesis) that the static bias field modifies the interference behavior. Understanding its influence may give insight into the formation of an emission barrier by the optical and static fields. Referencing the relative phase measurements will give access to the quantum mechanical contribution in the phase between the two pathways. Further coherent control schemes complementing the Brumer-Shapiro-like scheme that we have explored, like the application of a pulse shaper with an adaptive algorithm [134] may elucidate the quantum dynamics further. At higher field strengths, as available from the NOPA-DFG laser system, two-color measurements will be performed in the tunneling regime, where emitted electrons may be steered in the synthesized light wave [148]. Finally, we have indication that exploring the polarization of the two colors as an additional degree of freedom at isolated tips and tip arrays, which are discussed as electron sources in a scheme for coherent x-ray generation [22, 23, 192], will allow complex spatiotemporal shaping of electron emission on the fs-nm scale.

Time-resolved imaging of matter

Lastly, we give two examples of how our understanding of electron emission from tips may be applied. One opportunity is time-resolved imaging of matter using electron pulses as probe of dynamic structural changes. For application of nanotips as laser-triggered electron source, the mechanism and thereby the time scale of electron emission is critical for the temporal resolution. In our measurements we find that a high-repetition rate, low-power laser can confine electron emission to the (sub-)femtosecond scale, while higher pulse energies have been reported to lead to thermal emission [51, 79]. We have therefore set up a tip-based source of electrons at 30 keV for electron diffraction [21] driven by a laser oscillator. Since it has been established that photoemitted electrons can display the same exceptional transverse coherence as DC emission [18], also large samples such as single

biological molecules [193] can be subject to time-resolved studies with the help of electron pulses from metal tips.

Nanoscale sensing of light fields

In this work we measured the strength of the near field at the nanotip apex and discussed an experiment to obtain phase information on this field. On a different level, given the nanometric dimensions of the tip, we can also employ it to measure local properties of the electric field with sub-wavelength resolution. For example, the tip can map out intensity distributions of a laser focus by determining the electron current as a function of position for a known nonlinearity of electron emission. Moreover, we demonstrated that the lifetime of intermediate states involved in photoemission from a (310) tungsten tip can be so short that nanotips should allow spatially-resolved characterization of pulse durations. In addition, relative phase information, such as the classical Gouy phase shift is within reach due to the phase sensitivity of the rescattering plateau [15, 194], and our ω-2ω-scheme allows measuring the relative Gouy phase between two colors [195] with unprecedented spatial resolution.

Bibliography

[1] Müller, E. W. & Bahadur, K. Field Ionization of Gases at a Metal Surface and the Resolution of the Field Ion Microscope. *Phys. Rev.* **102**, 624–631 (1956).

[2] Müller, E. W. Das Feldionenmikroskop. *Z. Phys.* **131**, 136 (1951).

[3] Müller, E. W., Panitz, J. A. & McLane, S. B. The Atom Probe Field Ion Microscope. *Rev. Sci. Instrum.* **39**, 83–86 (1968).

[4] Binnig, G., Rohrer, H., Gerber, C. & Weibel, E. Tunneling through a controllable vacuum gap. *Appl. Phys. Lett.* **40**, 178–180 (1982).

[5] Binnig, G., Quate, C. F. & Gerber, C. Atomic Force Microscope. *Phys. Rev. Lett.* **56**, 930–933 (1986).

[6] Pohl, D. W., Denk, W. & Lanz, M. Optical stethoscopy: Image recording with resolution $\lambda/20$. *Appl. Phys. Lett.* **44**, 651–653 (1984).

[7] Spence, J. C. H. *High-Resolution Electron Microscopy* (Oxford University Press, New York, 2013).

[8] Krausz, F. & Ivanov, M. Attosecond physics. *Rev. Mod. Phys.* **81**, 163–234 (2009).

[9] Apolonski, A., Dombi, P., Paulus, G. G., Kakehata, M., Holzwarth, R., Udem, T., Lemell, C., Torizuka, K., Burgdörfer, J., Hänsch, T. W. & Krausz, F. Observation of Light-Phase-Sensitive Photoemission from a Metal. *Phys. Rev. Lett.* **92**, 073902 (2004).

[10] Hommelhoff, P., Sortais, Y., Aghajani-Talesh, A. & Kasevich, M. A. Field Emission Tip as a Nanometer Source of Free Electron Femtosecond Pulses. *Phys. Rev. Lett.* **96**, 077401 (2006).

[11] Hommelhoff, P., Kealhofer, C. & Kasevich, M. A. Ultrafast Electron Pulses from a Tungsten Tip Triggered by Low-Power Femtosecond Laser Pulses. *Phys. Rev. Lett.* **97**, 247402 (2006).

[12] Ropers, C., Solli, D. R., Schulz, C. P., Lienau, C. & Elsaesser, T. Localized Multiphoton Emission of Femtosecond Electron Pulses from Metal Nanotips. *Phys. Rev. Lett.* **98**, 043907 (2007).

[13] Bormann, R., Gulde, M., Weismann, A., Yalunin, S. V. & Ropers, C. Tip-Enhanced Strong-Field Photoemission. *Phys. Rev. Lett.* **105**, 147601 (2010).

[14] Schenk, M., Krüger, M. & Hommelhoff, P. Strong-Field Above-Threshold Photoemission from Sharp Metal Tips. *Phys. Rev. Lett.* **105**, 257601 (2010).

[15] Krüger, M., Schenk, M. & Hommelhoff, P. Attosecond control of electrons emitted from a nanoscale metal tip. *Nature* **475**, 78–81 (2011).

[16] Herink, G., Solli, D. R., Gulde, M. & Ropers, C. Field-driven photoemission from nanostructures quenches the quiver motion. *Nature* **483**, 190–193 (2012).

[17] Piglosiewicz, B., Schmidt, S., Park, D. J., Vogelsang, J., Groß, P., Manzoni, C., Farinello, P., Cerullo, G. & Lienau, C. Carrier-envelope phase effects on the strong-field photoemission of electrons from metallic nanostructures. *Nat. Photon.* **8**, 37–42 (2014).

[18] Ehberger, D., Hammer, J., Eisele, M., Krüger, M., Noe, J., Högele, A. & Hommelhoff, P. Highly Coherent Electron Beam from a Laser-Triggered Tungsten Needle Tip. *Phys. Rev. Lett.* **114**, 227601 (2015).

[19] Müller, M., Paarmann, A. & Ernstorfer, R. Femtosecond electrons probing currents and atomic structure in nanomaterials. *Nat. Commun.* **5**, 5292 (2014).

[20] Paarmann, A., Gulde, M., Müller, M., Schäfer, S., Schweda, S., Maiti, M., Xu, C., Hohage, T., Schenk, F., Ropers, C. & Ernstorfer, R. Coherent femtosecond low-energy single-electron pulses for time-resolved diffraction and imaging: A numerical study. *J. Appl. Phys.* **112**, 113109 (2012).

[21] Hoffrogge, J., Stein, J. P., Krüger, M., Förster, M., Hammer, J., Ehberger, D., Baum, P. & Hommelhoff, P. Tip-based source of femtosecond electron pulses at 30 keV. *J. Appl. Phys.* **115**, 094506 (2014).

[22] Swanwick, M. E., Keathley, P. D., Fallahi, A., Krogen, P. R., Laurent, G., Moses, J., Kärtner, F. X. & Velásquez-García, L. F. Nanostructured Ultrafast Silicon-Tip Optical Field-Emitter Arrays. *Nano Lett.* **14**, 5035–5043 (2014).

[23] Graves, W. S., Kärtner, F. X., Moncton, D. E. & Piot, P. Intense Superradiant X Rays from a Compact Source Using a Nanocathode Array and Emittance Exchange. *Phys. Rev. Lett.* **108**, 263904 (2012).

[24] Hartschuh, A. Tip-Enhanced Near-Field Optical Microscopy. *Angew. Chem. Int. Ed.* **47**, 8178–8191 (2008).

[25] Zuloaga, J., Prodan, E. & Nordlander, P. Quantum Plasmonics: Optical Properties and Tunability of Metallic Nanorods. *ACS Nano* **4**, 5269–5276 (2010).

[26] Maiman, T. H. Stimulated Optical Radiation in Ruby. *Nature* **187**, 493–494 (1960).

[27] Brumer, P. & Shapiro, M. Control of unimolecular reactions using coherent light. *Chem. Phys. Lett.* **126**, 541–546 (1986).

[28] Shapiro, M. & Brumer, P. Laser control of product quantum state populations in unimolecular reactions. *J. Chem. Phys.* **84**, 4103 (1986).

[29] Shapiro, M., Hepburn, J. W. & Brumer, P. Simplified laser control of unimolecular reactions: Simultaneous (ω_1, ω_3) excitation. *Chem. Phys. Lett.* **149**, 451–454 (1988).

[30] Chen, M.-C., Arpin, P., Popmintchev, T., Gerrity, M., Zhang, B., Seaberg, M., Popmintchev, D., Murnane, M. M. & Kapteyn, H. C. Bright, Coherent, Ultrafast Soft X-Ray Harmonics Spanning the Water Window from a Tabletop Light Source. *Phys. Rev. Lett.* **105**, 173901 (2010).

[31] Lewis, G. N., Lipkin, D. & Magel, T. T. Reversible Photochemical Processes in Rigid Media. A Study of the Phosphorescent State. *J. Am. Chem. Soc.* **63**, 3005–3018 (1941).

[32] Boyd, R. W. *Nonlinear Optics* (3rd edition, Academic Press, Burlington, 2008).

[33] Mukamel, S. *Principles of Nonlinear Optical Spectroscopy* (Oxford University Press, Oxford, 1999).

[34] Franken, P. A., Hill, A. E., Peters, C. W. & Weinreich, G. Generation of Optical Harmonics. *Phys. Rev. Lett.* **7**, 118–119 (1961).

[35] Hum, D. S. & Fejer, M. M. Quasi-phasematching. *Comptes Rendus Physique* **8**, 180–198 (2007).

[36] Nikogosyan, D. N. Beta barium borate (BBO). *Appl. Phys. A* **52**, 359–368 (1991).

[37] Cerullo, G. & Silvestri, S. D. Ultrafast optical parametric amplifiers. *Rev. Sci. Instrum.* **74**, 1–18 (2003).

[38] Riedle, E., Beutter, M., Lochbrunner, S., Piel, J., Schenkl, S., Spörlein, S. & Zinth, W. Generation of 10 to 50 fs pulses tunable through all of the visible and the NIR. *Appl. Phys. B* **71**, 457–465 (2014).

[39] Homann, C. *Optical parametric processes to the extreme: From new insights in first principles to tunability over more than 4 octaves.* Ph.D. thesis, München (2012).

[40] Alfano, R. R. (ed.) *The Supercontinuum Laser Source* (Springer, New York, 2006).

[41] Brodeur, A. & Chin, S. L. Ultrafast white-light continuum generation and self-focusing in transparent condensed media. *JOSA B* **16**, 637 (1999).

[42] Bradler, M., Baum, P. & Riedle, E. Femtosecond continuum generation in bulk laser host materials with sub-μJ pump pulses. *Appl. Phys. B* **97**, 561–574 (2009).

[43] Cerullo, G., Baltuška, A., Mücke, O. & Vozzi, C. Few-optical-cycle light pulses with passive carrier-envelope phase stabilization. *Laser & Photon. Rev.* **5**, 323–351 (2011).

[44] Baltuska, A., Fuji, T. & Kobayashi, T. Controlling the carrier-envelope phase of ultrashort light pulses with optical parametric amplifiers. *Phys. Rev. Lett.* **88**, 133901 (2002).

[45] Baltuska, A., Fuji, T. & Kobayashi, T. Self-referencing of the carrier-envelope slip in a 6-fs visible parametric amplifier. *Opt. Lett.* **27**, 1241–1243 (2002).

[46] Jones, R. J. & Diels, J. C. Stabilization of femtosecond lasers for optical frequency metrology and direct optical to radio frequency synthesis. *Phys. Rev. Lett.* **86**, 3288–3291 (2001).

[47] Koke, S., Grebing, C., Frei, H., Anderson, A., Assion, A. & Steinmeyer, G. Direct frequency comb synthesis with arbitrary offset and shot-noise-limited phase noise. *Nat. Photon.* **4**, 462–465 (2010).

[48] Botineau, J. & Stolen, R. H. Effect of polarization on spectral broadening in optical fibers. *JOSA* **72**, 1592 (1982).

[49] Bellini, M. & Hänsch, T. W. Phase-locked white-light continuum pulses: toward a universal optical frequency-comb synthesizer. *Opt. Lett.* **25**, 1049 (2000).

[50] Krüger, M. *Attosecond Physics in Strong-Field Photoemission from Metal Nanotips.* Ph.D. thesis, München (2013).

[51] Kealhofer, C., Foreman, S. M., Gerlich, S. & Kasevich, M. A. Ultrafast laser-triggered emission from hafnium carbide tips. *Phys. Rev. B* **86**, 035405 (2012).

[52] Winckler, J. H. *Gedanken von den Eigenschaften, Wirkungen und Ursachen der Electricität: nebst einer Beschreibung zwo neuer Electrischen Maschinen* (Breitkopf, Leipzig, 1744).

[53] Fowler, R. H. & Nordheim, L. Electron Emission in Intense Electric Fields. *Proc. R. Soc. A* **119**, 173–181 (1928).

[54] Schottky, W. Über den Einfluss von Strukturwirkungen, besonders der Thomsonschen Bildkraft, auf die Elektronenemission der Metalle. *Phys. Zeitschr.* **15**, 872–879 (1914).

[55] Murphy, E. L. & Good, R. H. Thermionic Emission, Field Emission, and the Transition Region. *Phys. Rev.* **102**, 1464–1473 (1956).

[56] Schenk, M. *Starkfeldeffekte und Attosekundendynamik in Photoemission von Metallnanospitzen*. Ph.D. thesis, München (2012).

[57] Burgess, R. E., Kroemer, H. & Houston, J. M. Corrected Values of Fowler-Nordheim Field Emission Functions v(y) and s(y). *Phys. Rev.* **90**, 515–515 (1953).

[58] Hertz, H. Ueber einen Einfluss des ultravioletten Lichtes auf die electrische Entladung. *Ann. Phys.* **267**, 983–1000 (1887).

[59] Thomson, J. Cathode Rays. *Philos. Mag. Series 5* **44**, 293–316 (1897).

[60] Einstein, A. Über einen die Erzeugung und Verwandlung des Lichtes betreffenden heuristischen Gesichtspunkt. *Ann. Phys.* **322**, 132–148 (1905).

[61] Eastman, D. E. Photoelectric Work Functions of Transition, Rare-Earth, and Noble Metals. *Phys. Rev. B* **2**, 1–2 (1970).

[62] Keldysh, L. Ionization in the field of a strong electromagnetic wave. *Sov. Phys. JETP* **20**, 1307 (1965).

[63] Bunkin, F. & Fedorov, M. V. Cold emission of electrons from the surface of a metal in a strong radiation field. *Sov. Phys. JETP* **48**, 1341–1346 (1965).

[64] Perelomov, A. M., Popov, V. S. & Terent'ev, M. V. Ionization of atoms in an alternating electric field. *Sov. Phys. JETP* **23**, 924–934 (1966).

[65] Perelomov, A. M. & Popov, V. S. Ionization of atoms in an alternating electrical field III. *Sov. Phys. JETP* **25**, 336–343 (1967).

[66] Perelomov, A. M., Popov, V. S. & Terent'ev, M. V. Ionization of atoms in an alternating electric field II. *Sov. Phys. JETP* **24**, 207 (1967).

[67] Voronov, G. S. & Delone, N. B. Many-photon ionization of the xenon atom by ruby laser radiation. *Sov. Phys. JETP* **50**, 78–84 (1966).

[68] Agostini, P., Barjot, G., Bonnal, J., Mainfray, G., Manus, C. & Morellec, J. Multiphoton ionization of hydrogen and rare gases. *IEEE J. Quant. Electron.* **4**, 667–669 (1968).

[69] Anisimov, S. I., Benderski, V. A. & Farkas, G. Nonlinear photoelectric emission from metals induced by a laser radiation. *Soviet Physics Uspekhi* **20**, 467–488 (1977).

[70] Agostini, P., Fabre, F., Mainfray, G., Petite, G. & Rahman, N. K. Free-Free Transitions Following Six-Photon Ionization of Xenon Atoms. *Phys. Rev. Lett.* **42**, 1127–1130 (1979).

[71] Luan, S., Hippler, R., Schwier, H. & Lutz, H. O. Electron Emission from Polycrystalline Copper Surfaces by Multi-Photon Absorption. *Europhys. Lett.* **9**, 489 (1989).

[72] Tamm, I. Über eine mögliche Art der Elektronenbindung an Kristalloberflächen. *Z. Physik* **76**, 849–850 (1932).

[73] Shockley, W. On the Surface States Associated with a Periodic Potential. *Phys. Rev.* **56**, 317–323 (1939).

[74] Klamroth, T. *Quantendynamik von Atomen und Elektronen an nicht-rigiden Festkörperoberflächen*. Ph.D. thesis, Berlin (2000).

[75] Echenique, P. M. & Pendry, J. B. The existence and detection of Rydberg states at surfaces. *J. Phys. C* **11**, 2065 (1978).

[76] Petek, H. & Ogawa, S. Femtosecond time-resolved two-photon photoemission studies of electron dynamics in metals. *Prog. Surf. Sci.* **56**, 239–310 (1997).

[77] Lee, M. J. G. Field Emission of Hot Electrons from Tungsten. *Phys. Rev. Lett.* **30**, 1193–1196 (1973).

[78] Yanagisawa, H., Hengsberger, M., Leuenberger, D., Klöckner, M., Hafner, C., Greber, T. & Osterwalder, J. Energy Distribution Curves of Ultrafast Laser-Induced Field Emission and Their Implications for Electron Dynamics. *Phys. Rev. Lett.* **107**, 087601 (2011).

[79] Herink, G., Wimmer, L. & Ropers, C. Field emission at terahertz frequencies: AC-tunneling and ultrafast carrier dynamics. *New J. Phys.* **16**, 123005 (2014).

[80] Corkum, P. B. Plasma perspective on strong field multiphoton ionization. *Phys. Rev. Lett.* **71**, 1994–1997 (1993).

[81] Kulander, K. C., Schafer, K. J. & Krause, J. L. Dynamics of Short-Pulse Excitation, Ionization and Harmonic Conversion. In Piraux, B., L'Huillier, A. & Rzazewski, K. (eds.) *Super-Intense Laser-Atom Physics*, NATO ASI Series, 95–110 (Springer US, 1993).

[82] Busuladzić, M., Gazibegović-Busuladžić, A. & Milošević, D. B. High-order above-threshold ionization in a laser field: Influence of the ionization potential on the high-energy cutoff. *Laser Phys.* **16**, 289–293 (2006).

[83] Krüger, M. *Laser-triggered electron emission from tungsten tips*. Master's thesis, München (2009).

[84] Savitzky, A. & Golay, M. J. E. Smoothing and Differentiation of Data by Simplified Least Squares Procedures. *Anal. Chem.* **36**, 1627–1639 (1964).

[85] Klein, M. & Schwitzgebel, G. An improved lamellae drop-off technique for sharp tip preparation in scanning tunneling microscopy. *Rev. Sci. Instrum.* **68**, 3099–3103 (1997).

[86] Müller, E. W. Work Function of Tungsten Single Crystal Planes Measured by the Field Emission Microscope. *J. Appl. Phys.* **26**, 732–737 (1955).

[87] Eisele, M., Krüger, M., Schenk, M., Ziegler, A. & Hommelhoff, P. Note: Production of sharp gold tips with high surface quality. *Rev. Sci. Instr.* **82**, 026101 (2011).

[88] Lucier, A.-S. *Preparation and Characterization of Tungsten Tips Suitable for Molecular Electronics Studies*. Master's thesis, Center for the physics of materials, McGill University (2004).

[89] Gomer, R. *Field Emission and Field Ionization* (Harvard University Press, Cambridge, Massachusetts, 1961).

[90] Tsong, T. T. *Atom-Probe Field Ion Microscopy: Field Ion Emission, and Surfaces and Interfaces at Atomic Resolution* (Cambridge University Press, 2005).

[91] Müller, E. W. Versuche zur Theorie der Elektronenemission unter der Einwirkung hoher Feldstärken. *Z. Tech. Phys.* **37**, 838–842 (1936).

[92] Müller, E. W. Field Ion Microscopy. *Science* **149**, 591–601 (1965).

[93] Forbes, R. G. Field-ion imaging old and new. *Appl. Surf. Sci.* **9495**, 1–16 (1996).

[94] Gault, B., Moody, M. P., Cairney, J. M. & Ringer, S. P. Field Ion Microscopy. In *Atom Probe Microscopy*, Springer Series in Materials Science, 9–28 (Springer New York, 2012).

[95] Lucier, A.-S., Mortensen, H., Sun, Y. & Grütter, P. Determination of the atomic structure of scanning probe microscopy tungsten tips by field ion microscopy. *Phys. Rev. B* **72**, 235420 (2005).

[96] Airy, G. B. On the Diffraction of an Object-glass with Circular Aperture. *Cambridge Philos. Soc.* **5**, 283–291 (1835).

[97] Novotny, L. & Hecht, B. *Principles of Nano-Optics* (Cambridge University Press, Cambridge, 2012).

[98] Maier, S. A. *Plasmonics: Fundamentals and Applications* (Springer US, Boston, MA, 2007).

[99] Breuer, J. & Hommelhoff, P. Laser-Based Acceleration of Nonrelativistic Electrons at a Dielectric Structure. *Phys. Rev. Lett.* **111**, 134803 (2013).

[100] Peralta, E. A., Soong, K., England, R. J., Colby, E. R., Wu, Z., Montazeri, B., McGuinness, C., McNeur, J., Leedle, K. J., Walz, D., Sozer, E. B., Cowan, B., Schwartz, B., Travish, G. & Byer, R. L. Demonstration of electron acceleration in a laser-driven dielectric microstructure. *Nature* **503**, 91–94 (2013).

[101] Synge, E. H. A suggested method for extending the microscopic resolution into the ultramicroscopic region. *Phil. Mag.* **6**, 356 (1928).

[102] Jiang, S., Zhang, Y., Zhang, R., Hu, C., Liao, M., Luo, Y., Yang, J., Dong, Z. & Hou, J. G. Distinguishing adjacent molecules on a surface using plasmon-enhanced Raman scattering. *Nat. Nanotechnol.* **10**, 865–869 (2015).

[103] Takahashi, S. & Zayats, A. V. Near-field second-harmonic generation at a metal tip apex. *Appl. Phys. Lett.* **80**, 3479–3481 (2002).

[104] Bouhelier, A., Beversluis, M., Hartschuh, A. & Novotny, L. Near-Field Second-Harmonic Generation Induced by Local Field Enhancement. *Phys. Rev. Lett.* **90**, 013903 (2003).

[105] Neacsu, C. C., Reider, G. A. & Raschke, M. B. Second-harmonic generation from nanoscopic metal tips: Symmetry selection rules for single asymmetric nanostructures. *Phys. Rev. B* **71**, 201402 (2005).

[106] Anderson, A., Deryckx, K. S., Xu, X. G., Steinmeyer, G. & Raschke, M. B. Few-Femtosecond Plasmon Dephasing of a Single Metallic Nanostructure from Optical Response Function Reconstruction by Interferometric Frequency Resolved Optical Gating. *Nano Lett.* **10**, 2519–2524 (2010).

[107] Thomas, S., Krüger, M., Förster, M., Schenk, M. & Hommelhoff, P. Probing of Optical Near-Fields by Electron Rescattering on the 1 nm Scale. *Nano Lett.* **13**, 4790–4794 (2013).

[108] Krüger, M., Thomas, S., Förster, M. & Hommelhoff, P. Self-probing of metal nanotips by rescattered electrons reveals the nano-optical near-field. *J. Phys. B* **47**, 124022 (2014).

[109] Förg, B., Schötz, J., Süssmann, F., Förster, M., Krüger, M., Ahn, B.-N., Okell, W., Wintersperger, K., Zherebtsov, S., Guggenmos, A., Pervak, V., Kessel, A., Trushin, S., Azzeer, A., Stockman, M., Kim, D.-E., Krausz, F., Hommelhoff, P. & Kling, M. Attosecond nanoscale near-field sampling. *arXiv:1508.05611 [physics]* (2015).

[110] Yanagisawa, H., Hafner, C., Don, P., Klöckner, M., Leuenberger, D., Greber, T., Hengsberger, M. & Osterwalder, J. Optical Control of Field-Emission Sites by Femtosecond Laser Pulses. *Phys. Rev. Lett.* **103**, 257603 (2009).

[111] Thomas, S. *Electric Field Enhancement and Strong-Field Effects at Sharp Metal Tips Investigated with Few-Cycle Pulses from an Erbium-Doped Fiber Laser*. Master's thesis, München (2011).

[112] Paulus, G. G., Nicklich, W., Xu, H., Lambropoulos, P. & Walther, H. Plateau in above threshold ionization spectra. *Phys. Rev. Lett.* **72**, 2851 (1994).

[113] Zherebtsov, S., Fennel, T., Plenge, J., Antonsson, E., Znakovskaya, I., Wirth, A., Herrwerth, O., Sümann, F., Peltz, C., Ahmad, I., Trushin, S. A., Pervak, V., Karsch, S., Vrakking, M. J. J., Langer, B., Graf, C., Stockman, M. I., Krausz, F., Rühl, E. & Kling, M. F. Controlled near-field enhanced electron acceleration from dielectric nanospheres with intense few-cycle laser fields. *Nat. Phys.* **7**, 656–662 (2011).

[114] Lai, X. Y., Quan, W. & Liu, X. Tunneling-induced shift of the cutoff law for high-order above-threshold ionization. *Phys. Rev. A* **84**, 025401 (2011).

[115] Krüger, M., Schenk, M., Förster, M. & Hommelhoff, P. Attosecond physics in photoemission from a metal nanotip. *J. Phys. B* **45**, 074006 (2012).

[116] Hickstein, D. D., Ranitovic, P., Witte, S., Tong, X.-M., Huismans, Y., Arpin, P., Zhou, X., Keister, K. E., Hogle, C. W., Zhang, B., Ding, C., Johnsson, P., Toshima, N., Vrakking, M. J. J., Murnane, M. M. & Kapteyn, H. C. Direct Visualization of Laser-Driven Electron Multiple Scattering and Tunneling Distance in Strong-Field Ionization. *Phys. Rev. Lett.* **109**, 073004 (2012).

[117] Chirilă, C. C. & Lein, M. High-order above-threshold ionization in stretched molecules. *Phys. Rev. A* **74**, 051401 (2006).

[118] Krüger, M., Schenk, M., Hommelhoff, P., Wachter, G., Lemell, C. & Burgdörfer, J. Interaction of ultrashort laser pulses with metal nanotips: a model system for strong-field phenomena. *New J. Phys.* **14**, 085019 (2012).

[119] Wachter, G., Lemell, C., Burgdörfer, J., Schenk, M., Krüger, M. & Hommelhoff, P. Electron rescattering at metal nanotips induced by ultrashort laser pulses. *Phys. Rev. B* **86**, 035402 (2012).

[120] Park, D. J., Piglosiewicz, B., Schmidt, S., Kollmann, H., Mascheck, M. & Lienau, C. Strong Field Acceleration and Steering of Ultrafast Electron Pulses from a Sharp Metallic Nanotip. *Phys. Rev. Lett.* **109**, 244803 (2012).

[121] Yalunin, S. V., Herink, G., Solli, D. R., Krüger, M., Hommelhoff, P., Diehn, M., Munk, A. & Ropers, C. Field localization and rescattering in tip-enhanced photoemission. *Ann. Phys.* **525**, L12–L18 (2013).

[122] Yanagisawa, H., Hafner, C., Don, P., Klöckner, M., Leuenberger, D., Greber, T., Osterwalder, J. & Hengsberger, M. Laser-induced field emission from a tungsten tip:

Optical control of emission sites and the emission process. *Phys. Rev. B* **81**, 115429 (2010).

[123] Martin, Y. C., Hamann, H. F. & Wickramasinghe, H. K. Strength of the electric field in apertureless near-field optical microscopy. *J. Appl. Phys.* **89**, 5774–5778 (2001).

[124] Thomas, S., Wachter, G., Lemell, C., Burgdörfer, J. & Hommelhoff, P. Large optical field enhancement for nanotips with large opening angles. *New J. Phys.* **17**, 063010 (2015).

[125] Chang, W.-T., Hwang, I.-S., Chang, M.-T., Lin, C.-Y., Hsu, W.-H. & Hou, J.-L. Method of electrochemical etching of tungsten tips with controllable profiles. *Rev. Sci. Instrum.* **83**, 083704 (2012).

[126] Vogelsang, J., Robin, J., Nagy, B. J., Dombi, P., Rosenkranz, D., Schiek, M., Groß, P. & Lienau, C. Ultrafast Electron Emission from a Sharp Metal Nanotaper Driven by Adiabatic Nanofocusing of Surface Plasmons. *Nano Lett.* **15**, 4685–4691 (2015).

[127] Nelayah, J., Kociak, M., Stéphan, O., García de Abajo, F. J., Tencé, M., Henrard, L., Taverna, D., Pastoriza-Santos, I., Liz-Marzán, L. M. & Colliex, C. Mapping surface plasmons on a single metallic nanoparticle. *Nat. Phys.* **3**, 348–353 (2007).

[128] Barwick, B., Flannigan, D. J. & Zewail, A. H. Photon-induced near-field electron microscopy. *Nature* **462**, 902–906 (2009).

[129] Hohenester, U., Ditlbacher, H. & Krenn, J. R. Electron-energy-loss spectra of plasmonic nanoparticles. *Phys. Rev. Lett.* **103**, 106801 (2009).

[130] Esteban, R., Borisov, A. G., Nordlander, P. & Aizpurua, J. Bridging quantum and classical plasmonics with a quantum-corrected model. *Nat. Commun.* **3**, 825 (2012).

[131] Süßmann, F. & Kling, M. F. Attosecond nanoplasmonic streaking of localized fields near metal nanospheres. *Phys. Rev. B* **84**, 121406 (2011).

[132] Weinacht, T. C. & Bucksbaum, P. H. Using feedback for coherent control of quantum systems. *J. Opt. B* **4**, R35 (2002).

[133] Tannor, D. J. & Rice, S. A. Control of selectivity of chemical reaction via control of wave packet evolution. *J. Chem. Phys.* **83**, 5013–5018 (1985).

[134] Judson, R. S. & Rabitz, H. Teaching lasers to control molecules. *Phys. Rev. Lett.* **68**, 1500–1503 (1992).

[135] Zhu, L., Kleiman, V., Li, X., Lu, S. P., Trentelman, K. & Gordon, R. J. Coherent Laser Control of the Product Distribution Obtained in the Photoexcitation of HI. *Science* **270**, 77–80 (1995).

[136] Chen, C., Yin, Y.-Y. & Elliott, D. S. Interference between optical transitions. *Phys. Rev. Lett.* **64**, 507–510 (1990).

[137] Yin, Y.-Y., Chen, C., Elliott, D. S. & Smith, A. V. Asymmetric photoelectron angular distributions from interfering photoionization processes. *Phys. Rev. Lett.* **69**, 2353–2356 (1992).

[138] Muller, H. G., Bucksbaum, P. H., Schumacher, D. W. & Zavriyev, A. Above-threshold ionisation with a two-colour laser field. *J. Phys. B* **23**, 2761 (1990).

[139] Vrakking, M. J. J. & Stolte, S. Coherent control of molecular orientation. *Chem. Phys. Lett.* **271**, 209–215 (1997).

[140] De, S., Znakovskaya, I., Ray, D., Anis, F., Johnson, N. G., Bocharova, I. A., Magrakvelidze, M., Esry, B. D., Cocke, C. L., Litvinyuk, I. V. & Kling, M. F. Field-Free Orientation of CO Molecules by Femtosecond Two-Color Laser Fields. *Phys. Rev. Lett.* **103**, 153002 (2009).

[141] Dupont, E., Corkum, P. B., Liu, H. C., Buchanan, M. & Wasilewski, Z. R. Phase-Controlled Currents in Semiconductors. *Phys. Rev. Lett.* **74**, 3596–3599 (1995).

[142] Hach, A., Kostoulas, Y., Atanasov, R., Hughes, J. L. P., Sipe, J. E. & van Driel, H. M. Observation of Coherently Controlled Photocurrent in Unbiased, Bulk GaAs. *Phys. Rev. Lett.* **78**, 306–309 (1997).

[143] Baranova, N. B., Chudinov, A. N. & Zel'dovich, B. Y. Polar asymmetry of photoionization by a field with $\langle E^3 \rangle \neq 0$. Theory and experiment. *Opt. Commun.* **79**, 116–120 (1990).

[144] Höfer, U., Shumay, I. L., Reu, C., Thomann, U., Wallauer, W. & Fauster, T. Time-Resolved Coherent Photoelectron Spectroscopy of Quantized Electronic States on Metal Surfaces. *Science* **277**, 1480–1482 (1997).

[145] Güdde, J., Rohleder, M., Meier, T., Koch, S. W. & Höfer, U. Time-Resolved Investigation of Coherently Controlled Electric Currents at a Metal Surface. *Science* **318**, 1287–1291 (2007).

[146] Ruppert, C., Thunich, S., Abstreiter, G., Fontcuberta i Morral, A., Holleitner, A. W. & Betz, M. Quantum Interference Control of Femtosecond, μA Current Bursts in Single GaAs Nanowires. *Nano Lett.* **10**, 1799–1804 (2010).

[147] Boutu, W., Haessler, S., Merdji, H., Breger, P., Waters, G., Stankiewicz, M., Frasinski, L. J., Taieb, R., Caillat, J., Maquet, A., Monchicourt, P., Carre, B. & Salieres, P. Coherent control of attosecond emission from aligned molecules. *Nat. Phys.* **4**, 545–549 (2008).

[148] Dudovich, N., Smirnova, O., Levesque, J., Mairesse, Y., Ivanov, M. Y., Villeneuve, D. M. & Corkum, P. B. Measuring and controlling the birth of attosecond XUV pulses. *Nat. Phys.* **2**, 781–786 (2006).

[149] Xie, X., Dai, J. & Zhang, X.-C. Coherent Control of THz Wave Generation in Ambient Air. *Phys. Rev. Lett.* **96**, 075005 (2006).

[150] Miller, J. C., Compton, R. N., Payne, M. G. & Garrett, W. W. Resonantly Enhanced Multiphoton Ionization and Third-Harmonic Generation in Xenon Gas. *Phys. Rev. Lett.* **45**, 114–116 (1980).

[151] Ackermann, P., Scharf, A. & Halfmann, T. Strong quantum interferences in frequency up-conversion towards short vacuum-ultraviolet radiation pulses. *Phys. Rev. A* **89**, 063804 (2014).

[152] Gunawardena, M. & Elliott, D. S. Atomic Homodyne Detection of Weak Atomic Transitions. *Phys. Rev. Lett.* **98**, 043001 (2007).

[153] Shapiro, M. & Brumer, P. Coherent control of molecular dynamics. *Rep. Prog. Phys.* **66**, 859 (2003).

[154] Wehner, M. U., Ulm, M. H. & Wegener, M. Scanning interferometer stabilized by use of Pancharatnams phase. *Opt. Lett.* **22**, 1455 (1997).

[155] Güdde, J., Rohleder, M. & Höfer, U. Time-resolved two-color interferometric photoemission of image-potential states on Cu(100). *Appl. Phys. A* **85**, 345–350 (2006).

[156] Güdde, J. & Höfer, U. Femtosecond time-resolved studies of image-potential states at surfaces and interfaces of rare-gas adlayers. *Prog. Surf. Sci.* **80**, 49–91 (2005).

[157] Bowlan, P., Gabolde, P. & Trebino, R. Directly measuring the spatio-temporal electric field of focusing ultrashort pulses. *Opt. Expr.* **15**, 10219 (2007).

[158] Bowlan, P., Fuchs, U., Trebino, R. & Zeitner, U. D. Measuring the spatiotemporal electric field of tightly focused ultrashort pulses with sub-micron spatial resolution. *Opt. Expr.* **16**, 13663 (2008).

[159] Extermann, J., Bonacina, L., Courvoisier, F., Kiselev, D., Mugnier, Y., Le Dantec, R., Galez, C. & Wolf, J.-P. Nano-FROG: Frequency resolved optical gating by a nanometric object. *Opt. Expr.* **16**, 10405 (2008).

[160] Wnuk, P., Xuan, L. L., Slablab, A., Tard, C., Perruchas, S., Gacoin, T., Roch, J.-F., Chauvat, D. & Radzewicz, C. Coherent nonlinear emission from a single KTP nanoparticle with broadband femtosecond pulses. *Opt. Expr.* **17**, 4652 (2009).

[161] Accanto, N., Nieder, J. B., Piatkowski, L., Castro-Lopez, M., Pastorelli, F., Brinks, D. & van Hulst, N. F. Phase control of femtosecond pulses on the nanoscale using second harmonic nanoparticles. *Light Sci. Appl.* **3**, e143 (2014).

[162] Pawlowska, M., Goetz, S., Dreher, C., Wurdack, M., Krauss, E., Razinskas, G., Geisler, P., Hecht, B. & Brixner, T. Shaping and spatiotemporal characterization of sub-10-fs pulses focused by a high-NA objective. *Opt. Expr.* **22**, 31496 (2014).

[163] Piglosiewicz, B., Sadiq, D., Mascheck, M., Schmidt, S., Silies, M., Vasa, P. & Lienau, C. Ultrasmall bullets of light – focusing few-cycle light pulses to the diffraction limit. *Opt. Expr.* **19**, 14451 (2011).

[164] Wu, T.-w., Tang, J., Hajj, B. & Cui, M. Phase resolved interferometric spectral modulation (PRISM) for ultrafast pulse measurement and compression. *Opt. Expr.* **19**, 12961 (2011).

[165] Fauster, T. & Weinelt, M. Time-resolved photoemission from image-potential states. *J. Electron Spectr.* **114116**, 269–275 (2001).

[166] Homann, C., Bradler, M., Förster, M., Hommelhoff, P. & Riedle, E. Carrier-envelope phase stable sub-two-cycle pulses tunable around 1.8 μm at 100 kHz. *Opt. Lett.* **37**, 1673 (2012).

[167] Scholle, K., Lamrini, S., Koopmann, P. & Fuhrberg, P. *2 μm laser sources and their possible applications* (Intech, Croatia, 2010).

[168] Solem, J. C. & Baldwin, G. C. Microholography of Living Organisms. *Science* **218**, 229–235 (1982).

[169] Manzoni, C., Cerullo, G. & De Silvestri, S. Ultrabroadband self-phase-stabilized pulses by difference-frequency generation. *Opt. Lett.* **29**, 2668 (2004).

[170] Vozzi, C., Cirmi, G., Manzoni, C., Benedetti, E., Calegari, F., Sansone, G., Stagira, S., Svelto, O., De Silvestri, S., Nisoli, M. & Cerullo, G. High-energy, few-optical-cycle pulses at 1.5 μm with passive carrier-envelope phase stabilization. *Opt. Expr.* **14**, 10109 (2006).

[171] Gu, X., Marcus, G., Deng, Y., Metzger, T., Teisset, C., Ishii, N., Fuji, T., Baltuska, A., Butkus, R., Pervak, V., Ishizuki, H., Taira, T., Kobayashi, T., Kienberger, R. & Krausz, F. Generation of carrier-envelope-phase-stable 2-cycle 740-μJ pulses at 2.1-μm carrier wavelength. *Opt. Expr.* **17**, 62 (2009).

[172] Li, C., Wang, D., Song, L., Liu, J., Liu, P., Xu, C., Leng, Y., Li, R. & Xu, Z. Generation of carrier-envelope phase stabilized intense 1.5 cycle pulses at 1.75 μm. *Opt. Expr.* **19**, 6783 (2011).

[173] Schmidt, B. E., Shiner, A. D., Lassonde, P., Kieffer, J.-C., Corkum, P. B., Villeneuve, D. M. & Legare, F. CEP stable 1.6 cycle laser pulses at 1.8 μm. *Opt. Expr.* **19**, 6858 (2011).

[174] Hong, K.-H., Huang, S.-W., Moses, J., Fu, X., Lai, C.-J., Cirmi, G., Sell, A., Granados, E., Keathley, P. & Kärtner, F. X. High-energy, phase-stable, ultrabroadband kHz OPCPA at 2.1 μm pumped by a picosecond cryogenic Yb:YAG laser. *Opt. Expr.* **19**, 15538 (2011).

[175] Deng, Y., Schwarz, A., Fattahi, H., Ueffing, M., Gu, X., Ossiander, M., Metzger, T., Pervak, V., Ishizuki, H., Taira, T., Kobayashi, T., Marcus, G., Krausz, F., Kienberger, R. & Karpowicz, N. Carrier-envelope-phase-stable, 1.2 mJ, 1.5 cycle laser pulses at 2.1 μm. *Opt. Lett.* **37**, 4973 (2012).

[176] Mücke, O. D., Sidorov, D., Dombi, P., Pugžlys, A., Baltuška, A., Ališauskas, S., Smilgevičius, V., Pocius, J., Giniunas, L., Danielius, R. & Forget, N. Scalable Yb-MOPA-driven carrier-envelope phase-stable few-cycle parametric amplifier at 1.5 μm. *Opt. Lett.* **34**, 118 (2009).

[177] Heese, C., Gallmann, L., Keller, U., Phillips, C. R. & Fejer, M. M. Ultrabroadband, highly flexible amplifier for ultrashort midinfrared laser pulses based on aperiodically poled Mg:LiNbO3. *Opt. Lett.* **35**, 2340 (2010).

[178] Thai, A., Hemmer, M., Bates, P. K., Chalus, O. & Biegert, J. Sub-250-mrad, passively carrier-envelope-phase-stable mid-infrared OPCPA source at high repetition rate. *Opt. Lett.* **36**, 3918 (2011).

[179] Darginavicius, J., Garejev, N. & Dubietis, A. Generation of carrier-envelope phase-stable two optical-cycle pulses at 2 μm from a noncollinear beta-barium borate optical parametric amplifier. *Opt. Lett.* **37**, 4805 (2012).

[180] Vogelsang, J., Robin, J., Piglosiewicz, B., Manzoni, C., Farinello, P., Melzer, S., Feru, P., Cerullo, G., Lienau, C. & Groß, P. High passive CEP stability from a few-cycle, tunable NOPA-DFG system for observation of CEP-effects in photoemission. *Opt. Expr.* **22**, 25295 (2014).

[181] Hoogland, H., Thai, A., Snchez, D., Cousin, S. L., Hemmer, M., Engelbrecht, M., Biegert, J. & Holzwarth, R. All-PM coherent 2.05 μm Thulium/Holmium fiber frequency comb source at 100 MHz with up to 0.5 W average power and pulse duration down to 135 fs. *Opt. Expr.* **21**, 31390 (2013).

[182] Li, P., Ruehl, A., Grosse-Wortmann, U. & Hartl, I. Sub-100 fs passively mode-locked holmium-doped fiber oscillator operating at 2.06 μm. *Opt. Lett.* **39**, 6859 (2014).

[183] Gebhardt, M., Gaida, C., Hädrich, S., Stutzki, F., Jauregui, C., Limpert, J. & Tünnermann, A. Nonlinear compression of an ultrashort-pulse thulium-based fiber laser to sub-70 fs in Kagome photonic crystal fiber. *Opt. Lett.* **40**, 2770 (2015).

[184] Vasilyev, S., Moskalev, I., Mirov, M., Mirov, S. & Gapontsev, V. Three optical cycle mid-IR Kerr-lens mode-locked polycrystalline Cr^{2+}:ZnS laser. *Opt. Lett.* **40**, 5054 (2015).

[185] Wachter, G., Lemell, C. & Burgdörfer, J. Electron rescattering at metal nanotips induced by ultrashort laser pulses. *J. Phys.: Conf. Ser.* **488**, 012005 (2014).

[186] Yanagisawa, H., Schnepp, S., Hafner, C., Hengsberger, M., Landsman, A., Gallmann, L. & Osterwalder, J. Temporal and spectral disentanglement of laser-driven electron tunneling emission from a solid. *arXiv:1405.0609 [cond-mat]* (2014).

[187] Ghimire, S., DiChiara, A. D., Sistrunk, E., Agostini, P., DiMauro, L. F. & Reis, D. A. Observation of high-order harmonic generation in a bulk crystal. *Nat. Phys.* **7**, 138–141 (2011).

[188] Schubert, O., Hohenleutner, M., Langer, F., Urbanek, B., Lange, C., Huttner, U., Golde, D., Meier, T., Kira, M., Koch, S. W. & Huber, R. Sub-cycle control of terahertz high-harmonic generation by dynamical Bloch oscillations. *Nat. Photon.* **8**, 119–123 (2014).

[189] Schmidt, E. *Photon generation and electron emission studies at metal nanotips.* Master's thesis, Erlangen (2015).

[190] Breuer, J., Graf, R., Apolonski, A. & Hommelhoff, P. Dielectric laser acceleration of nonrelativistic electrons at a single fused silica grating structure: Experimental part. *Phys. Rev. ST Accel. Beams* **17**, 021301 (2014).

[191] Park, D. J., Piglosiewicz, B., Schmidt, S., Kollmann, H., Mascheck, M., Groß, P. & Lienau, C. Characterizing the optical near-field in the vicinity of a sharp metallic nanoprobe by angle-resolved electron kinetic energy spectroscopy. *Ann. Phys.* **525**, 135–142 (2013).

[192] Nagel, P. M., Robinson, J. S., Harteneck, B. D., Pfeifer, T., Abel, M. J., Prell, J. S., Neumark, D. M., Kaindl, R. A. & Leone, S. R. Surface plasmon assisted electron acceleration in photoemission from gold nanopillars. *Chem. Phys.* **414**, 106–111 (2013).

[193] Longchamp, J.-N., Latychevskaia, T., Escher, C. & Fink, H.-W. Low-energy electron holographic imaging of individual tobacco mosaic virions. *Appl. Phys. Lett.* **107**, 133101 (2015).

[194] Maisenbacher, L. *Comparison of the material response in carrier-envelope-phase-resolved photoemission metal nanotip vs. atomic gas.* Master's thesis, München (2012).

[195] Chen, C. & Elliott, D. S. Measurements of optical phase variations using interfering multiphoton ionization processes. *Phys. Rev. Lett.* **65**, 1737–1740 (1990).

Acknowledgments

It is my great pleasure to thank all those who participated in the success of this thesis.

First I would like to thank my advisor, Prof. Peter Hommelhoff. Peter, I thank you for your passion for our work inside and outside the lab, for your creativity, for many hints in the right direction, for providing the opportunity of an excellent environment at MPQ and in Erlangen, and for the many chances to present our work around the world.

I am thankful to our collaborators at Technical University of Vienna, Prof. Joachim Burgdörfer, Prof. Christoph Lemell, Dr. Florian Libisch, Dr. Georg Wachter, and Thomas Madlener. Thank you for sharing your deep knowledge, your simulations of light-matter interaction, and the discussions regarding the mechanism of the coherent control of photoemission.

Many useful hints came from our collaborators at Ludwig-Maximilians-University Munich, Prof. Eberhard Riedle, Dr. Christian Homann, and Dr. Maximilian Bradler. Thank you for your letting us profit from your extensive experience, knowledge, and support for the NOPA-DFG system.

I would like to thank our collaborators at the Max-Planck-Institute for Quantum Optics in Garching, Prof. Matthias Kling, Dr. Frederik Süßmann, Benjamin Förg, Johannes Schötz, and Karen Wintersperger. Thanks for sharing your vast knowledge on attosecond streaking and the hard work inside and outside the lab to make the XUV-IR streaking experiment on our tips a reality.

From our group I would first like to thank Dr. Anoush Aghajani-Talesh, Dr. Michael Krüger, and Timo Paschen. Together we spent many hours in the lab setting up our experiments and uncovering the secrets of laser-tip interaction. I am very greatful for your dedication, passion, and knowledge, and the friendship inside and outside the lab. The same goes for Sebastian Thomas. I'd like to thank you in particular for your FDTD simulations of Maxwell's equations. Thank you Timo, Sebastian, and Michael for proofreading this thesis. Thanks to Martin Hundhausen and Takuya Higuchi for many discussions about physics and other matters, to Markus Schenk for the initial setup of the vacuum chamber. I'd like to thank Ella Schmidt, Alexander Lang, and Alexander Hirler. Thank you for your dedication to your theses that helped advance our work. I'd like to thank our whole group. Thank you, everyone, for the atmosphere of industry and excitement, for the support in many small matters that went without saying.

I am grateful to the technicians at MPQ and at FAU, Karl Linner, Wolfgang Simon, and Helmut Brückner and the teams around Thomas Spona and Florian Schmitt. Without

you much of this work would not have been possible. Special thanks are due to Gerhard Schlosser. Thank you for all your work supporting setting up the new lab. I'd also like to thank our secretaries Bettina Schütz, Jutta Zintchenko, and Claudia Schlechte for excellently handling many administrative matters.

For personal support I am grateful to the international Max-Planck research school for advanced photon science (IMPRS-APS), mostly impersonated by Monica Wild. Thanks to everyone in the school for creating such an exciting environment at our meetings, the lectures, and beyond.

Finally, I would like to thank my family and friends. I am very grateful for your never-fading support and the beautiful time we share.